optica

Volume 1 • Issue 3 • September 2014

OSA®
The Optical Society

ISSN: 2334-2536

optica.osa.org

Research Article Vol. 1, No. 3 / September 2014 / Optica 129

Non-invasive monitoring and control in silicon photonics using CMOS integrated electronics

Stefano Grillanda,[1,*,†] Marco Carminati,[1,†] Francesco Morichetti,[1] Pietro Ciccarella,[1] Andrea Annoni,[1] Giorgio Ferrari,[1] Michael Strain,[2] Marc Sorel,[3] Marco Sampietro,[1] and Andrea Melloni[1]

[1]Dipartimento di Elettronica, Informazione e Bioingegneria, Politecnico di Milano, 20133 Milano, Italy

[2]Institute of Photonics, The University of Strathclyde, Glasgow G4 0NW, UK

[3]School of Engineering, University of Glasgow, Glasgow G12 8QQ, UK

*Corresponding author: stefano.grillanda@polimi.it

Received 22 May 2014; revised 15 July 2014; accepted 15 July 2014 (Doc. ID 212608); published 27 August 2014

As photonics moves from the single-device level toward large-scale, integrated, and complex systems on a chip, monitoring, control, and stabilization of the components become critical. We need to monitor a circuit non-invasively and apply a simple, fast, and robust feedback control. Here, we show non-invasive monitoring and feedback control of high-quality-factor silicon (Si) photonic resonators assisted by a transparent detector that is directly integrated inside the cavity. Control operations are entirely managed by a CMOS microelectronic circuit that is bridged to the Si photonic chip and hosts many parallel electronic readout channels. Advanced functionalities, such as wavelength tuning, locking, labeling, and swapping, are demonstrated. The non-invasive nature of the transparent monitor and the scalability of the CMOS readout system offer a viable solution for the control of arbitrarily reconfigurable photonic integrated circuits aggregating many components on a single chip.

OCIS codes: (130.0130) Integrated optics; (250.5300) Photonic integrated circuits; (230.5750) Resonators; (130.0250) Optoelectronics; (040.6040) Silicon.

http://dx.doi.org/10.1364/OPTICA.1.000129

1. INTRODUCTION

The level of complexity achieved by today's integrated electronic systems is commonly perceived as the result, primarily, of challenging technological efforts to scale device dimensions down to their ultimate physical limits [1]. Although this is indeed true, it is only partially responsible for their success, as miniaturization is not synonymous with large-scale integration. In fact, analog electronic circuits cannot function properly without adequate tools to dynamically steer and hold each embedded device to the desired working point, counteracting functional drifts due to fluctuations in the environment, aging effects, mutual crosstalk, and fault events [2].

This argument is equally applicable to photonic technologies. Even though photonic platforms, like silicon-on-insulator (SOI), have demonstrated maturity for squeezing several thousands of photonic elements in a footprint of less than 1 mm^2 [3], the evolution of integrated photonics from device-level to large-scale systems is still a challenge. In fact, when aggregating several components on a single chip, the aforementioned parasitic effects become critical and need to be addressed through feedback control loops that locally monitor and continuously set each optical element to the desired functionality [4].

These issues are particularly severe in silicon (Si) photonic microresonators, due to their extreme sensitivity to fabrication tolerances [5] and temperature variations [6]. Several approaches have recently been proposed to lock the resonant wavelength of Si microrings, for instance by applying dithering signals [7] or homodyne detection schemes [8], and by monitoring the power level [9,10] or bit-error rate [11] of

the optical signal. However, all the techniques proposed so far require the use of on-chip or external photodetectors to partially tap the light travelling in the resonator. Though effective on single devices, this approach is not scalable to large-scale integration circuits [12], where multipoint light tapping would result in a large amount of optical power being wasted for monitoring operation. Local feedback control assisted by transparent optical detectors is envisioned as an enabling tool for the realization of complex and arbitrarily reconfigurable systems on a chip [13–15].

Here, we show a Si photonic–electronic integrated platform enabling the feedback control of Si photonic integrated circuits without the need of tapping any photon from the waveguide. The status of high-quality-factor resonators is monitored by a recently pionereed ContactLess Integrated Photonic Probe (CLIPP) [16] that realizes a fully transparent detector and can be integrated directly inside any photonic circuit, including microrings. The feedback loop, combining the CLIPP readout system and the microring control functions, is entirely integrated onto an electronic CMOS circuit [17] that is wire-bonded to the Si photonic chip. Advanced functionalities and control operations such as wavelength tuning, locking, labeling, and swapping are demonstrated in a thermally actuated resonator, proving that the presented Si photonic–electronic integrated platform is an efficient and flexible solution for the realization and control of Si photonic circuits hosting many components.

2. CLIPP CONCEPT AND FABRICATION

Figure 1(a) shows a top-view photograph of a microring fabricated using SOI technology, where the CLIPP electrodes and the thermal actuator are integrated. The microring is 516 μm long, has 20 μm bending radius, and is realized by a channel waveguide with 480 nm wide and 220 nm thick Si core [Fig. 1(b)], patterned by means of electron-beam lithography [18]. The waveguide core is buried into a 1 μm thick silicon dioxide (SiO_2) top cladding that is grown by plasma-enhanced chemical vapor deposition [16,18]. On top of it, the metallic

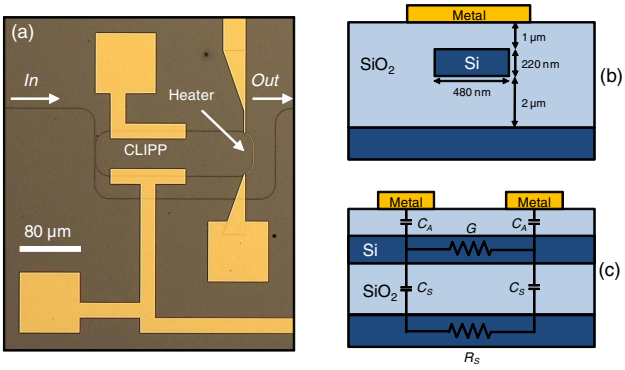

Fig. 1. (a) Top-view photograph of the fabricated Si microring, where CLIPP and thermal actuator are integrated. (b) Cross-section of the Si core waveguide, with the CLIPP metal electrode deposited on top of the SiO_2 cladding. (c) Longitudinal profile of the Si waveguide showing the CLIPP equivalent circuit in the electrical domain. The substrate resistance R_S is negligible with respect to the other impedances of the circuit.

NiCr heaters and Au pads of the CLIPP are patterned by lift-off technique and placed at sufficient distance from the Si core to avoid any significant interaction with the optical mode.

The CLIPP is constituted simply by two 100 μm long metal electrodes placed on top of the microring waveguide, here mutually spaced by about 83 μm on the side of the bus-to-ring directional coupler. The CLIPP can be fabricated using any CMOS-compatible metal technology, and can exploit traditional processes used for the fabrication of thermal actuators, without requiring any additional or specific process step.

The equivalent electrical circuit of the CLIPP is reported in Fig. 1(c), which shows the longitudinal profile of the waveguide. Due to the typical doping of SOI wafers (10^{15} cm^{-3}, *p*-type), the Si core acts mainly as a resistor of conductance G, whereas the insulating top cladding provides the access capacitances C_A. The CLIPP monitors variations of the waveguide electric conductance ΔG with optical power P that are induced by a carrier generation effect, occurring at the native Si/SiO_2 interface, associated with intrinsic surface state absorption (SSA) processes [16,19]. These phenomena exist even in ideally smooth interfaces due to the termination of the Si lattice at the walls of the waveguide core [20]. The results shown in this work demonstrate indeed that the CLIPP approach successfully applies to low-loss Si waveguides with a very good quality of the Si/SiO_2 interface. In our waveguides, exhibiting optical loss lower than 1.5 dB/cm, the CLIPP signal-to-noise ratio (SNR) achieved by using low-noise standard CMOS readout electronics (see Section 3) is sufficiently large to make it exploitable for monitoring and feedback control operations (see Sections 4 and 5). This also implies that no specific damaging treatments need to be applied to the waveguide in order to increase the density of interface states, and hence the SNR.

Other all-silicon detectors, based on SSA [19,21] or defect mediated absorption [9,22,23], require the photogenerated carriers to be swept away from the waveguide through highly doped regions or electric lines directly contacted to the Si core, thus resulting in additional optical loss. In contrast, the capacitively coupled electrodes of the CLIPP perform a remote monitoring of the optical field, thus avoiding any perturbation [16]. In this sense, the CLIPP realizes a transparent detector that can be placed in any point of the circuit to monitor its local status without affecting its functionality.

3. CLIPP READOUT SYSTEM

The CLIPP observes directly the amount of light stored in the resonant cavity, information that traditionally is not available unless a portion of the optical power is tapped and rerouted to a photodetector, by measuring variations of the electric conductance G of the waveguide core [16].

Readout operations of the CLIPP electric signal, as well as microring control functionalities (such as wavelength tuning, locking, labeling, and swapping), are performed by means of a custom microelectronic circuit [17] whose schematic is shown in Fig. 2(a). One of the CLIPP electrodes is excited with a sinusoidal electrical signal with frequency f_e and amplitude V_e, whereas the current flow i_e at the other one is collected by means

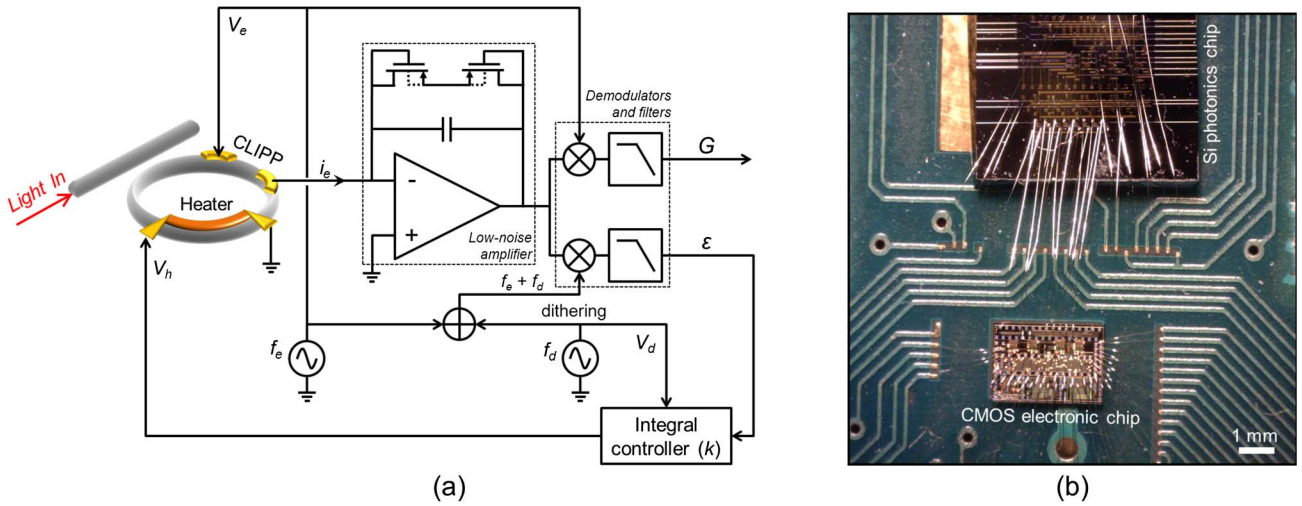

Fig. 2. (a) Schematic of the electronic integrated circuit that performs the readout of the CLIPP electric signal and manages control operations of the Si photonic microring resonator (such as wavelength tuning, locking, labeling, and swapping). (b) Photograph of the Si photonic chip (on the top) hosting the microring resonator that is wire-bonded to the CMOS electronic chip (in the bottom) containing all the CLIPP readout and microring control circuitry. Both the photonic and electronic chips are integrated onto the same printed circuit board.

of a low-noise amplifier. Then, the CLIPP signal is demodulated at frequency f_e to provide the electric conductance G.

The electric readout frequency of the CLIPP is typically around $f_e = 1$ MHz in order to bypass the capacitances C_A and access directly the waveguide conductance G. Actually, as shown in Fig. 1(c), there is a parasitic path composed of stray capacitances C_S across the SiO_2 undercladding and the Si substrate resistance R_S. Due to the Si conductivity and the large thickness of the chip substrate, R_S is negligible compared to the other impedances of the circuit. In this device, C_S is smaller than C_A so that, when the CLIPP is driven at f_e, no significant stray current is injected through the parasitic path that can therefore be neglected.

The amplitude of the applied signal is usually $V_e = 1$ V, so that neither attenuation nor significant perturbation of the optical mode and quality factor is induced [16]. The integrated electronic circuit manages control operations of the microring, like wavelength tuning, locking, labeling, and swapping, using the dithering and feedback controller units reported in the schematic (see Sections 4–6).

The electronic readout circuit is integrated in a CMOS chip (0.35 μm process by AMS Foundry) with 32 readout channels that is wire-bonded to the Si photonic chip hosting the microring resonator (fabricated by the James Watt Nanofabrication Centre at University of Glasgow) [Fig. 2(b)]. Both the electronic and the photonic chips are integrated onto the same printed circuit board. The design of the CMOS chip was optimized to achieve a noise level as low as 2 pS rms with a lock-in bandwidth $B_e = 1$ Hz [17]. This photonic–electronic integrated platform also offers a simple and flexible system for the realization and control of large-scale Si photonic-integrated circuits, hosting several components to achieve complex systems on a chip.

The driving frequency f_e and the SNR of the CLIPP signal are the most relevant parameters for the miniaturization of the CLIPP size. With reference to the equivalent electric circuit of Fig. 1(c), a reduction of the electrode spacing would increase G, whereas a reduction of the electrode length would make C_A smaller. Both these actions would result in a higher driving frequency f_e. For instance, the CLIPP of Fig. 1(a) can be scaled down by a factor of 10, corresponding to less than 30 μm overall length, at the price of an access frequency f_e of 100 MHz (due to a 10× increase of G and a 10× decrease of C_A). This would make the CLIPP integrable inside Si microrings with radius of less than 15 μm (i.e., around 100 μm ring length), this being the typical size of low-energy Si microring modulators [10].

The main drawback of a higher f_e is the reduction of the SNR. In fact, moving from 1 to 100 MHz, a 10× reduction of the SNR is expected because the CLIPP signal is 10 times higher (due to the reduction of G), but the noise level is 100 times higher (because of the larger noise spectral density increasing with frequency [17]). In order to reduce f_e, a thinner SiO_2 layer (down to 600 nm) can be used as waveguide upper cladding so as to increase C_A and correspondingly reduce the noise bandwidth. Further, to compensate for the SNR reduction, parasitic paths in parallel to the waveguide or toward the substrate can be minimized, for instance by adopting an insulating substrate. Note that the SNR can be also improved by increasing the voltage V_e applied to the CLIPP, yet at the price of some more perturbation of the optical field [16].

These considerations show that the integration of the CLIPP inside ultrasmall resonators with a radius of less than 5 μm [24] would require a higher readout frequency (several hundreds of megahertz). In this case, it could be more convenient to place the CLIPP outside the resonator. However, also in this case, the CLIPP would have a significant advantage compared to conventional integrated detectors [10,24], because it can be placed directly on the output bus waveguide of the resonator and no additional tap waveguides would be needed for monitoring operations.

4. TUNING THE MICRORING RESONANT WAVELENGTH

Figure 3(a) shows the variations of conductance ΔG induced by the propagation of quasi-transverse electric (TE) polarized light in the resonator, measured by the CLIPP versus wavelength, when the thermal actuator is off (blue line), and then driven with voltage $V_h = 2$, 3, 4 V (red, green, and orange lines). The microring has a linewidth of 51 pm (6.4 GHz), free spectral range of 1.115 nm (139.2 GHz), and quality factor of about 30,000. Also, the corresponding optical power traveling in the resonator is provided on the rightmost vertical axis, as estimated from the conductance variations ΔG measured by the CLIPP [16]. A peak conductance change of about 0.4 nS is measured ($B_e = 1$ Hz), corresponding to a SNR of about 200. Any spurious conductance change due to thermal crosstalk effects between CLIPP and heater is negligible here, being more than one order of magnitude smaller than ΔG induced by light at the low power levels utilized in this work.

The effectiveness of the CLIPP to monitor the transfer function of the microring is exploited to automatically tune its resonant wavelength in order to overlap with that of an external laser [Fig. 3(b)]. The laser wavelength is initially redshifted with respect to that of the resonator by about 230 pm (4.5 times the ring linewidth), then while the heater voltage V_h is automatically and continuously increased to shift the resonant wavelength (red line), the CLIPP simultaneously monitors the optical intensity stored in the cavity (blue line). In order to track this variation, a faster CLIPP response was achieved by enlarging B_e to 100 Hz (noise level of 9 pS rms). The inset of Fig. 3(b) shows the CLIPP monitoring the microring resonant wavelength versus the voltage applied to the heater. The tuning process, here achieved in about 260 ms, terminates when the optical power measured by the CLIPP reaches its maximum value, here for $V_h = 3.2$ V, condition that occurs only when the resonator wavelength is aligned to that of the laser.

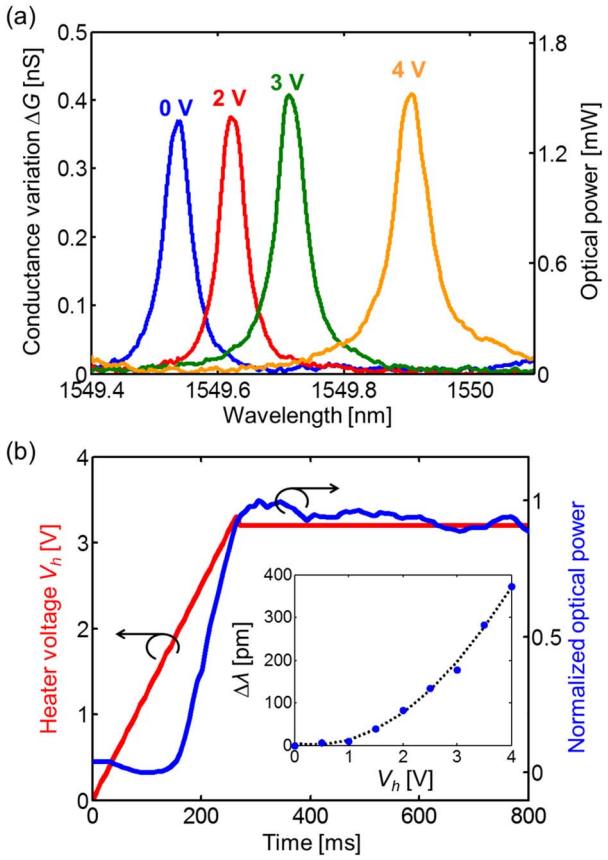

Fig. 3. Tuning of the microring resonant wavelength assisted by the CLIPP. (a) Light-induced conductance variation ΔG measured by the CLIPP ($B_e = 1$ Hz) and corresponding estimated optical power as a function of wavelength when the thermal actuator is off (blue line) and then switched on at $V_h = 2$, 3, 4 V (red, green, and orange lines). (b) Automated tuning of the resonator wavelength to that of an external laser, here detuned by about 230 pm, assisted by the CLIPP ($B_e = 100$ Hz); the inset shows the wavelength shift $\Delta\lambda$ measured by the CLIPP as the heater voltage V_h is increased from 0 to 4 V.

Actually, Fig. 3(b) shows that the intracavity optical power measured by the CLIPP increases and then slightly decreases beyond the point where voltage is no longer changed. The reason is that an open loop tuning procedure does not ensure bringing the microring exactly at resonance condition. In this experiment, we estimated a 6 pm residual wavelength shift, corresponding to about 10% of the resonator 3 dB linewidth. The main cause for this inaccuracy is the instability of the fiber to waveguide optical coupling at the waveguide input that, in our setup, introduces power fluctuations on the order of ± 0.2 dB on a time scale of a few hundreds of milliseconds. Moreover, some residual thermal drift contributes to reducing the tuning accuracy. In order to make the tuning procedure independent on power fluctuation and more robust against thermal drifts, feedback control and locking algorithms must be used, as described in Section 5.

5. LOCKING THE MICRORING RESONANT WAVELENGTH

Here, we demonstrate that the CLIPP can be exploited for feedback-controlling the microring by locking its resonant wavelength to that of an external laser. The CLIPP monitors the intracavity optical intensity and provides a feedback error signal to the thermal actuator to adjust the resonant wavelength of the microring. In particular, we employ a common dithering technique [7], according to which a small modulation signal is applied to the resonator and then, by mixing it with the modulated intracavity optical intensity measured by the CLIPP, an error signal is extracted and used to drive the feedback loop [as shown in the schematic of Fig. 2(a)].

A. Generation and Readout of the Error Signal

Figure 4(a) shows the optical intensity in the resonator measured by the CLIPP, here low-pass filtered, when a sinusoidal dithering signal with frequency $f_d = 160$ Hz and amplitude $V_d = 100$ mV is applied to the heater of the resonator, as in the schematic of Fig. 2(a). In addition, a 2 V bias is applied to the heater in order to have the resonant wavelength overlapped to that of the laser. Here, a detection bandwidth $B_e = 1$ kHz is used to measure the conductance variation ΔG. The CLIPP also monitors the corresponding error signal ε [Fig. 4(b), red line] by demodulating the resonant optical power at frequency

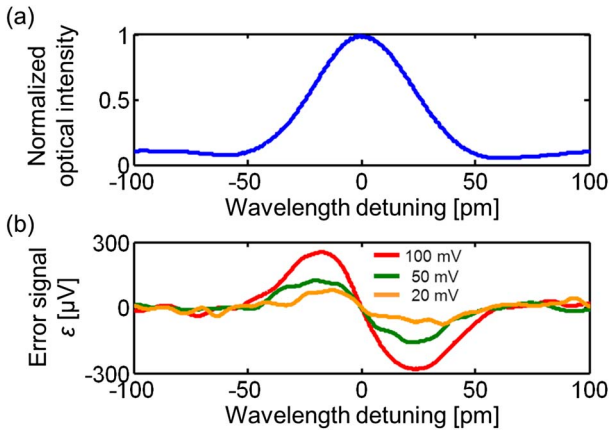

Fig. 4. Generation and readout of the error signal of the feedback-controlled microring. (a) Normalized optical intensity measured by the CLIPP versus wavelength, with $V_e = 1$ V and $f_e = 1$ MHz, when a dithering signal with amplitude $V_d = 100$ mV and frequency $f_d = 160$ Hz is applied to the heater. (b) Error signal ε extracted by the CLIPP by further demodulating the optical power P at the frequency of the dithering signal f_d for dithering amplitudes $V_d = 20$, 50, and 100 mV.

$f_e + f_d = 1.00016$ MHz. To extract the amplitude of the dithering signal applied to the heater, a second filter with a bandwidth $B_d = 100$ Hz is added, which ultimately sets the dominant time constant of the loop system (see Supplement 1). The error signal is zero at the resonant wavelength ($\lambda_r = 1549.54$ nm) and maximum on the slope of the resonator ($\lambda_r \pm 20$ pm). Also, thanks to the antisymmetric shape of ε, no ambiguity is left as to where λ_r is located. The application of a dithering signal with 100 mV amplitude corresponds to a thermal fluctuation as low as $\Delta T = 0.14$ K (wavelength shift $\Delta\lambda = 11$ pm, corresponding to about 20% of the linewidth) that is in line with those used for tap detectors [7] and does not affect the quality of the transmitted signal [10]. Though small, the amplitude of V_d can be further reduced to minimize the induced $\Delta\lambda$: in fact, with amplitudes of 50 mV and even 20 mV [Fig. 4(b), green and orange lines] corresponding respectively to $\Delta T = 0.07$ K ($\Delta\lambda = 5$ pm, 10% of the linewidth) and $\Delta T = 0.03$ K ($\Delta\lambda = 2$ pm, 4% of the linewidth), the error control signal is well above the noise level and can be used to drive the feedback loop.

B. Implementation of the Control Loop

In order to have the resonator wavelength λ_r continuously locked to that of an external laser λ_l, the CLIPP monitors simultaneously and continuously the intracavity optical intensity and the level of the error signal ε. As λ_r and λ_l drift apart from each other, the resonant optical power drops and the error signal deviates from zero. Consequently, the voltage applied to the heater is updated with an increment proportional to ε, its sign indicating the direction to follow (heating or cooling), and thus restoring the alignment between λ_r and λ_l.

The feedback loop is implemented by means of an integral controller whose gain k depends on the magnitude of ε with respect to the wavelength detuning $\Delta\lambda$ [Fig. 4(b)], and on the wavelength shift that the heater can achieve [inset of Fig. 3(b)]. According to our model, k should be sufficiently high to achieve fast response of the feedback loop but, at the same time, low enough to guarantee stability of the system (see Supplement 1 for details). As an example, considering that $\Delta\varepsilon/\Delta\lambda = 15$ μV/pm around the resonant wavelength when $V_d = 100$ mV, and that the heater shifts λ_r by about 95 pm/V around 2 V bias, a controller gain around $k = 10,000$ is sufficient to provide a loop response as low as 50 ms, while maintaining the system stability according to the Bode criterion. Here, the controller is implemented by means of a programmable digital platform (FPGA), thus allowing more speed and flexibility in setting the controller parameters with respect to computer-assisted architectures.

C. Testing the Control Loop

The feedback loop is here tested against external fluctuations of the laser wavelength. Figure 5 shows the optical intensity in the microring, measured by the CLIPP as a function of time, when

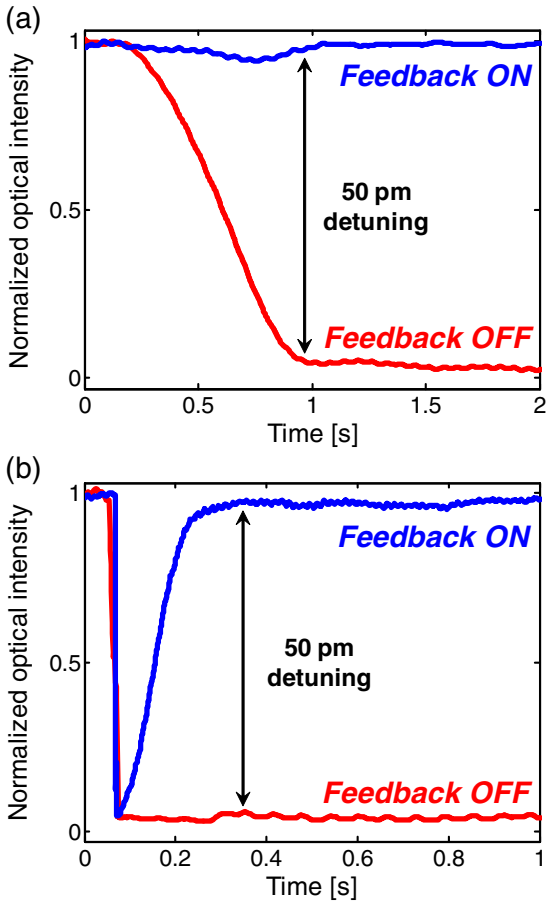

Fig. 5. Locking the microring resonant wavelength to that of an external laser λ_l assisted by the CLIPP. Normalized optical intensity in the resonator measured by the CLIPP when the feedback control is on (blue lines) and off (red lines) in the presence of (a) a continuous wavelength sweep (here occurring in about 700 ms) and (b) an instantaneous wavelength shift of the external laser by 50 pm (corresponding to 98% of the resonator linewidth). The considered 50 pm wavelength shift is the same of a temperature variation of 0.7 K.

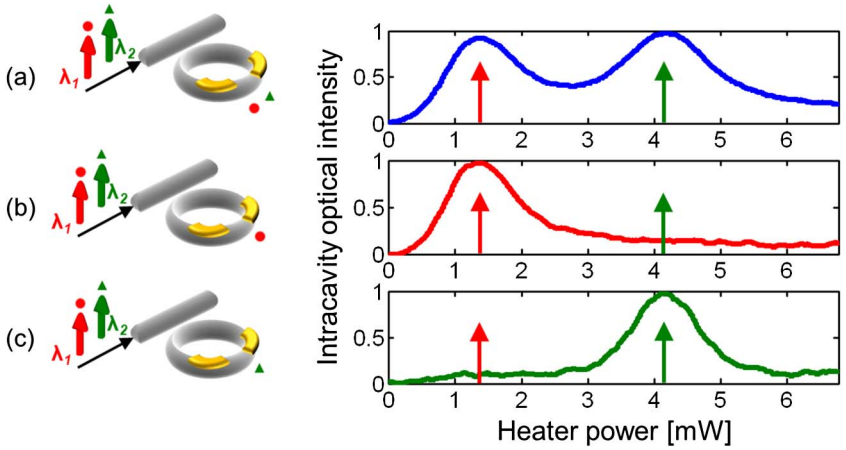

Fig. 6. Swapping the resonator wavelength between two optical signals at wavelengths λ_1 (red arrow) and λ_2 (green arrow) injected in the microring. A weak modulation tone with depth 2% is added to label each of the optical carriers: the tone centered on λ_1 has frequency $f_1 = 10$ kHz (labeled with a red circle), whereas the tone around λ_2 has frequency $f_2 = 11$ kHz (labeled with a green triangle). The optical intensity measured by the CLIPP in the resonator is reported as a function of the electrical power dissipated on the heater when the CLIPP signal is demodulated at frequencies (a) $f_e = 1$ MHz, (b) $f_e + f_1 = 1.010$ MHz, and (c) $f_e + f_2 = 1.011$ MHz. When demodulating the CLIPP signal at frequency f_e, the signals λ_1 and λ_2 are indistinguishable; in constrast, when readout operations are performed at frequency $f_e + f_1$ ($f_e + f_2$), the CLIPP is able to identify distinctively λ_1 (λ_2).

the feedback routine is on (blue lines) and off (red lines), in presence of a detuning of λ_l by 50 pm, which is about the same as the resonator linewidth, and corresponding to a temperature variation of 0.7 K. In Fig. 5(a), where a continuous wavelength shift is imposed by the laser, no significant variation in the resonant optical intensity is observed (blue line) along the entire wavelength detuning (here occurring in about 700 ms). This means that λ_l and λ_r are always locked one to another by the feedback control. In these conditions, the closed-loop system works in the linearity range of the error signal of Fig. 4 (see Supplement 1 for details) and at the highest SNR condition ($B_d = 100$ Hz, noise level 9 pS rms, SNR > 40), because the CLIPP signal is always at its maximum [$\Delta G = 0.4$ nS, see Fig. 3(a)]. Actually, Fig. 5(b) shows that the feedback loop is able to bring the microring back to resonance even after an instantaneous wavelength shift of the laser source, thus making the control system work in less favorable conditions. As λ_l is abruptly changed by 50 pm, the optical intensity in the resonator drops to less than 5%, but then is rapidly restored (here in about 150 ms) to its initial level, where λ_l and λ_r overlap, by the feedback loop (blue line). Note that, although the SNR at 50 pm detuning is reduced to less than 5, the control system is still able to keep the microring locked. The beneficial effect of the feedback loop is confirmed when the control is switched off (red lines) in fact, in both cases, as λ_l shifts, the optical intensity in the resonator drops and is never compensated, having the laser wavelength completely outside of the resonator linewidth.

Although the speed of the control loop achieved here is well enough to counteract most of the drifts (thermal and others) experienced by Si photonic microrings, it can be significantly increased either with suitable control laws (such as proportional or proportional-integral) or by enlarging the CLIPP readout bandwidth. For instance, while keeping the current CLIPP bandwidth ($B_d = 100$ Hz), if a proportional controller with gain of few thousands is utilized, a loop with time constant down to hundreds of microsecond is achieved (see Supplement 1 for details), yet at the price of larger voltage variations at the thermal actuator. On the other side, while maintaining an integral controller, the loop frequency can be increased by using a larger CLIPP bandwidth, yet at the price of larger noise (though typically depending on the square root of the bandwidth). The SNR can be preserved by increasing V_e accordingly.

6. SWAPPING THE MICRORING RESONANT WAVELENGTH

Although the CLIPP is in general a broadband light observer, here we show that it is able to simultaneously monitor and discriminate optical signals at different wavelengths. To this aim, we inject in the microring two different signals with wavelengths $\lambda_1 = 1549.59$ nm and $\lambda_2 = \lambda_1 + 120$ pm, labeled respectively with red and green arrows in Fig. 6. A weak modulation tone, with depth 2%, is added to label each of the optical carriers by means of an external modulator. The tone centered around λ_1 has frequency $f_1 = 10$ kHz whereas the other one, centered around λ_2, has frequency $f_2 = 11$ kHz (the tones are labeled, respectively, with red circle and green triangle in Fig. 6). The optical intensity observed in the resonator by the CLIPP is shown in Fig. 6 as a function of the electrical power dissipated by the heater. When the CLIPP electrical signal is demodulated at the usual frequency $f_e = 1$ MHz, the intracavity optical intensity reports two peaks associated with the transmission of both signals λ_1 and λ_2 [blue line in Fig. 6(a)] that are therefore indistinguishable. Vice versa, if the readout operations are performed at frequency $f_e + f_1 = 1.010$ MHz, the CLIPP is able to identify the signal at λ_1, where the modulation tone at frequency f_1 is added. In fact, as shown in Fig. 6(b) with the red line, the resonant peak measured by the CLIPP is centered on the first

signal (red arrow), whereas no evidence of λ_2 is found (green arrow). Similarly, if the electric signal is demodulated at frequency $f_e + f_2 = 1.011$ MHz, the measured resonant peak is centered on the second signal (green arrow), identified by the CLIPP as wavelength λ_2. It is straightforward now to tune and lock the microring resonant wavelength to that of the first signal λ_1 (λ_2), and then easily swap it to that of the second signal λ_2 (λ_1). Furthermore, it is worth noticing that wavelength-swapping operations can be performed by the CLIPP simultaneously on an arbitrarily large number of wavelengths using several modulation tones and by suitably demodulating the different signals. The same labeling approach can be used to manage many signals at the same wavelength but different light polarizations [16], or combined according to mode-division multiplexing schemes in multimode optical waveguides [25].

7. CONCLUSION

We have demonstrated non-invasive monitoring and advanced control functionalities in Si photonic microring resonators, assisted by a fully transparent light detector directly integrated inside the cavity. Through a CMOS microelectronic circuit [17] bridged to the Si photonic chip, the resonant wavelength of the microring is automatically tuned and locked against wavelength drifts of the optical signal. The non-invasive nature of the CLIPP enables real-time inspection of the intracavity light intensity without affecting the quality factor of the resonator. Therefore, the CLIPP can be used as a transparent detector for the realization of local feedback loops [14], thus making the control of devices integrated into complex circuits as if they were stand-alone.

Furthermore, the CLIPP is able to monitor and discriminate suitably labeled signals, allowing one to tune and lock photonic devices to the wavelength of a channel, regardless of the presence of other signals, simultaneously coexisting in the same photonic device. In the fabricated devices, feedback control is achieved through thermal actuators but the proposed tuning and locking schemes, and the CLIPP concept itself, can be adopted with any available actuator technology.

Finally, the possibility of managing feedback-controlled photonics through standard CMOS electronics makes the presented approach directly exploitable in system-level applications. The compactness and scalability of CMOS electronics to multichannel readout systems allows one also to extend the presented approach to the control of complex integrated circuits hosting many photonic components.

FUNDING INFORMATION

European Commission (EC) (BBOI (n. 323734)).

ACKNOWLEDGMENTS

The authors are grateful to the staff of the James Watt Nanofabrication Centre (JWNC) at the University of Glasgow for the fabrication of the Si photonic sample, and to Giovanni Bellotti from Politecnico di Milano for support during the measurements.

†S.G. and M.C. contributed equally to this work.

See Supplement 1 for supporting content.

REFERENCES

1. R. Chau, B. Doyle, S. Datta, J. Kavalieros, and K. Zhang, "Integrated nanoelectronics for the future," Nat. Mater. **6**, 810–812 (2007).
2. R. Gonzalez, B. M. Gordon, and M. A. Horowitz, "Supply and threshold voltage scaling for low power CMOS," IEEE J. Solid-State Circuits **32**, 1210–1216 (1997).
3. J. Sun, E. Timurdogan, A. Yaacobi, E. S. Hosseini, and M. R. Watts, "Large-scale nanophotonic phased array," Nature **493**, 195–199 (2013).
4. F. Morichetti, S. Grillanda, and A. Melloni, "Toward feedback-controlled integrated photonics," IEEE Photon. J. **6**, 1–6 (2014).
5. F. Xia, L. Sekaric, and Y. Vlasov, "Ultracompact optical buffers on a silicon chip," Nat. Photonics **1**, 65–71 (2007).
6. B. Guha, A. Gondarenko, and M. Lipson, "Minimizing temperature sensitivity of silicon Mach–Zehnder interferometers," Opt. Express **18**, 1879–1887 (2010).
7. K. Padmaraju, D. F. Logan, T. Shiraishi, J. J. Ackert, A. P. Knights, and K. Bergman, "Wavelength locking and thermally stabilizing microring resonators using dithering signals," J. Lightwave Technol. **32**, 505–512 (2014).
8. J. A. Cox, A. L. Lentine, D. C. Trotter, and A. L. Starbuck, "Control of integrated micro-resonator wavelength via balanced homodyne locking," Opt. Express **22**, 11279–11289 (2014).
9. K. Padmaraju, J. Chan, L. Chen, M. Lipson, and K. Bergman, "Thermal stabilization of a microring modulator using feedback control," Opt. Express **20**, 27999–28008 (2012).
10. K. Padmaraju, D. F. Logan, X. Zhu, J. J. Ackert, A. P. Knights, and K. Bergman, "Integrated thermal stabilization of a microring modulator," Opt. Express **21**, 14342–14350 (2013).
11. W. A. Zortman, A. L. Lentine, D. C. Trotter, and M. R. Watts, "Bit-error-rate monitoring for active wavelength control of resonant modulators," IEEE Micro **33**, 42–52 (2013).
12. T. Baehr-Jones, T. Pinguet, P. Lo Guo-Qiang, S. Danziger, D. Prather, and M. Hochberg, "Myths and rumours of silicon photonics," Nat. Photonics **6**, 206–208 (2012).
13. D. A. B. Miller, "Designing linear optical components," Opt. Photon. News **24**(12), 38 (2013).
14. D. A. B. Miller, "Self-configuring universal linear optical component," Photon. Res. **1**, 1–15 (2013).
15. J. K. Doylend and A. P. Knights, "The evolution of silicon photonics as an enabling technology for optical interconnection," Laser Photon. Rev. **6**, 504–525 (2012).
16. F. Morichetti, S. Grillanda, M. Carminati, G. Ferrari, M. Sampietro, M. J. Strain, M. Sorel, and A. Melloni, "Non-invasive on-chip light observation by contactless waveguide conductivity monitoring," IEEE J. Sel. Top. Quantum Electron. **20**, 1–10 (2014).
17. P. Ciccarella, M. Carminati, G. Ferrari, D. Bianchi, S. Grillanda, F. Morichetti, A. Melloni, and M. Sampietro are preparing a manuscript to be called "Impedance sensing CMOS chip for non-invasive light detection in integrated photonics."
18. M. Gnan, S. Thoms, D. S. Macintyre, R. M. De La Rue, and M. Sorel, "Fabrication of low-loss photonic wires in silicon-on-insulator using hydrogen silsesquioxane electron-beam resist," Electron. Lett. **44**, 115–116 (2008).
19. T. Baehr-Jones, M. Hochberg, and A. Scherer, "Photodetection in silicon beyond the band edge with surface states," Opt. Express **16**, 1659–1668 (2008).
20. W. Monch, *Semiconductor Surfaces and Interfaces* (Springer-Verlag, 2001).

21. H. Chen, X. Luo, and A. W. Poon, "Cavity-enhanced photocurrent generation by 1.55 μm wavelengths linear absorption in a p-i-n diode embedded silicon microring resonator," Appl. Phys. Lett. **95**, 171111 (2009).
22. J. D. B. Bradley, P. E. Jessop, and A. P. Knights, "Silicon waveguide integrated optical power monitor with enhanced sensitivity at 1550 nm," Appl. Phys. Lett. **86**, 241103 (2005).
23. M. W. Geis, S. J. Spector, M. E. Grein, R. T. Schulein, J. U. Yoon, D. M. Lennon, S. Deneault, F. Gan, F. X. Kaertner, and T. M. Lyszczarz, "CMOS-compatible all-Si high-speed waveguide photodiodes with high responsivity in near-infrared communication band," IEEE Photon. Technol. Lett. **19**, 152–154 (2007).
24. E. Timurdogan, C. M. Sorace-Agaskar, J. Sun, E. S. Hosseini, A. Biberman, and M. R. Watts, "An ultralow power athermal silicon modulator," Nat. Commun. **5**, 4008 (2014).
25. L. W. Luo, N. Ophir, C. P. Chen, L. H. Gabrielli, C. B. Poitras, K. Bergman, and M. Lipson, "WDM-compatible mode-division multiplexing on a silicon chip," Nat. Commun. **5**, 3069 (2014).

Research Article Vol. 1, No. 3 / September 2014 / Optica 137

Investigation of mode coupling in normal-dispersion silicon nitride microresonators for Kerr frequency comb generation

Yang Liu,[1] Yi Xuan,[1,2] Xiaoxiao Xue,[1] Pei-Hsun Wang,[1] Steven Chen,[1] Andrew J. Metcalf,[1] Jian Wang,[1,2] Daniel E. Leaird,[1] Minghao Qi,[1,2] and Andrew M. Weiner[1,2,*]

[1]School of Electrical and Computer Engineering, Purdue University, 465 Northwestern Avenue, West Lafayette, Indiana 47907-2035, USA

[2]Birck Nanotechnology Center, Purdue University, 1205 West State Street, West Lafayette, Indiana 47907, USA

*Corresponding author: amw@purdue.edu

Received 23 May 2014; revised 21 July 2014; accepted 23 July 2014 (Doc. ID 212661); published 29 August 2014

Kerr frequency combs generated from microresonators are the subject of intense study for potential applications ranging from short pulse generation to frequency metrology to radiofrequency signal processing. Most research employs microresonators with anomalous dispersion, for which modulation instability is believed to play a key role in initiation of the comb. Comb generation in normal-dispersion microresonators has also been reported but is less well understood. Here, we report a detailed investigation of few-moded, normal-dispersion silicon nitride microresonators, showing that mode coupling can strongly modify the local dispersion, even changing its sign. We demonstrate a link between mode coupling and initiation of comb generation by showing experimentally the pinning of one of the initial comb sidebands near a mode-crossing frequency. Associated with this route to comb formation, we observe direct generation of coherent, bandwidth-limited pulses at repetition rates down to 75 GHz, without the need to first pass through a chaotic state. Our results with normal-dispersion devices highlight mode interactions as a beneficial tool for comb initiation and pulse formation.

OCIS codes: (130.3990) Micro-optical devices; (140.4780) Optical resonators; (190.4360) Nonlinear optics, devices.

http://dx.doi.org/10.1364/OPTICA.1.000137

Recently, high quality factor (Q) microresonators have been intensively investigated for optical comb generation. Both whispering gallery mode (WGM) resonators employing tapered fiber coupling and chip-scale microresonators employing monolithically fabricated coupling waveguides are popular. Tuning a continuous-wave (CW) laser into resonance leads to buildup of the intracavity power and enables additional cavity modes to oscillate through cascaded four-wave mixing (FWM) [1–15]. Modulational instability (MI) of the CW pump mode is commonly cited as an important mechanism for comb generation [16–18]. According both to experiment and to theoretical analysis, comb generation preferably occurs in resonators with anomalous dispersion. However, comb generation in resonators characterized with normal dispersion has also been observed experimentally [5,8,19–27]. Several models have been proposed to describe this phenomenon. Although MI gain is missing in fibers or waveguides with normal dispersion, when it comes to resonators, the detuning provides an extra degree of freedom which enables MI to take place in the normal dispersion regime, hence providing a route to comb generation [16,18,25]. However, this mechanism requires either a precise relationship between detuning and pump power, making it difficult to realize practically, or hard excitation, a nonadiabatic process under which pump photons must be initially present in the resonator [17].

Mode coupling has also been suggested as a mechanism enabling comb generation in resonators with normal dispersion

[26]. When resonances corresponding to different families of transverse modes approach each other in frequency, they may interact due to imperfections in the resonator. The theory of mode coupling in resonators has been well-established [28], and frequency shifts and avoided crossings have been observed [29–35]. In the anomalous-dispersion regime, mode coupling has been reported to affect the bandwidth scaling of frequency combs [36] and the process of soliton formation [37]. However, in these cases, anomalous dispersion is still considered to be the determining factor for comb generation; mode coupling is considered to be detrimental, inhibiting the formation of solitons and limiting comb bandwidth. In the normal-dispersion regime, measurements have been performed with CaF_2 WGM resonators [26]. The experiments demonstrate strong local frequency shifts that are attributed to mode interactions and show a correlation between the presence of such local frequency shifts and the ability to generate combs in these normal-dispersion resonators. Significant changes in comb spectra have been observed when pumping different longitudinal modes spaced by only a few free spectral ranges (FSRs), both in normal-dispersion silicon nitride microring resonators [5] and in the WGM resonators of [26]; in the latter case, such effects were specifically attributed to mode interactions.

In the current report, we perform comb-assisted precision spectroscopy measurements [38] of few-moded silicon nitride microresonators in the normal-dispersion regime over frequency ranges spanning dozens of FSRs. As a result, we are able to clearly map out mode interactions and obtain plots of resonant frequencies exhibiting strong avoided crossings closely analogous to those that occur for quantum mechanical energy surfaces [39–41]. The frequency shifts affecting a series of resonances from both mode families can lead to a strong change in local dispersion, even changing its sign. We provide clear experimental evidence that this mode coupling plays a major role in the comb-generation process for our normal-dispersion resonators by showing experimentally, for the first time to our knowledge, that the location of one of the two initial sidebands at the onset of comb generation is "pinned" at a mode-crossing frequency, even as the pump wavelength is changed substantially [42].

These effects allow us to realize a "Type I" comb [5], also termed a natively mode-spaced (NMS) comb [43], in a resonator with FSR slightly under 75 GHz. In such a comb, the initial sidebands are generated via a soft excitation mechanism and are spaced one FSR from the pump; the comb exhibits low noise and high coherence immediately upon generation [5,20–22,36,43,44]. We also find that the Type I comb as generated here corresponds directly to a train of bandwidth-limited pulses. This is in sharp contrast to "Type II" combs [5] (also termed multiple mode-spaced combs [43]) for which the initial sidebands are separated from the pump by several FSRs, after which additional, closer sidebands are generated (usually with increasing intracavity power) to arrive at single-FSR spacing. Such Type II combs exhibit poor coherence and high noise [5,21,43,45]. Mode-locking transitions in which Type II combs switch into a coherent, low-noise state have been observed experimentally and studied theoretically [17,23–25,37,43,46–58]. However, these methods require careful and sometimes complex tuning of the pump frequency or power [37]; the mode-locking transition is often difficult to achieve and until very recently has not been observed in normal-dispersion microresonators. Our recent demonstration of dark soliton formation in resonators with normal dispersion is linked to a mode-locking transition [23], but the waveforms generated are quite distinct from the bandwidth-limited pulses reported here.

The field in the microresonators can be expressed using the following mode coupling equations:

$$\frac{dE_1}{dt} = \left(-\frac{1}{\tau_{o1}} - \frac{1}{\tau_{e1}} - j\delta_1\right)E_1 + j\kappa_{12}E_2 + \sqrt{\frac{2}{\tau_{e1}}}E_0, \quad \textbf{(1a)}$$

$$\frac{dE_2}{dt} = \left(-\frac{1}{\tau_{o2}} - \frac{1}{\tau_{e2}} - j\delta_2\right)E_2 + j\kappa_{21}E_1 + \sqrt{\frac{2}{\tau_{e2}}}E_0. \quad \textbf{(1b)}$$

Here, E_1 and E_2 are the intracavity fields for mode 1 and 2, respectively; $1/\tau_{o1}$ and $1/\tau_{o2}$ are decay rates due to the intrinsic loss for both modes, while $1/\tau_{e1}$ and $1/\tau_{e2}$ are coupling rates between the resonator and the bus waveguides. $\delta_1 = \omega - \omega_1$ and $\delta_2 = \omega - \omega_2$ are the frequency detunings, where ω_1 and ω_2 are the resonant frequencies. $\kappa_{12} = \kappa_{21}^* = \kappa$ are mode coupling coefficients. We can simulate mode interaction effects using the mode-coupling equations. Two modes are assumed working close to 1550 nm in the resonator with $\tau_{o1} = 2.79 \times 10^{-9}$ s, $\tau_{e1} = 4.00 \times 10^{-9}$ s and $\tau_{o2} = 5.78 \times 10^{-10}$ s, $\tau_{e2} = 3.38 \times 10^{-9}$ s, respectively. This corresponds to two modes working in the undercoupling regime: mode 1 with loaded Q of 10^6, intrinsic Q of 1.70×10^6, and extinction ratio of 15 dB; and mode 2, with loaded Q of 3×10^5, intrinsic Q of 3.51×10^5, and extinction ratio of 3 dB. We solve Eq. (1) and plot the resulting transmission spectra for different separations (over the range −5 GHz–5 GHz) between the resonances of the two modes. Without mode coupling [$\kappa = 0$, Fig. 1(a)], the resonances approach and cross each other at a constant rate. However, with mode coupling turned on [$\kappa = j \cdot 8.25 \times 10^9$ s^{-1} compared with $1/\tau_{o1} = 3.58 \times 10^8$ s^{-1}, Fig. 1(b)], the dips in transmission are shifted in frequency, resulting in an avoided crossing. The mode interactions also lead to significant changes in the extinction ratios and linewidths of the resonant features. Similar effects are observed in our experiments, as we relate below.

Our experiments utilize silicon nitride resonators fabricated to have 2 μm × 550 nm waveguide cross-sections. According

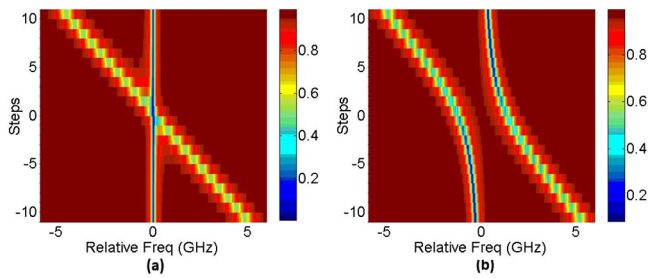

Fig. 1. Numerical investigation of mode-coupling effect when the resonances of the two modes get close and cross each other: (a) no mode coupling and (b) with mode coupling.

to simulation for two transverse electric (TE) modes TE_1 and TE_2, these waveguides are clearly in the normal-dispersion regime with $D \sim -156$ ps/nm · km and $D \sim -160$ ps/nm · km, respectively [20]. We first study a resonator with a total path length of 5.92 mm, which corresponds to a FSR slightly under 25 GHz. Similar to [14], to avoid the stitching error, we introduce a finger-shaped structure for the resonator so that it can fit in a single field of our electron beam lithography tool. Figure 2(a) shows a microscope image of the microresonator. The light is coupled both in and out through lensed fibers which are positioned in U-grooves to improve stability when working at high power [20]. Fiber-to-fiber coupling loss is ~5 dB. The measured transmission spectrum, showing resonances throughout the lightwave C band, is given in Fig. 2(b). If we zoom in the transmission spectrum as shown in the inset, resonances of two transverse mode families with different depth can be observed. The loaded Q factors at the frequencies shown are ca. 1×10^6 (intrinsic $Q \sim 1.7 \times 10^6$) and 0.3×10^6 (intrinsic $Q \sim 0.35 \times 10^6$) for modes 1 and 2, respectively.

We use the frequency-comb-assisted spectroscopy method of [38] to accurately determine the resonance positions and compute the changes in FSR with wavelength to estimate the dispersion for TE modes. The measured FSRs are given in Fig. 3(a). The FSRs for the two modes are around 24.8 and 24.4 GHz, respectively. Both modes are fitted with our simulated dispersion showing good accordance, which confirms that the resonator is in the normal-dispersion regime for TE modes with $D_2/2\pi \approx 474$ kHz, where $D_2/2\pi$ denotes the difference in FSR for adjacent resonances, which can be expressed as

$$\frac{D_2}{2\pi} = \lambda^2 \cdot n_{\text{eff}} \cdot \text{FSR}^2 \cdot D. \quad \textbf{(2)}$$

However, at several wavelengths for which the resonances associated with the two transverse modes are closely spaced (1532, 1542, and 1562 nm), the FSRs of the two modes change significantly, such that their FSRs become more similar. In these cases, we clearly observe that the mode coupling results in a major modification to the local dispersion, even changing the sign of dispersion in some wavelength regions. To take a closer look at this phenomenon, in Fig. 3(b), we plot the transmission spectrum in the vicinity of the mode-crossing regime near 1542 nm. To visualize the data in a form analogous to the simulations of Fig. 1, we vertically align different pieces of the transmission spectrum separated by a

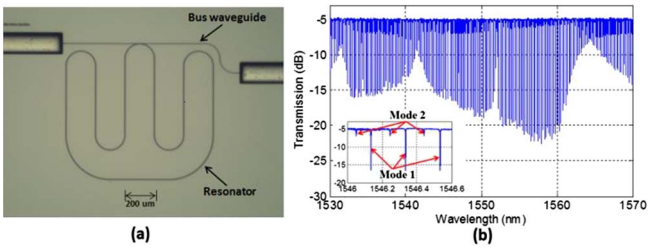

Fig. 2. (a) Microscope image of the silicon nitride resonator with path length of 5.92 mm. (b) Measured transmission spectrum of the resonator. Inset is the zoom-in transmission spectrum showing resonances from different transverse-mode families.

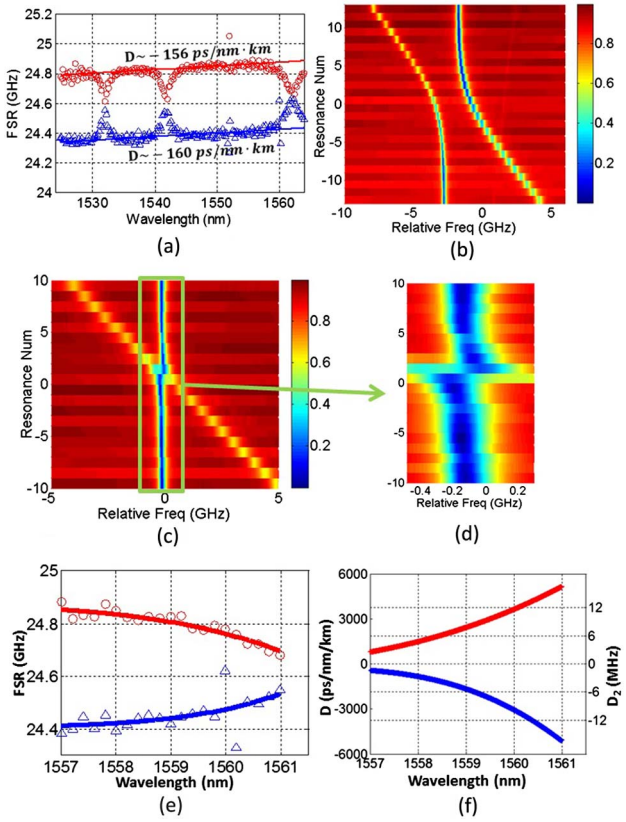

Fig. 3. (a) Measured FSR versus optical wavelength for two TE modes plotted in red circles and blue triangles and fitted with $D \sim -156$ ps/nm · km and $D \sim -160$ ps/nm · km, respectively. (b)–(d) Aligned resonances with fixed increment showing the mode coupling with different coupling strength. (b) Strong coupling case centered at 1542 nm with clear avoided crossings. (c) Weak coupling case centered at 1552 nm. (d) Zoomed-in view of the weak coupling case. (e) Zoom-in view and fitted FSR spectrum in a mode-crossing area. (f) Calculated D and corresponding D_2 value of mode 1 and mode 2 plotted in red and blue, respectively.

constant 24.82 GHz increment (the nominal FSR of the higher Q mode around 1542 nm). Since the average dispersion contributes a change in FSR below 15 MHz in the range plotted without mode coupling, one of the modes should appear as very nearly a vertical line, while the other should appear as a tilted line due to the difference in FSRs. However, in Fig. 3(b), we observe that the curves bend as they approach each other, resulting in an avoided crossing, similar to the simulation results of Fig. 1(b). Changes in the extinction ratio of the resonances are also clearly evident in the mode-interaction region. These data provide detailed and compelling evidence of strong mode-coupling effects on the linear spectrum.

A different case for the mode crossing is observed around 1552 nm. Here, there is no obvious change in FSR around the wavelength where the resonances of these modes get close. The aligned resonance pairs are shown in Fig. 3(c). The picture resembles the case shown in Fig. 1(a), where no mode coupling is assumed. However, if we zoom in on the data, we can again see slight shifts in the positions of the resonances when they are close enough. In this case, mode-coupling effects are present but weak. We have estimated the mode-coupling strength according to the shift of resonance positions for each of the

four mode crossings; the results are given in Table 1. The coupling strength ranges from 1.50×10^{10} at 1562 nm to 1.65×10^{9} at 1552 nm. We can also calculate the local dispersion of the two modes in the crossing region by fitting the FSR spectra and calculating their derivatives. The results for the strongest coupling case at 1562 nm are given in Figs. 3(e) and 3(f). We can see that for mode 1, the D value changes from around −156 ps/nm/km to over 5000 ps/nm/km. Not only does the magnitude increase by more than a decade, but also the sign changes from normal to anomalous. For mode 2, the magnitude of D changes by a similar amount. The D_2 value, however, remains below 20 MHz, which is less than the resonance linewidth (ca. 200 MHz). Hence, according to the analysis of [43], the dispersion is still not large enough to enforce Type I comb generation.

In comb generation experiments, we pumped the microresonator with a single CW input at 1.75 W (this is the value prior to the chip, without accounting for coupling loss) tuned to different resonances of the high-Q-mode family and recorded the comb spectra. The results are given in Fig. 4. In Fig. 4(a), we pump at 28 different resonances between 1554 and 1560 nm. The frequency spacing of the comb varies from 33 FSR for pumping at 1554 nm to 7 FSR for pumping at 1559.4 nm. We observe that the nearest long-wavelength sideband remains anchored at approximately 1560.5 nm, very close to the ∼1562 nm mode interaction feature. With the pump shifted by a total of 694 GHz (27 FSRs), we find that the long wavelength sideband varies by no more than ±25 GHz (±1 FSR). Meanwhile, the short wavelength sideband varies at twice the rate of the pump tuning, for a total frequency variation of ∼1.3 THz. Similar behavior is observed when we pump between 1546 and 1549.5 nm. As shown in Fig. 4(b), one of the sidebands is anchored near 1550.5 nm, close to the weaker 1552 nm mode interaction feature. In this case comb, generation is missing for some pump wavelengths, which may be the result of the weak coupling strength. Pinning of one of the sidebands at 1532 and 1542 nm has also been observed, but for a smaller number of pump wavelengths. The different mode interaction features may compete with each other in initializing the combs. Pinning around the 1562 nm mode interaction region, which has the strongest coupling strength, occurs for the largest number of pump wavelengths. The observed pinning of one of the initial sidebands very close to a mode interaction feature clearly suggests that mode coupling is a major factor in comb generation in this normal-dispersion microresonator.

According to the anomalous dispersion analysis of Ref. [43], increasingly large dispersion is needed to generate "NMS" (Type I) combs as the resonator FSR decreases. Physically, the

Table 1. Estimated Coupling Strength for Four Mode-Crossing Areas Shown in Fig. 3(a)

Wavelength(nm)	1532	1542	1552	1562
Coupling strength $\lvert\kappa\rvert$ (s^{-1})	6.50×10^{9}	8.25×10^{9}	1.65×10^{9}	1.50×10^{10}

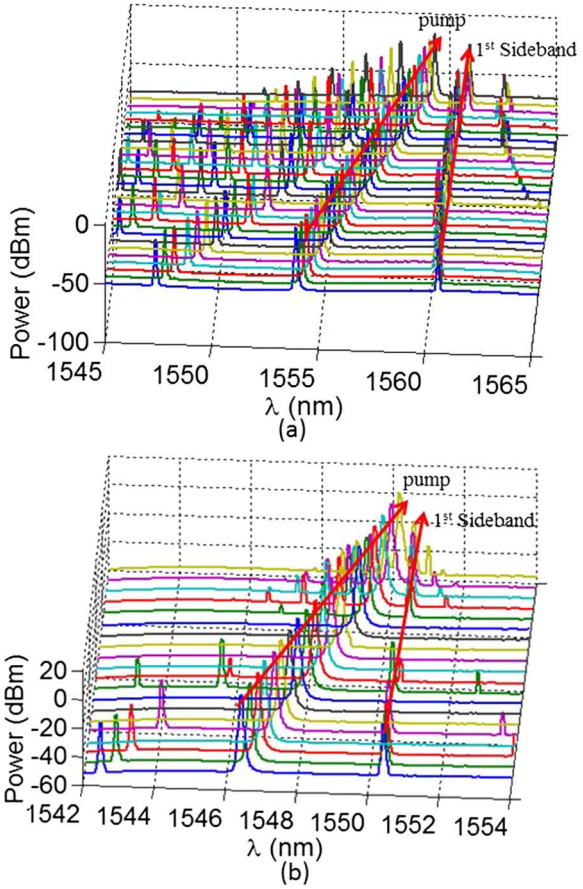

Fig. 4. Comb generation at different pump wavelength with one of the first sidebands kept at an approximately constant location (a) around 1560 nm and (b) around 1550 nm.

increased dispersion brings the MI gain peak closer to the pump. In order to reduce the gain peak to single FSR frequency offset, it was shown that the D_2 parameter should be made close to the resonance width (200 MHz for silicon nitride resonators with $Q \sim 10^6$). For example, for a resonator with FSR ∼100 GHz, the dispersion required for the generation of a Type I comb would be $D \approx 4.2 \times 10^3$ ps · nm^{-1} · km^{-1}. Furthermore, according to Eq. (2), the dispersion required grows quadratically as the resonator size is further increased (required D grows as the inverse square of the FSR). Such dispersions are generally too large to achieve practically; perhaps, as a result, no observation of Type I comb generation in sub-100-GHz silicon nitride resonators has been reported. However, mode coupling can dramatically change the local dispersion, both increasing its magnitude and changing its sign. Generation of Type I combs from large WGM resonators has previously been reported and attributed to mode coupling [25,26]. In our experiments, we have observed Type I comb generation in SiN for a resonator with a FSR slightly below 75 GHz. We have not yet obtained a NMS comb from resonators with even smaller FSR. However, as shown in Fig. 4(b), a comb with 2 FSR separation is observed when the 25 GHz FSR resonator is pumped at 1550.41 nm. This means that the first sideband is less than 50 GHz from the pump, which is still very difficult to achieve without mode-coupling effects.

The fabricated ~75 GHz FSR resonator is shown in Fig. 5(a). Unlike the 25 GHz resonator discussed earlier, it has a drop-port design which has been observed to reduce the power difference between the pump and adjacent comb lines, yielding a smoother comb spectrum without the usual strong pump background [20]. Using the frequency-comb-assisted spectroscopy method, two mode families with FSRs around 74.7 and 72 GHz are observed. The two families of resonances approach each other around 1563 nm. Different sections of the transmission spectrum are aligned in a similar fashion as for Figs. 3(b)–3(d) and plotted in Fig. 5(b). An avoided crossing evidencing mode coupling is clearly observed. The comb results are shown in Fig. 5(c) for pumping between 1554.71 and 1566.59 nm. Again, one of the first sidebands is "pinned" near the mode-crossing wavelength. Although the first sideband has a 13 FSR separation when pumping at 1555 nm, a Type I comb can be generated for pumping at 1562.62, 1563.22, 1563.81, and 1564.43 nm (as shown in the circled area). We note that in this case, pinning of the first sideband is observed for pumping at either the blue side or the red side of the mode-crossing area. Very close to the mode interaction region, the estimated D_2 can be increased to over 200 MHz, which is on the order of resonance linewidth. This satisfies the dispersion requirement for Type I comb generation as predicted in Ref. [43].

As an example, pumping at 1562.62 nm with 1.6 W input, more than 20 comb lines with 1 FSR separation are generated. The spectrum observed at the drop port is shown in Fig. 6(a). Fifteen of the lines are selected by a bandpass filter and amplified in an erbium-doped fiber amplifier (EDFA); the resulting spectrum is shown in Fig. 6(b). The amplified and filtered comb is directed to an intensity autocorrelator based on second-harmonic generation in a noncollinear geometry. A length of dispersion compensating fiber (DCF) is used to achieve dispersion compensation of the entire fiber link (including the EDFA) connecting the SiN chip to the autocorrelator. The length of DCF was adjusted by injecting a short-pulse laser from a passively mode-locked fiber laser into the front end of the fiber link and minimizing its autocorrelation width. The autocorrelation trace measured for the comb is plotted in Fig. 6(c). Also plotted is the autocorrelation of the ideal bandwidth-limited pulse, calculated from the spectrum of Fig. 6(b) with the assumption of flat phase. Clearly the generated pulses, with estimated duration of 2.7 ps FWHM, are very close to bandwidth-limited. We have also used a photodetector and spectrum analyzer to look at the low frequency intensity noise of the comb (measurement bandwidth: ~500 MHz). The intensity noise is below the background level of our measurement setup. Similar low noise, bandwidth-limited pulse generation is observed for the "Type I" combs generated via pumping at other resonances of this same resonator. These data demonstrate that the Type I combs reported here are generated *directly* in a mode-locked state featuring low noise, high coherence, and bandwidth-limited temporal profile, though with a limited number of comb lines.

To better understand the comb-generation behavior as influenced by mode coupling, we performed simulations for our 75 GHz microresonator using the Lugiato–Lefever (L–L) equation [23,46,47,59]. As suggested by Ref. [26], we introduced phase shift terms to model the effect of mode interaction. Here, we introduced phase shifts to the four resonances (numbered –1 to 2 with reference to Fig. 7), which experience the largest frequency shifts due to the mode coupling. The phase shifts are selected by normalizing the measured resonance frequency shifts by the FSR value; 2π shift in phase corresponds to a 1 FSR change of resonance frequency. As

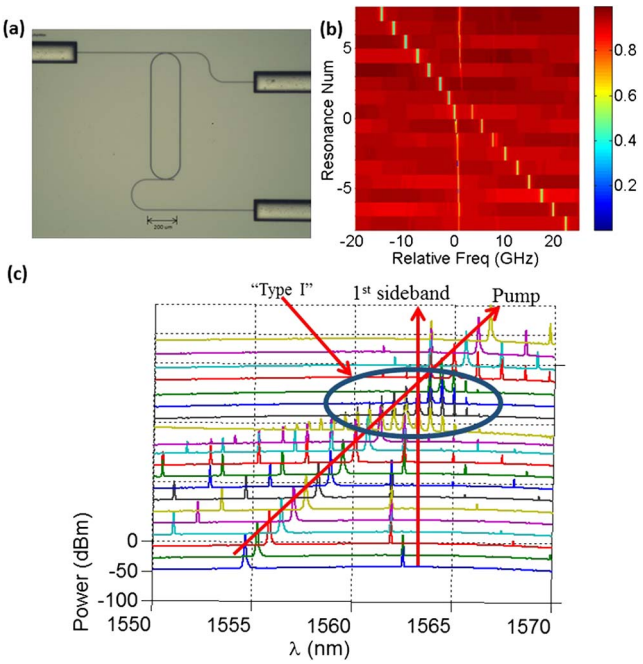

Fig. 5. (a) Microscope image of the silicon nitride resonator with path length of 1.97 mm. (b) Aligned resonances centered at 1563 nm with fixed increment showing the mode coupling. (c) Comb generation at different pump wavelength; one of the first sidebands remains close to 1563 nm.

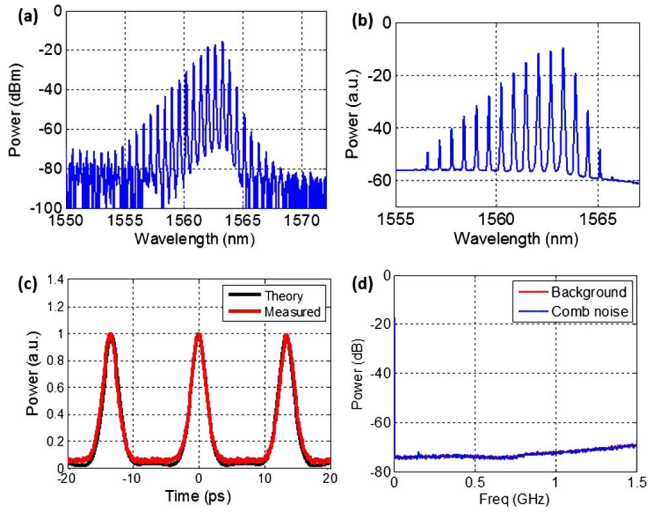

Fig. 6. Generation of coherent mode-locked Type I comb due to the mode coupling. (a) Generated comb spectrum at the drop port. (b) Fifteen lines are selected, amplified, and filtered for time domain characterization. (c) Autocorrelation of time domain pulse compared with that of theoretical bandwidth-limited pulse, showing good coherence and mode-locking behavior. (d) Intensity noise compared with the measurement system noise floor.

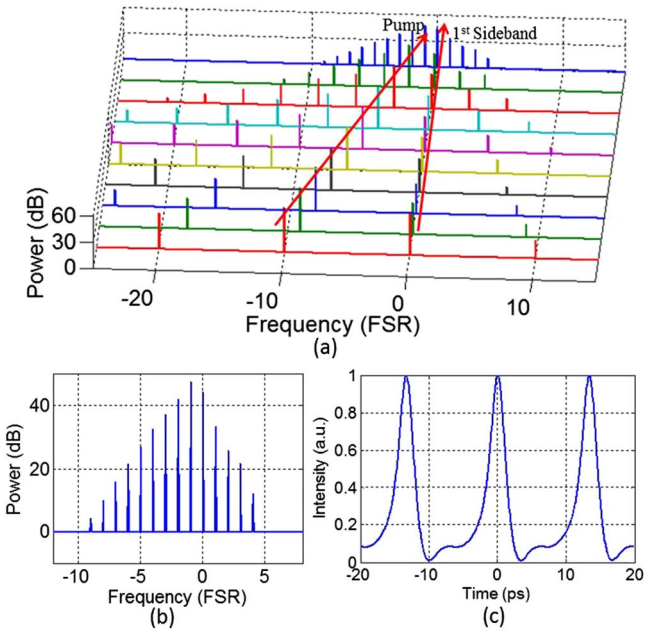

Fig. 7. (a) Simulated comb generation pumping at different resonances in normal-dispersion microresonator with mode coupling. (b) and (c) Simulated mode coupling initialized Type I comb spectrum and its intracavity intensity, respectively.

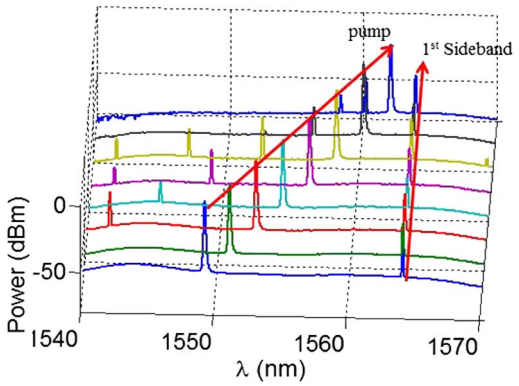

Fig. 8. Observation of "Pinned" first sidebands for the resonator with passively mode locked "Type I" comb as discussed in Ref. [20].

shown in Fig. 7(a), the resonator is pumped at different resonances; one of the sidebands stays pinned at the resonance with the largest phase shift [denoted frequency 0 in Fig. 7(a)]. A type I comb is observed for pumping at an adjacent resonance; the resulting spectrum is shown in Fig. 7(b). We note that the resonance frequency shifts are measured under cold cavity conditions with very low input optical power. In comb generation experiments, the optical powers are much higher; thermal and other nonlinear effects shift the positions of the resonances (usually leading to a blue shift). Furthermore, the different modes are expected to shift at somewhat different rates. This effect, which would modify the frequency offsets of the interacting modes compared to our low-power transmission measurements, is not considered in our simulation. This may explain why in the simulation the pinned sideband is fixed at one specific resonance, while in experiment the sideband is pinned more loosely [moves by about ±1 FSR in Fig. 5(c)].

Our group has previously reported direct Type I generation, with behavior similar to that shown in Fig. 6, from a smaller, normal-dispersion SiN microresonator with ~230 GHz FSR [20]. Although we speculated that mode interactions may have played a role in allowing comb generation, as pointed out theoretically in [26], we were unable to present data to support this speculation. Based on the insight developed in the current work, we decided to reexamine our data from the device of [20]. Figure 8 shows the comb spectra obtained for pump powers just above threshold, plotted in the same fashion as Figs. 4 and 5(c). This format clearly shows pinning of one of the initial sidebands, revealing what we now understand to be a signature of comb initiation through mode coupling.

The pathway to coherent pulse generation reported here is clearly distinct from that observed in Refs. [23,24,37,45], which attain broader comb bandwidths but need to navigate through a chaotic state before arriving at a transition to mode locking. A theoretical explanation for the observed direct generation of approximately bandwidth-limited pulses is still not fully available. The intracavity field corresponding to the Type I comb in the simulation results of Fig. 7(b) does correspond to single pulses in each time period [Fig. 7(c)]. However, the pulses from simulation are not fully bandwidth-limited; the comb field is phase modulated and temporally broadened (the corresponding autocorrelation trace has a FWHM of 4.53 ps compared to 3.6 ps of the bandwidth-limited pulse). This discrepancy suggests some factors may be missing in the model. One possibility is that a heretofore unidentified nonlinear amplitude modulation mechanism may be present, as suggested briefly in Refs. [20,43]. Mode interactions may contribute to such a mechanism, since a superposition of transverse modes leads to a longitudinally modulated spatial profile which may either increase or decrease overlap with waveguide imperfections. Nonlinearity could shift such spatial profiles, under appropriate circumstances reducing loss, analogous to decreased loss through nonlinear lensing in Kerr lens mode-locked lasers. Another possibility suggested in Ref. [24] is that a broad wavelength dependence of the resonator Q introduces a spectral filtering effect which contributes to shaping the time domain field. However, in our resonators, a similar variation of the Q factor is not observed (although some variations in Q do appear to be induced around the mode-coupling region).

Finally, we note that previous studies have associated mode coupling with asymmetric comb spectra [19,26]. However, mode-interaction spectra such as those in Figs. 3 and 5 were neither reported nor registered with the generated combs. In our experiments, asymmetric spectra were observed for both resonators studied; Fig. 9 shows four examples with the mode interaction region identified through the pinned first sideband. For the resonator with ~25 GHz FSR, the separations between the pump and the first sideband are 15 and 2 FSR in Figs. 9(a) and 9(b), respectively; for the ~75 GHz FSR resonator, the pump position is changed from the short-wavelength side of the coupling region [Fig. 9(c)] to the long-wavelength side [Fig. 9(d)]. In each case, the first sideband "pinned" close to the mode crossing has higher power than the first sideband on the other side of the pump. However,

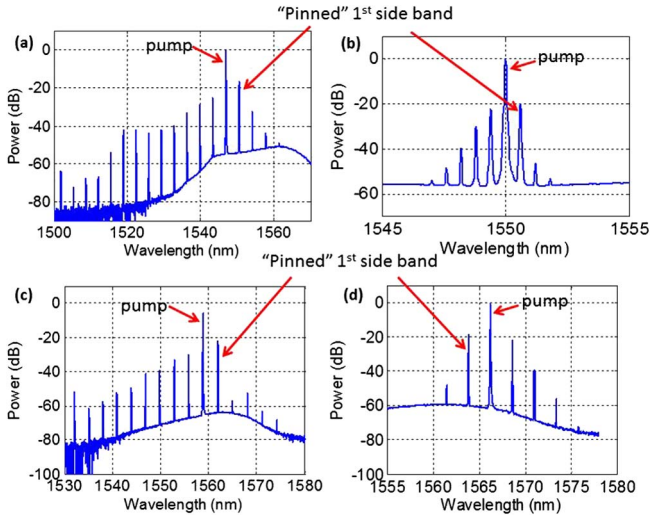

Fig. 9. Asymmetric comb spectra. (a) and (b) Comb generation using resonators with ~25 GHz FSR with "pinned" sideband close to 1551 nm, (c) and (d) comb generation using resonators with ~75 GHz FSR with "pinned" sideband close to 1563 nm.

fewer comb lines are generated on the side of the pump corresponding to the pinned sideband. We may understand this behavior by noting that flattened dispersion is favorable for broadband comb generation [13,33,50,60]. In our experiments, mode coupling modifies the local dispersion, allowing MI gain for initiation of comb generation but at the same time giving rise to significant higher-order dispersion that limits growth of the comb bandwidth on the mode-interaction side. Since approximately bandwidth-limited pulses are generated directly, it may be possible to obtain wider bandwidths through amplification and spectral broadening in nonlinear fiber, without the need for intermediate pulse shaping.

In summary, we have demonstrated what we believe to be conclusive evidence of the impact of mode coupling on initiation of comb generation in normal-dispersion silicon nitride microresonators. We have also demonstrated mode-coupling-assisted "Type I" comb generation resulting in direct generation of bandwidth-limited pulses, without the need to navigate through a chaotic state.

FUNDING INFORMATION

National Science Foundation (NSF) (ECCS-1102110, ECCS-1126314); Air Force Office of Scientific Research (FA9550-12-1-0236); Defense Advanced Research Projects Agency (DARPA) (W31P40-13-1-0018).

REFERENCES

1. P. Del'Haye, A. Schliesser, O. Arcizet, T. Wilken, R. Holzwarth, and T. J. Kippenberg, "Optical frequency comb generation from a monolithic microresonator," Nature **450**, 1214–1217 (2007).
2. T. J. Kippenberg, R. Holzwarth, and S. A. Diddams, "Microresonator-based optical frequency combs," Science **332**, 555–559 (2011).
3. J. S. Levy, A. Gondarenko, M. A. Foster, A. C. Turner-Foster, A. L. Gaeta, and M. Lipson, "CMOS-compatible multiple-wavelength oscillator for on-chip optical interconnects," Nat. Photonics **4**, 37–40 (2009).
4. L. Razzari, D. Duchesne, M. Ferrera, R. Morandotti, S. Chu, B. E. Little, and D. J. Moss, "CMOS-compatible integrated optical hyper-parametric oscillator," Nat. Photonics **4**, 41–45 (2009).
5. F. Ferdous, H. Miao, D. E. Leaird, K. Srinivasan, J. Wang, L. Chen, L. T. Varghese, and A. M. Weiner, "Spectral line-by-line pulse shaping of on-chip microresonator frequency combs," Nat. Photonics **5**, 770–776 (2011).
6. P. Del'Haye, T. Herr, E. Gavartin, R. Holzwarth, and T. J. Kippenberg, "Octave spanning tunable frequency comb from a microresonator," Phys. Rev. Lett. **107**, 063901 (2011).
7. I. S. Grudinin, N. Yu, and L. Maleki, "Generation of optical frequency combs with a CaF_2 resonator," Opt. Lett. **34**, 878–880 (2009).
8. A. A. Savchenkov, A. B. Matsko, V. S. Ilchenko, I. Solomatine, D. Seidel, and L. Maleki, "Tunable optical frequency comb with a crystalline whispering gallery mode resonator," Phys. Rev. Lett. **101**, 093902 (2008).
9. C. Y. Wang, T. Herr, P. Del'Haye, A. Schliesser, J. Hofer, R. Holzwarth, T. W. Hänsch, N. Picqué, and T. J. Kippenberg, "Mid-infrared optical frequency combs at 2.5 μm based on crystalline microresonators," Nat. Commun. **4**, 1345 (2013).
10. W. Liang, A. A. Savchenkov, A. B. Matsko, V. S. Ilchenko, D. Seidel, and L. Maleki, "Generation of near-infrared frequency combs from a MgF_2 whispering gallery mode resonator," Opt. Lett. **36**, 2290–2292 (2011).
11. I. H. Agha, Y. Okawachi, and A. L. Gaeta, "Theoretical and experimental investigation of broadband cascaded four-wave mixing in high-Q microspheres," Opt. Express **17**, 16209–16215 (2009).
12. M. A. Foster, J. S. Levy, O. Kuzucu, K. Saha, M. Lipson, and A. L. Gaeta, "Silicon-based monolithic optical frequency comb source," Opt. Express **19**, 14233–14239 (2011).
13. Y. Okawachi, K. Saha, J. S. Levy, Y. H. Wen, M. Lipson, and A. L. Gaeta, "Octave-spanning frequency comb generation in a silicon nitride chip," Opt. Lett. **36**, 3398–3400 (2011).
14. A. R. Johnson, Y. Okawachi, J. S. Levy, J. Cardenas, K. Saha, M. Lispon, and A. L. Gaeta, "Chip-based frequency combs with sub-100 GHz repetition rates," Opt. Express **37**, 875–877 (2012).
15. H. Jung, C. Xiong, K. Y. Fong, X. Zhang, and H. X. Tang, "Optical frequency comb generation from aluminum nitride microring resonator," Opt. Lett. **38**, 2810–2813 (2013).
16. A. B. Matsko, A. A. Savchenkov, D. Strekalov, V. S. Ilchenko, and L. Maleki, "Optical hyperparametric oscillations in a whispering-gallery-mode resonator: threshold and phase diffusion," Phys. Rev. A **71**, 033804 (2005).
17. A. B. Matsko, A. A. Savchenkov, V. S. Ilchenko, D. Seidel, and L. Maleki, "Hard and soft excitation regimes of Kerr frequency combs," Phys. Rev. A **85**, 023830 (2012).
18. T. Hansson, D. Modotto, and S. Wabnitz, "Dynamics of the modulational instability in microresonator frequency combs," Phys. Rev. A **88**, 023819 (2013).
19. A. A. Savchenkov, E. Rubiola, A. B. Matsko, V. S. Ilchenko, and L. Maleki, "Phase noise of whispering gallery photonic hyperparametric microwave oscillators," Opt. Express **16**, 4130–4144 (2008).
20. P. Wang, Y. Xuan, L. Fan, L. T. Varghese, J. Wang, Y. Liu, X. Xue, D. E. Leaird, M. Qi, and A. M. Weiner, "Drop-port study of microresonator frequency combs: power transfer, spectra and time-domain characterization," Opt. Express **21**, 22441–22452 (2013) and erratum, Opt. Express 22, 12148 (2014).
21. P.-H. Wang, F. Ferdous, H. Miao, J. Wang, D. E. Leaird, K. Srinivasan, L. Chen, V. Aksyuk, and A. M. Weiner, "Observation of correlation between route to formation, coherence, noise, and communication performance of Kerr combs," Opt. Express **20**, 29284–29295 (2012).
22. F. Ferdous, H. Miao, P.-H. Wang, D. E. Leaird, K. Srinivasan, L. Chen, V. Aksyuk, and A. M. Weiner, "Probing coherence in microcavity frequency combs via optical pulse shaping," Opt. Express **20**, 21033–21043 (2012).
23. X. Xue, Y. Xuan, Y. Liu, P. Wang, S. Chen, J. Wang, D. E. Leaird, M. Qi, and A. M. Weiner, "Mode interaction aided soft excitation of

dark solitons in normal dispersion microresonators and offset-frequency tunable Kerr combs," arXiv:1404.2865 (2014).
24. S.-W. Huang, J. F. McMillan, J. Yang, A. Matsko, H. Zhou, M. Yu, D.-L. Kwong, L. Maleki, and C. W. Wong, "Direct generation of 74-fs mode-locking from on-chip normal dispersion frequency combs," arXiv:1404.3256 (2014).
25. A. B. Matsko, A. A. Savchenkov, and L. Maleki, "Normal group-velocity dispersion Kerr frequency comb," Opt. Lett. **37**, 43–45 (2012).
26. A. A. Savchenkov, A. B. Matsko, W. Liang, V. S. Ilchenko, D. Seidel, and L. Maleki, "Kerr frequency comb generation in overmoded resonators," Opt. Express **20**, 27290–27298 (2012).
27. I. S. Grudinin and N. Yu, "Frequency combs from crystalline resonators: influence of cavity parameters on comb dynamics," arXiv:1406.0790v1 (2014).
28. H. A. Haus and W. Huang, "Coupled-mode theory," Proc. IEEE **79**, 1505–1518 (1991).
29. J. Wiersig, "Formation of long-lived, scarlike modes near avoided resonance crossings in optical microcavities," Phys. Rev. Lett. **97**, 253901 (2006).
30. S. Gröblacher, K. Hammerer, M. R. Vanner, and M. Aspelmeyer, "Observation of strong coupling between a micromechanical resonator and an optical cavity field," Nature **460**, 724–727 (2009).
31. T. Klaassen, J. de Jong, M. van Exter, and J. P. Woerdman, "Transverse mode coupling in an optical resonator," Opt. Lett. **30**, 1959–1961 (2005).
32. L. Novotny, "Strong coupling, energy splitting, and level crossings: a classical perspective," Am. J. Phys. **78**, 1199–1202 (2010).
33. G. Anetsberger, E. M. Weig, J. P. Kotthaus, and T. J. Kippenberg, "Cavity optomechanics and cooling nanomechanical oscillators using microresonator enhanced evanescent near-field coupling," C. R. Phys. **12**, 800–816 (2011).
34. T. Carmon, H. G. L. Schwefel, L. Yang, M. Oxborrow, A. D. Stone, and K. J. Vahala, "Static envelope patterns in composite resonances generated by level crossing in optical toroidal microcavities," Phys. Rev. Lett. **100**, 103905 (2008).
35. S. Ramelow, A. Farsi, S. Clemmen, J. S. Levy, A. R. Johnson, Y. Okawachi, M. R. E. Lamont, M. Lipson, and A. L. Gaeta, "Strong polarization mode coupling in microresonators," arXiv:1405.5211 (2014).
36. I. S. Grudinin, L. Baumgartel, and N. Yu, "Impact of cavity spectrum on span in microresonator frequency combs," Opt. Express **21**, 26929–26935 (2013).
37. T. Herr, V. Brasch, J. D. Jost, I. Mirgorodskiy, G. Lihachev, M. L. Gorodestky, and T. J. Kippenberg, "Mode spectrum and temporal soliton formation in optical microresonators," arXiv:1311.1716 (2013).
38. P. Del'Haye, O. Arcizet, M. L. Gorodetsky, R. Holzwarth, and T. J. Kippenberg, "Frequency comb assisted diode laser spectroscopy for measurement of microcavity dispersion," Nat. Photonics **3**, 529–533 (2009).
39. J. C. Tully and R. K. Preston, "Trajectory surface hopping approach to nonadiabatic molecular collisions: the reaction of H+ with D_2," J. Chem. Phys. **55**, 562–572 (1971).
40. J. C. Tully, "Molecular dynamics with electronic transitions," J. Chem. Phys. **93**, 1061–1071 (1990).
41. L. D. Landau and E. M. Lifshitz, *Quantum Mechanics: Non-Relativistic Theory*, 3rd ed. (Butterworth-Heinemann, 2003).
42. A brief report on these observations is given in Y. Liu, Y. Xuan, X. Xue, P.-H. Wang, A. J. Metcalf, S. Chen, M. Qi, and A. M. Weiner, "Investigation of mode interaction in optical microresonators for Kerr frequency comb generation," to appear in CLEO: 2014, paper FW1D.2; also see arXiv:1402.5686 (2014).
43. T. Herr, K. Hartinger, J. Riemensberger, C. Y. Wang, E. Gavartin, R. Holzwarth, M. L. Gorodetsky, and T. J. Kippenberg, "Universal formation dynamics and noise of Kerr-frequency combs in microresonators," Nat. Photonics **6**, 480–487 (2012).
44. I. S. Grudinin, L. Baumgartel, and N. Yu, "Frequency comb from a microresonator with engineered spectrum," Opt. Express **20**, 6604–6609 (2012).
45. S. B. Papp and S. A. Diddams, "Spectral and temporal characterization of a fused-quartz-microresonator optical frequency comb," Phys. Rev. A **84**, 053833 (2011).
46. S. Saha, Y. Okawachi, B. Shim, J. S. Levy, R. Salem, A. R. Johnson, M. A. Foster, M. R. E. Lamont, M. Lipson, and A. L. Gaeta, "Mode locking and femtosecond pulse generation in chip-based frequency combs," Opt. Express **21**, 1335–1343 (2013).
47. T. Herr, V. Brasch, J. D. Jost, C. Y. Wang, N. M. Kondratiev, M. L. Gorodetsky, and T. J. Kippenberg, "Temporal solitons in optical microresonators," Nat. Photonics **8**, 145–152 (2013).
48. P. Del'Haye, S. B. Papp, and S. A. Diddams, "Self-injection locking and phase-locked states in microresonator-based optical frequency combs," Phys. Rev. Lett. **112**, 043905 (2014).
49. S. Coen, H. G. Randle, T. Sylvestre, and M. Erkintalo, "Modeling of octave-spanning Kerr frequency combs using a generalized mean-field Lugiato–Lefever model," Opt. Lett. **38**, 37–39 (2013).
50. F. Leo, L. Gelens, P. Emplit, M. Haelterman, and S. Coen, "Dynamics of one-dimensional Kerr cavity solitons," Opt. Express **21**, 9180–9191 (2013).
51. M. Erkintalo and S. Coen, "Coherence properties of Kerr frequency combs," Opt. Lett. **39**, 283–286 (2014).
52. M. R. E. Lamont, Y. Okawachi, and A. L. Gaeta, "Route to stabilized ultrabroadband microresonator-based frequency combs," Opt. Lett. **38**, 3478–3481 (2013).
53. A. Matsko, A. Savchenkov, and L. Maleki, "On excitation of breather solitons in an optical microresonator," Opt. Lett. **37**, 4856–4858 (2012).
54. A. Matsko, A. Savchenkov, W. Liang, V. Ilchenko, D. Seidel, and L. Maleki, "Mode-locked Kerr frequency combs," Opt. Lett. **36**, 2845–2847 (2011).
55. I. Balakireva, A. Coillet, C. Godey, and Y. K. Chembo, "Stability analysis of the Lugiato-Lefever model for Kerr optical frequency combs. Part II: case of anomalous dispersion," arXiv:1308.2542v1 (2013).
56. P. Parra-Rivas, D. Gomila, M. A. Matias, S. Coen, and L. Gelens, "Dynamics of localized and patterned structures in the Lugiato-Lefever equation determine the stability and shape of optical frequency combs," arXiv:1401.6059v1 (2014).
57. A. Coillet, I. Balakireva, R. Henriet, K. Saleh, L. Larger, J. M. Dudley, C. R. Menyuk, and Y. K. Chembo, "Azimuthal turing patterns, bright and dark cavity solitons in Kerr combs generated with whispering-gallery-mode resonators," IEEE Photon. J. **5**, 6100409 (2013).
58. C. Godey, I. Balakireva, A. Coillet, and Y. K. Chembo, "Stability analysis of the Lugiato-Lefever model for Kerr optical frequency combs. Part I: case of normal dispersion," arXiv:1308.2539v1 (2013).
59. M. Haelterman, S. Trillo, and S. Wabnitz, "Dissipative modulation instability in a nonlinear dispersive ring cavity," Opt. Commun. **91**, 401–407 (1992).
60. S. Coen and M. Erkintalo, "Universal scaling laws of Kerr frequency combs," Opt. Lett. **38**, 1790–1792 (2013).

optica

Classical condensation of light pulses in a loss trap in a laser cavity

GILAD OREN, ALEXANDER BEKKER, AND BARUCH FISCHER*

Department of Electrical Engineering, Technion, Haifa 32000, Israel

**Corresponding author: fischer@ee.technion.ac.il*

Received 23 April 2014; revised 15 July 2014; accepted 29 July 2014 (Doc. ID 210707); published 2 September 2014

We present an experimental demonstration of condensation in a many-light-pulse system in a loss trap (loss well) in a one-dimensional laser cavity. The route to condensation is similar to Bose–Einstein condensation in a potential trap (potential well), but classical. The pulses, their loss levels, and the noise-induced power distribution take the role of "particles", "energy" levels, and quantum-thermal population-statistics, respectively. The multipulse system is formed by high harmonic active mode-locking modulation and the trap by an envelope modulation. The experiment is done with an erbium-doped fiber laser. Condensation is shown to occur when the loss trap has near the lowest-loss pulse a power law dependence with exponent smaller than 1, as the theory predicts.

OCIS codes: (140.4050) Mode-locked lasers; (270.3430) Laser theory; (020.1475) Bose-Einstein condensates; (000.6590) Statistical mechanics.

http://dx.doi.org/10.1364/OPTICA.1.000145

Bose–Einstein condensation (BEC) is a special many-boson phenomenon that was observed in atomic particles [1,2]. Recent works have shown condensation in relatively simple systems, even at room temperature, compared to the ultralow temperatures needed so far to observe BEC. They were mostly based on nonatomic particles such as photons [3], polaritons [4,5], and magnons [6]. We can also find classical condensation experiments that use light and lasers [7–13]. This was shown, for example, in a single-pulse waveform system in an actively mode-locked laser, where the light power collapses upon condensation into the lowest pulse waveform [7,8]. In a more recent work [9], we theoretically suggested that simple cw lasers show in certain conditions a classical light condensation (LC) route that is formally similar to quantum BEC [14]. This is based on weighting the modes of the laser in a loss–gain scale, compared to energy (or photon frequency) in BEC, and the noise in the laser (spontaneous emission, external, etc.) functions as temperature. The levels are the regular cavity modes of the laser, and the condensation occurs in the modes' spectral domain where, for low noise or high laser power, the light power concentrates at the lowest-loss mode. The relation of this effect to lasing and to photon-BEC [3] was discussed in [9]. Other many-body effects such as phase transitions and critical phenomena were also observed in lasers [15–19].

Our experiment is done with a unique many-body system of many pulses in a laser cavity. The "particles", their "energy" levels, and population are the pulses, their corresponding loss levels, and powers, respectively. As we discuss below, this pulse system is formally equivalent to the cw laser mode system with spectral filtering that was theoretically shown to exhibit LC [9]. In the present pulse system, however, the condensation is expected to be in the spatial (or time) domain rather than the frequency domain. This condensation prediction has not been observed yet experimentally, and the present work therefore provides a first experimental demonstration of it. It requires a loss trap (loss well) with a power law dependence having an exponent $\eta < 1$, like the potential trap (potential well) needed for atomic quantum BEC in one dimension (1D) [14]. There (and in single-pulse condensation) $\eta < 2$ due to an additional kinetic energy (or similar) term.

The many-pulse system is obtained by the N_0-th harmonic active mode locking (AML) order of a laser that generates N_0 pulses with approximately the same width and power, bouncing in the cavity with equal spacing. AML is usually obtained by RF-driven electro-optic modulation of the light in the laser at the basic or harmonic cavity frequency that can nowadays reach 40 GHz, and then generate pulse trains at such rates. In fiber lasers with lengths of $L \sim 10$–100 m, we can have with high harmonic modulations hundreds and thousands of pulses in the cavity. We can view the pulses in the time domain or in the corresponding spatial domain in the cavity when we take a snapshot of the pulses or propagate with them. We therefore

have in the cavity N_0 pulse sites given by the harmonic AML with a pulse population in terms of power. We nevertheless need hierarchy in the pulse system, like the energy in thermodynamics statistics. We therefore add to the usual AML N_0 pulse system in the cavity an envelope modulation that makes the pulses have different losses, as illustrated in Fig. 1 for $N_0 = 15$ pulses. This modulation can be viewed as a loss trap, like the potential trap in BEC [14]. It determines the density of pulse loss states that has an important role for condensation occurrence. The situation in the pulse system is similar to that of the cw laser mode case, where a loss trap in the spectral domain (spectral filtering) can produce LC [9]. Another important point here is that each pulse state is represented by a single loss value according to its location in the loss trap (as seen in Fig. 1). By doing this, we ignore the high intrapulse

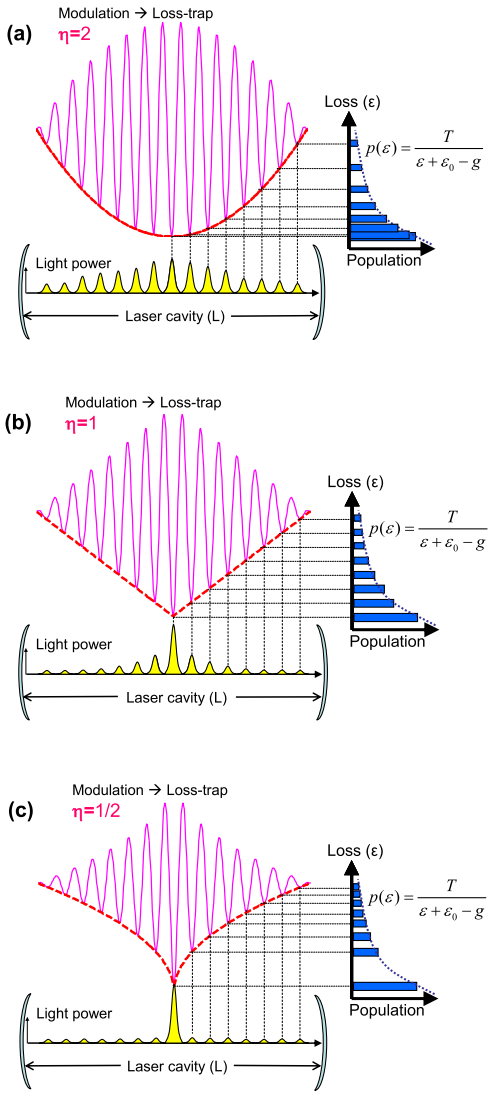

Fig. 1. Pulse system and the loss trap in the laser cavity. The loss trap is provided by an envelope modulation, shown for $\eta = 2, 1, 1/2$, and the pulses by a harmonic modulation, here illustrated for a 15th order, that gives 15 pulse sites. Characteristic pulse forms are plotted in the cavity in each figure along with their power distributions, which are shown in the diagrams to the right. We note that in the experiments, the pulses in the cavity are much denser, and so are the loss states. In the present experiment, we had 51 pulses.

loss levels and take only the lowest one in each pulse; it is allowed for pulse forms (commonly harmonic oscillator modes) with loss level spacings that are significantly larger than the interpulse loss level difference. A detailed study of this point will be given elsewhere.

We summarize the mathematical base of pulse condensation in the regime that each pulse has one loss value. We recall that the pulses are produced by high harmonic AML with an added envelope modulation that produces the loss trap and the pulse loss differentiation. We take the pulse locations in the cavity as a grid where the pulses are located with a population size measured in power terms, according to the noise-induced statistics. Therefore, the equation of motion is considered for the pulse population in the cavity without going into the formation of the pulses by high harmonic mode locking. Then the master equation for the pulse amplitudes a_m and the mathematical description are similar to the theory developed for the cw laser mode system [9]:

$$(da_m/d\tau) = (g - \varepsilon_m)a_m + \Gamma_m. \tag{1}$$

Here, a_m denotes pulse amplitude compared to mode amplitudes in the cw laser case, τ is the long-term time variable that counts cavity roundtrip frames, and g is a slow saturable-gain factor, shared by all pulses. ε_m is the mth pulse loss term, and Γ_m is an additive noise term that can result from spontaneous emission and any other internal or external source. It is modeled by a white Gaussian process with covariance $2T$: $\langle \Gamma_m(\tau)\Gamma_n^*(\tau')\rangle = 2T\delta(\tau - \tau')\delta_{mn}$ and $\langle \Gamma_m(\tau)\rangle = 0$, where $\langle\rangle$ denotes average. We emphasize that the master equation has a noise term but no explicit nonlinearity besides the one resulting from the overall power constraint.

We obtain from Eq. (1) the following expression for the overall pulse power in the cavity:

$$P = \sum_{m=-N}^{N} p_m = \sum_{m=-N}^{N} \frac{T}{\varepsilon_m - g}$$
$$\rightarrow P = \frac{T}{\varepsilon_0 - g} + T\int_0^{\varepsilon_N} \frac{\rho(\varepsilon)\mathrm{d}\varepsilon}{\varepsilon + \varepsilon_0 - g}, \tag{2}$$

where $p_m = |a_m|^2$ is the power of pulse m. For the integral with the continuous loss variable ε, measured relatively to the lowest pulse loss ε_0, we define the density of loss states (DOS) $\rho(\varepsilon)$ that has a prime role for condensation occurrence. ε_N is the highest pulse loss in the cavity, the loss trap depth. The first term at the right-hand side in the second line of Eq. (2) gives the power of the lowest-loss mode, and the second term is the power in all higher modes. We can notice the resemblance of Eq. (2) to that of the overall boson number in a potential well in BEC [14]. The weight for each spectral component depends on $\rho(\varepsilon)$ and the factor $T/(\varepsilon + \varepsilon_0 - g)$ replaces the Bose–Einstein statistics (see Table 1). The power of each pulse is $p_m = T/(\varepsilon_m - g)$, meaning that the noise populates the pulse states according to their loss in a similar way to thermal excitation via Bose–Einstein distribution.

We consider for the envelope loss function a power law dependence around the lowest-loss pulse, $\varepsilon_m = \varepsilon_0 + \varepsilon_N|(m/N)|^\eta$,

Table 1. Analogy between BEC and Pulse/Mode Condensation

Quantum BEC in a Potential Trap [14]	Classical Pulse/Mode Condensation in a Loss Trap
Many noninteracting bosons	Many noninteracting pulses/modes in a laser cavity
Energy scale: ε, $\hbar\nu$	Loss scale: ε
Temperature: T	Optical noise: T
Bose–Einstein thermal statistics:	Noise-induced pulse/mode power distribution:
$f_{\mathrm{BE}}(\varepsilon) = 1/\{\exp[(\varepsilon-\mu)/k_BT]-1\} \underset{[(\varepsilon-\mu)/k_BT]\ll 1}{\rightarrow} k_BT/(\varepsilon-\mu)$	$p(\varepsilon) = T/(\varepsilon+\varepsilon_0-g)$
Chemical potential: μ	Lowest pulse loss ("chemical-potential"): $\mu \equiv g-\varepsilon_0$
Overall particle number constraint:	Overall power constraint:
$N = n_0 + \int_0^\infty \frac{\rho(\varepsilon)\mathrm{d}\varepsilon}{\exp[(\varepsilon-\mu)/k_BT]-1}$	$P = p_0 + T\int_0^{\varepsilon_N} \frac{\rho(\varepsilon)\mathrm{d}\varepsilon}{\varepsilon+\varepsilon_0-g}$
n_0 is the ground-state ($\varepsilon = 0$) population.	p_0 is the lowest-loss ($\varepsilon = 0$) pulse/mode power.
Energy DOS in 1D potential trap [14]: $\rho(\varepsilon) \propto \varepsilon^{(1/\eta)-(1/2)}$	Pulse/mode DOS in 1D loss trap [9]: $\rho(\varepsilon) \propto \varepsilon^{(1/\eta)-1}$
DOS for d-dimensional potential trap [14]: $\rho(\varepsilon) \propto \varepsilon^{(d/\eta)+(d/2)-1}$	Single-pulse AML DOS in 1D loss trap [7,8]: $\rho(\varepsilon) \propto \varepsilon^{(1/\eta)-(1/2)}$
Condition for condensation in 1D potential trap [14]: $\eta < 2$	Condition for pulse/mode condensation in 1D loss trap [9]: $\eta < 1$
	Condensation condition for single-pulse AML in 1D [7,8]: $\eta < 2$

where we have $N_0 = 2N+1$ pulses in the cavity. It can be expressed in a continuous variable form $\varepsilon = \varepsilon_N(|t|/t_R)^\eta = \varepsilon_N(|z|/L)^\eta$ in terms of the cavity time t/t_R or space z/L variables. $L = ct_R$ and t_R are the roundtrip cavity length and time, and c is the speed of light. Loss traps with various exponents η are shown in Fig. 1. The corresponding DOS, derived as in [9], is given by $\rho(\varepsilon) = [2N/(\eta\varepsilon_N^{1/\eta})]\varepsilon^{(1/\eta)-1}$.

As the noise T is lowered (or P is raised) the distribution $p(\varepsilon)$ yields a gradual concentration of the pulse power at lower-loss states. Nevertheless, when condensation takes place, p_0 gets a macroscopic part of the power. It occurs when the integral in Eq. (2) converges at $\varepsilon = 0$ ($t = z = 0$), which happens when $\eta < 1$. Then, the power population of the light at higher than $\varepsilon = 0$ levels stays unchanged (filled) at $P_c = T\int_0^{\varepsilon_N}\rho(\varepsilon)\mathrm{d}\varepsilon/\varepsilon$, and additional pumping that increases P beyond P_c (or lowering T below T_c) will cause population of the lowest-level power p_0, which starts to grow macroscopically. At condensation ($P \geq P_c$ or $T \leq T_c$), the net gain for the lowest-loss pulse (the "chemical potential") becomes $\mu \equiv g-\varepsilon_0 = 0$. (It is negative at the noncondensate regime.) We therefore have a many-pulse system with a condensation route that is mathematically similar to BEC, but classical. As in BEC, there is no direct pulse ("particle") interaction, but a global constraint on the overall pulse power ("particle number"). Nevertheless, the "energy" hierarchy is in a loss–gain scale, where the "ground state" is the lowest-loss pulse and the noise has the role of temperature.

Our experiment is done in a ring erbium-doped fiber laser described in Fig. 2, with a 51st order harmonic AML that gives 51 pulses equally spaced in the cavity and has about the same power before applying the envelope modulation. We injected into the cavity controllable optical noise T using amplified spontaneous emission from an erbium-doped fiber amplifier.

Figure 3 gives the experimental and theoretical condensation ratio p_0/P dependence on the noise level T for several exponents. The condensation transition becomes sharper when the pulse number increases, as is the case in many-body systems. T measures the injected noise, but in the experiment there is the additional internal laser noise that limits the lowest achievable overall T and therefore the maximum condensation ratio. In the theoretical analysis, we added a constant internal noise that fitted the experimental graphs (which is negligible at the condensation region, but becomes significant at low T) that caused a partial condensation ratio and its saturation, as seen in this figure and in Fig. 4. We also note that the plots are against T/P (with an arbitrary shift) since variation of the injected noise in the experiment changed P, although the laser pumping was kept unchanged.

Figure 4 shows measurements of the power distributions among the 51 pulses in the cavity, as a function of the injected noise level T, for various exponents. In all of them, the distribution becomes more centered at lower-loss pulse states when the noise is lowered, as expected in noise-induced (or thermal) excitation. However, for $\eta < 1$ and partially for $\eta = 1$, there is a pronounced transition of the power into

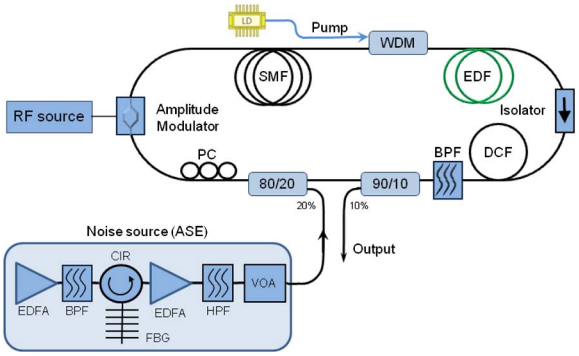

Fig. 2. Experimental setup. Ring fiber laser of length L ≈ 404 m, with a high harmonic AML, an envelope modulation (509 kHz), and a controllable noise injection. The wavelength was ~1549 nm. The system is composed of an erbium-doped fiber amplifier (EDFA), single mode fiber (SMF), wavelength division multiplexer (WDM), dispersion compensation fiber (DCF), bandpass filter (BPF), high pass filter (HPF), variable optical attenuator (VOA), polarization controller (PC), circulator (CIR), and fiber Bragg grating (FBG).

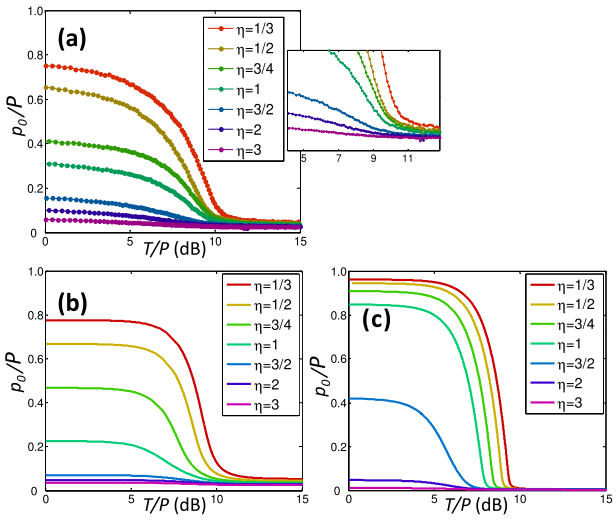

Fig. 3. Experimental and theoretical lowest-loss pulse power versus noise level normalized by power (T/P) for various η s. (a) Experimental results for 51 pulses in the cavity. The inset is a zoomed view of the transition region and the difference between the two regimes, below and above $\eta = 1$. Theoretical graphs are shown for (b) 51 and (c) 501 pulses.

the lowest-loss pulse state. The experimental results in Figs. 3 and 4 follow and verify the theoretical prediction [9] showing condensation for $\eta < 1$. We note in the caption of Fig. 3 that T measures the injected and not the internal noise,

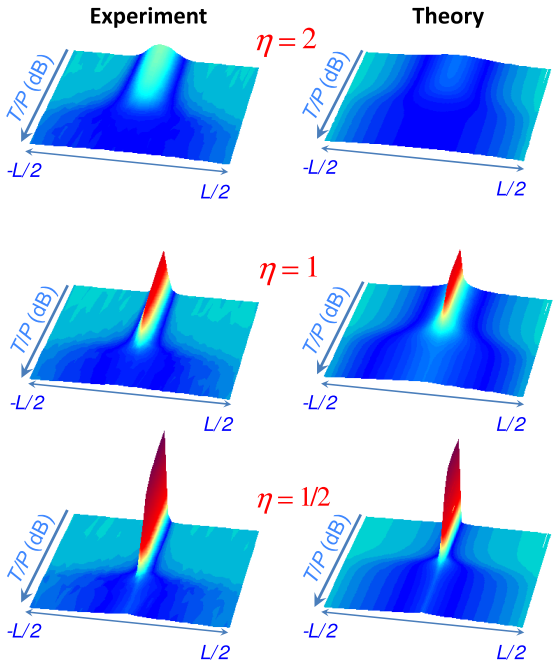

Fig. 4. Experimental and theoretical pulse power distribution. The experimental figures (left-hand side figures) are plotted from measurements of 51 equally spaced pulses in the cavity frame $(-L/2, L/2)$, as a function of the injected noise level T (in logarithmic scale and opposite direction), for various η s. The corresponding theoretical results are shown in the right-hand side figures. We can see the route to condensation for $\eta < 1$ with a massive lowest-loss pulse population as T decreases. The power scale is the same as in Fig. 3.

and therefore the figures show partial condensation ratios and saturation. A detailed account on those sides will be included in a full-length work. We also note that in our experiment we had only 51 pulses in the cavity, and therefore the phase-transition point is less sharp and the higher-loss pulse powers are not close to zero as one would obtain in the thermodynamic limit for large particle number, as can be seen in Fig. 3(c), which was calculated for 501 pulses. A larger number of pulses in the cavity would be experimentally feasible, but it raised other disturbances in the present experiment.

We have experimentally demonstrated and verified the prediction of a classical condensation phenomenon with a pulse system in a 1D laser cavity in a loss trap. The route to condensation is similar to cw laser LC and formally similar to quantum BEC in a potential trap [14]. We have experimentally shown that condensation occurs for loss trap exponents $\eta < 1$ like in the BEC case. The experiment is done with a fiber laser that produces pulses upon high harmonic AML, and the loss trap is achieved by an envelope modulation. It is a remarkably simple experimental system that nevertheless provides a first demonstration of LC in a new many-pulse system in a loss trap in a laser cavity. It can also serve as an experimental base for a further study on condensation that includes, for example, nonlinearity and pulse interaction.

FUNDING INFORMATION

Israel Science Foundation (ISF); Binational US-Israel Science Foundation (BSF).

REFERENCES

1. M. H. Anderson, J. R. Ensher, M. R. Matthews, C. E. Weiman, and E. A. Cornell, Science **269**, 198 (1995).
2. A. J. Leggett, Rev. Mod. Phys. **73**, 307 (2001).
3. J. Klaers, J. Schmitt, F. Vewinger, and M. Weitz, Nature **468**, 545 (2010).
4. R. Balili, V. Hartwell, D. Snoke, L. Pfeiffer, and K. West, Science **316**, 1007 (2007).
5. H. Deng, G. Weihs, C. Santori, J. Bloch, and Y. Yamamoto, Science **298**, 199 (2002).
6. S. O. Demokritov, V. E. Demidov, O. Dzyapko, G. A. Melkov, A. A. Segre, B. Hillerbrands, and A. N. Slavin, Nature **443**, 430 (2006).
7. R. Weill, B. Fischer, and O. Gat, Phys. Rev. Lett. **104**, 173901 (2010).
8. R. Weill, B. Levit, A. Bekker, O. Gat, and B. Fischer, Opt. Express **18**, 16520 (2010).
9. B. Fischer and R. Weill, Opt. Express **20**, 26704 (2012).
10. C. Sun, S. Jia, C. Barsi, S. Rica, A. Picozzi, and J. W. Fleischer, Nat. Phys. **8**, 470 (2012).
11. C. Connaughton, C. Josserand, A. Picozzi, Y. Pomeau, and S. Rica, Phys. Rev. Lett. **95**, 263901 (2005).
12. C. Conti, M. Leonetti, A. Fratalocchi, L. Angelani, and G. Ruocco, Phys. Rev. Lett. **101**, 143901 (2008).
13. A. Fratalocchi, Nat. Photonics **4**, 502 (2010).
14. V. Bagnato and D. Kleppner, Phys. Rev. A **44**, 7439 (1991).
15. A. Gordon and B. Fischer, Phys. Rev. Lett. **89**, 103901 (2002).
16. B. Vodonos, R. Weill, A. Gordon, A. Bekker, V. Smulakovsky, O. Gat, and B. Fischer, Phys. Rev. Lett. **93**, 0153901 (2004).
17. A. Rosen, R. Weill, B. Levit, V. Smulakovsky, A. Bekker, and B. Fischer, Phys. Rev. Lett. **105**, 013905 (2010).
18. A. Schwartz and B. Fischer, Opt. Express **21**, 6196 (2013).
19. B. Fischer and A. Bekker, Opt. Photon. News **24**, 40 (2013).

optica

Integrated nanophotonics based on nanowire plasmons and atomically thin material

KENNETH M. GOODFELLOW,[1] RYAN BEAMS,[1] CHITRALEEMA CHAKRABORTY,[2] LUKAS NOVOTNY,[3] AND A. N. VAMIVAKAS[1,4,*]

[1]Institute of Optics, University of Rochester, Rochester, New York 14627, USA

[2]Materials Science, University of Rochester, Rochester, New York 14627, USA

[3]Photonics Laboratory, ETH Zürich, 8093 Zürich, Switzerland

[4]Center for Coherence and Quantum Optics, University of Rochester, Rochester, New York 14627, USA

*Corresponding author: nick.vamivakas@rochester.edu

Received 13 June 2014; revised 16 July 2014; accepted 17 July 2014 (Doc. ID 213880); published 4 September 2014

The continually increasing demands for higher-speed and lower-operating-power devices have resulted in the continued impetus to shrink photonic components. We demonstrate a primitive nanophotonic integrated circuit element composed of a single silver nanowire and single-layer molybdenum disulfide (MoS_2) flake. Using scanning confocal fluorescence microscopy and spectroscopy, we find that nanowire plasmons can excite MoS_2 photoluminescence and that MoS_2 excitons can decay into nanowire plasmons. Finally, we show that the nanowire may serve the dual purpose of both exciting MoS_2 photoluminescence via plasmons and recollecting the decaying exciton as nanowire plasmons. The potential for subwavelength light guiding and strong nanoscale light–matter interaction afforded by our device may facilitate compact and efficient on-chip optical processing.

OCIS codes: (160.6000) Semiconductor materials; (250.5403) Plasmonics; (350.4238) Nanophotonics and photonic crystals.

http://dx.doi.org/10.1364/OPTICA.1.000149

Novel nanophotonic devices and nanomaterials are being explored for their potential in next-generation on-chip optical processing [1,2]. Surface plasmon polaritons (SPPs) [3], electromagnetic excitations that propagate along the interface between a metal and a dielectric, are a natural candidate for both integrated subwavelength light guiding and pronounced light–matter coupling [4–6]. Silver (Ag) nanowires have been studied extensively in this regard [7–11], and coupling has been demonstrated between Ag nanowires and other nanostructures, such as quantum dots [12–14] and nitrogen-vacancy centers [15,16].

Although there has been some investigation into graphene nanowire hybrids for nanophotonic circuitry [17,18], the vast potential for two-dimensional atomically thin materials in this realm is largely unexplored. Single-layer molybdenum disulfide (MoS_2) [19], a semiconductor being explored for its photoluminescence [20] potential as both a transistor [21] and photodetector [22,23], is an ideal choice to couple with nanoplasmonic circuitry. In this Letter, we explore the nanophotonics of a MoS_2/Ag nanowire hybrid structure. We demonstrate coupling between a single-layer MoS_2 flake and a single Ag nanowire. We show that a plasmon excited at the uncovered end of the nanowire can propagate and excite MoS_2 photoluminescence (PL), both by direct plasmon-to-exciton conversion along the wire and by absorbing photons rescattering from the end of the wire. We also demonstrate that MoS_2 excitons can decay to generate Ag nanowire plasmons. Finally, we show it is possible for the Ag nanowire to serve a dual role as both a channel for MoS_2 excitation and subsequent extraction of the decaying MoS_2 excitons.

Figure 1(a) presents an illustration of the fabricated MoS_2/Ag nanowire device. An incident photon is converted to a plasmon that propagates along the wire. When the plasmon arrives at the MoS_2, the plasmon may either be converted to an exciton, resulting in frequency-shifted photon emission from the MoS_2, or it can be converted back to a photon at the end of the wire. An optical micrograph of the hybrid device studied in this Letter is shown in Fig. 1(b). Figure 1(c) is a Raman spectrum acquired at the overlap region between the end of the nanowire and the MoS_2. The measured Raman spectrum reveals that the flake is single-layer MoS_2 [24].

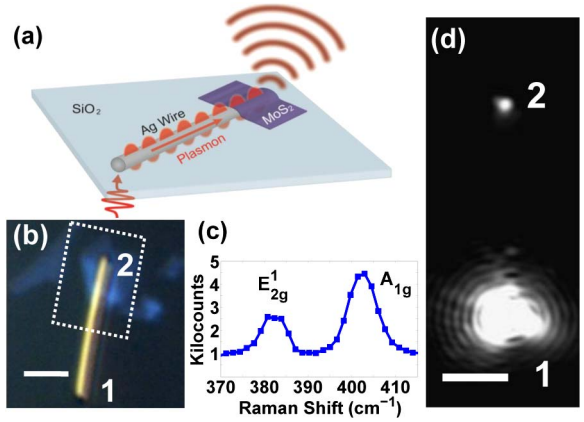

Fig. 1. (a) Schematic of MoS_2/nanowire structure. (b) Single-layer MoS_2 on a silver nanowire on glass after transfer of the flake. (c) Raman spectrum collected at the end of the wire in MoS_2; $\lambda = 532$ nm, power = 70 μW. (d) Demonstration of plasmon propagation along the Ag nanowire; $\lambda = 635$ nm, power = 20 μW. All scale bars are 2 μm.

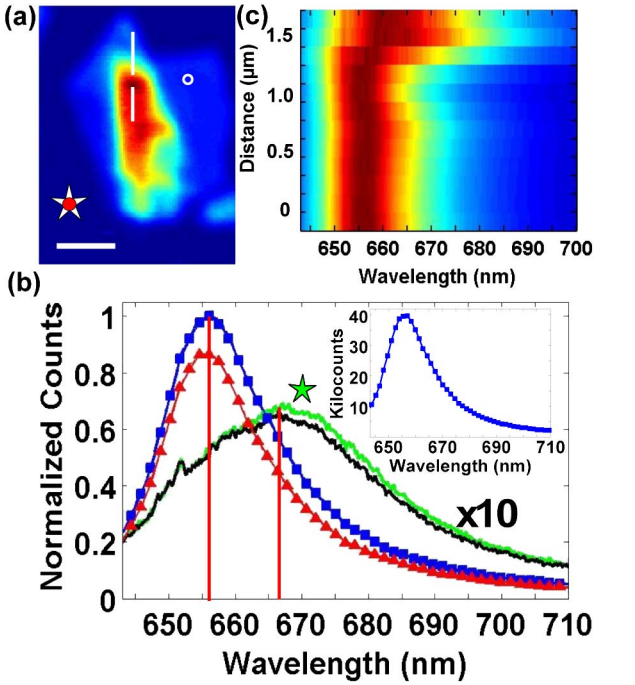

Fig. 2. (a) Confocal fluorescence image of the MoS_2/wire device from the dotted white box in Fig. 1(b). The red dot and white star represent no displacement between the excitation and collection focal volume, respectively. Scale bar is 1 μm. (b) Normalized photoluminescence spectra for the end of the wire covered by MoS_2 excited with light polarized parallel (blue decorated with squares) and perpendicular (red decorated with triangles) to the wire. Spectra of the MoS_2 on substrate were also acquired using parallel (green with star above) and perpendicular (black) excitation polarizations. The spectra for the MoS_2 on substrate are rescaled for clarity. Inset: absolute photoluminescence counts for the end of the wire in MoS_2 with light polarized parallel to the wire. (c) Spectra taken in 150 nm steps along the line in (a). For all images, $\lambda = 633$ nm, power = 5 μW.

To fabricate the device, we used a PMMA liftoff technique [25] to transfer the MoS_2 from a silicon with thermal oxide substrate to the wire on a standard glass cover slip. See Supplement 1 for more details on device fabrication.

The charge-coupled device (CCD) image in Fig. 1(d) demonstrates plasmon propagation and photon re-emission. Laser radiation ($\lambda = 635$ nm), polarized parallel to the wire axis, is coupled from the far-field into the nanowire at the end labeled "1" in Fig. 1(b) using a 100× oil-immersion objective with numerical aperture (NA) of 1.3. To reduce scattering and eliminate leakage radiation, the sample was covered in index-matching ($n = 1.515$) oil. In order to convert a photon into an SPP, the laser must be focused onto one of the ends of the wire; this accounts for the momentum mismatch between the incoming photon and the plasmon [9]. The SPP $1/e$ propagation length increases for larger-diameter wires [26] and longer excitation wavelengths [4]. The wires used in our study (average diameter 386 nm) support two lower-order modes, $m = 0$ and $m = 1$, which couple to incident light polarized parallel and perpendicular to the wire, respectively [11]. The in-coupling efficiency is always greater for the $m = 0$ mode than for the $m = 1$ mode, but the $1/e$ propagation length of the $m = 1$ mode becomes longer for larger diameter wires. For a wire of this length, following parallel excitation, we calculate the efficiency of photon re-emission at the end of the wire after plasmon propagation to be around 0.008%–0.012%. See Supplement 1 for a discussion of photon re-emission efficiencies.

Coupling between far-field photons, SPPs, and the single-layer MoS_2 was studied using an inverted confocal microscope utilizing an oil-immersion objective (NA = 1.4). A nanopositioning stage (Mad City Labs, Inc.) was used to scan and position the sample. Excitation polarization was controlled by a half-wave plate. The signal from the sample was sent to either an APD or a spectrometer. Longpass filters to block the laser line were used in front of both detectors. A fluorescence image of the single-layer flake on the wire from Fig. 1(b) using a laser ($\lambda = 633$ nm) is shown in Fig. 2(a). For photon-counting images, we adopt the convention of using a solid red circle to indicate the excitation and a white star to represent the approximate center of the collection focal volume, respectively. For this data set, the excitation and collection focal volumes are coincident so the dot and star overlap, indicating no displacement between excitation and collection. In Fig. 2(a), we observe strong PL from the MoS_2 flake, characteristic of single-layer, as well as a large increase in counts in the area where the flake overlaps with the wire.

To investigate the origin of the increased counts, Fig. 2(b) presents spectra acquired with the excitation polarization parallel and perpendicular to the wire on the bare flake [location indicated by the white circle in Fig. 2(a)] and at the end of the wire covered by MoS_2 [location indicated by the break in the solid vertical line in Fig. 2(a)]. Spectra taken at the end of the wire covered by MoS_2 (bare flake) with excitation polarized parallel to the wire are shown in blue (green), and the red (black) curve shows the perpendicular polarization case. By summing the recorded photo counts for all detected wavelengths when the excitation polarization is parallel (I_{par}) and perpendicular (I_{perp}) to the wire axis, we calculate an on-wire contrast $(I_{par} - I_{perp})/(I_{par} + I_{perp})$ of 9.5% and an off-wire

contrast of 2.6%. We attribute this difference to two effects. First, by removing direct contact with the substrate, MoS_2 fluorescence is known to increase [19,27]. Second, the enhancement of the MoS_2 fluorescence when the excitation is polarized parallel to the nanowire is a manifestation of an antenna-like enhancement of the excitation field (the wire influences emission the same way for the two different excitation conditions). Comparing the counts from the flake/wire region to the bare flake, we observed an enhancement of about 6.4× in fluorescence. We would expect an enhancement of about 3–5× due to removal of direct contact with the substrate [27], so the enhancement due to antenna effects is approximately 1.3–2.1× . The enhancement in MoS_2 fluorescence in the vicinity of the region where the Ag nanowire end overlaps with the MoS_2 flake is consistent on all devices we have fabricated, and we have observed a device exhibiting a 40-fold enhancement in fluorescence. See Supplement 1 for data on this device.

In addition to the enhancement, there is a clear spectral shift in the peak of the PL for the MoS_2 over the wire (656 nm) compared to on the substrate (668 nm). We attribute this shift to the MoS_2 flake not being in direct contact with the Ag nanowire as a result of the transfer process. The main PL peak of single-layer MoS_2 consists of two peaks: the A peak centered at 655 nm attributed to uncharged excitons and the A^- peak centered around 670 nm due to negatively charged trions [28]. It has been reported that interaction of the MoS_2 with the substrate suppresses exciton emission due to doping [27]. When removed from the substrate, the A peak becomes dominant. This shift is not due to strain, as strain would redshift the spectra [29]. For comparison, Fig. 2(c) presents MoS_2 spectra as we measure along the line in Fig. 2(a), starting from the bottom. Each spectrum is independently normalized. The spectral position of the peak is consistent along the wire covered by the MoS_2, and as the collection region moves off the wire, the peak redshifts.

To explore plasmon excitation of MoS_2 PL, the collection and excitation focal volumes are displaced vertically by the length of the wire. Figure 3(a) shows the resulting fluorescence image (with a CCD image of the structure overlaid) when the sample is scanned in this configuration. The prominent feature in the fluorescence image results when the laser excites plasmons at the end of the wire opposite the MoS_2, which propagate along the wire and excite MoS_2 PL. Figures 3(b) and 3(c) display a scan of this feature when light is polarized parallel and perpendicular to the wire, respectively. There is a reduction in intensity when the light is polarized perpendicular to the wire. Figure 3(d) shows the normalized polarization dependence of the signal with a contrast of 21%. This observed modulation indicates that the coupling is stronger when the excitation is parallel to the wire axis. This contrast is also greater than when the excitation was not displaced, suggesting that this feature is the result of plasmon propagation and MoS_2 excitation. The largest contrast that we observed of all of the devices tested was 80%. See Supplement 1 for data on this device. Simulations using the finite-difference time-domain (FDTD) method in Lumerical to further investigate the plasmon excitation are shown in Supplement 1.

We anticipate that plasmon-excited MoS_2 PL is not limited to the end of the wire. To investigate this, the displacement

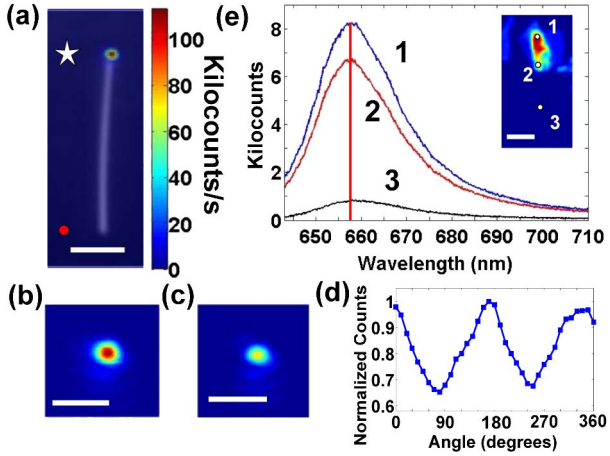

Fig. 3. (a) Fluorescence image resulting from displacing the collection and excitation focal volumes by the length of the wire, overlaid with a CCD image of the device. Scale bar is 2 μm. (b) and (c) Feature in (a) when light is polarized parallel and perpendicular to the wire, respectively. Scale bar in each is 1 μm. (d) Normalized polarization contrast of the MoS_2 fluorescence as a function of excitation polarization angle with respect to the nanowire axis; 0° corresponds to polarization parallel to the wire. (e) Spectra taken at the positions marked in the inset when the laser excitation is at the uncovered end of the wire. Scale bar is 2 μm. For all images, $\lambda = 633$ nm, power = 5 μW.

between the laser excitation and collection is adjusted to be a fraction of the wire length. The sample is then translated so that the laser excitation is at the uncovered end of the wire. Figure 3(e) presents the spectra corresponding to several points starting from the top circle, labeled "1," and walking downward in the fluorescence scan of the full sample in the inset. We observe that the PL is strongest near the end of the wire. However, we also obtain significant signal over the entire length that the wire is covered by the MoS_2. This is the result of two mechanisms at play. First, plasmons that propagate to the end of the wire are rescattered as photons and reabsorbed by the MoS_2, exciting an exciton. The electron-hole recombination then produces the PL signal. Second, plasmons in the wire are directly converted to excitons in the MoS_2, which then fluoresces.

In addition to plasmons exciting the MoS_2, excitons in the MoS_2 can be converted to plasmons that propagate along the wire and are rescattered as photons. The excitation is aligned with the overlap region of the MoS_2 flake/nanowire end, and the collection focal volume is aligned to the uncovered nanowire end (the reverse configuration of Fig. 3). Figure 4(a) shows the resulting fluorescence image with a CCD image overlaid when the sample is scanned in this configuration. Compared to the localized feature in Fig. 3(a), the present image shows an attribute that extends beyond the end of the wire. This is suggestive of plasmonic excitation along the MoS_2/wire interface. As the laser excitation scans over the MoS_2/wire interface, photons that re-emerge from the uncovered end are still detected by the confocal volume of the APD. If plasmons could only be excited at the end of the wire, the attribute in this image would look similar to the feature in Fig. 3(a). The upper (lower) inset displays a scan of the feature when the excitation light is polarized parallel (perpendicular)

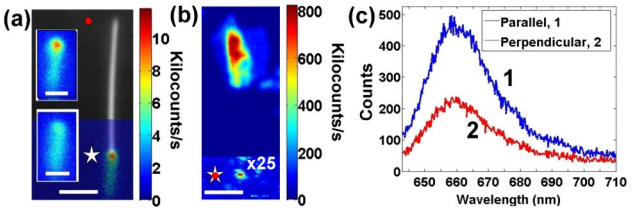

Fig. 4. (a) Image resulting from displacing the collection and excitation focal volumes by the length of the wire, overlaid with an image of the device. Opposed to Fig. 3, in this case the excitation is located at the MoS_2 end, and the collection is at the uncovered wire end. Scale bar is 2 μm. Top (bottom) inset: feature when light is polarized parallel (perpendicular) to the wire. Scale bar in each is 1 μm; $\lambda = 635$ nm, power = 20 μW. (b) Confocal fluorescence image of the sample with the uncovered end of the wire rescaled. Scale bar is 2 μm. (c) Spectra collected at the rescaled feature in (b) for light polarized parallel (blue) and perpendicular (red) to the wire. For (b) and (c), $\lambda = 633$ nm, power = 5 μW.

to the wire. Evident from comparing the two insets is an increase in the emission from the uncovered end when the excitation is parallel to the nanowire. The enhancement again suggests the nanowire provides an antenna-like enhancement of the excitation. Because MoS_2 absorption does not prefer a linear polarization, any mismatch results from excitation effects.

Finally, we demonstrate it is possible to use the Ag nanowire both as a channel for near-field excitation of the MoS_2 flake and to recollect the resultant MoS_2 fluorescence. The re-excited plasmons, at the MoS_2 photon energy, can propagate back along the wire and rescatter to the far-field as photons. Figure 4(b) shows a fluorescence image of the entire sample with the excitation and collection aligned. For this image, we have rescaled the end of the wire not covered by the MoS_2. There is a pronounced feature at the excitation end of the wire that is stronger than the background. To investigate this feature, spectra were collected for light polarized parallel and perpendicular to the wire [Fig. 4(c)]. The spectra reveal this is indeed PL from the MoS_2 flake. The pronounced polarization contrast in the two different excitation directions suggests that the Ag nanowire plasmons mediate this excitation and collection process.

In summary, we have demonstrated photonic and plasmonic interactions between an individual Ag nanowire and single-layer MoS_2. We found it is possible to excite MoS_2 with Ag nanowire plasmons as well as convert decaying MoS_2 excitons into Ag wire plasmons. This first step shows that there is pronounced nanoscale light–matter interaction between plasmons and atomically thin material that can be exploited for nanophotonic integrated circuits. A natural next step is the creation of a near-field detector based on MoS_2, as well as MoS_2 light-emitting diodes coupled to on-chip nanoplasmonic circuitry.

FUNDING INFORMATION

Directorate for Mathematical and Physical Sciences (MPS) (DMR-1309734); Office of Science, U.S. Department of Energy (DE-FG02-05ER46207); NSF IGERT (DGE-0966089); Institute of Optics.

See Supplement 1 for supporting content.

REFERENCES

1. V. J. Sorger, R. F. Oulton, R.-M. Ma, and X. Zhang, MRS Bull. **37**, 728 (2012).
2. K. C. Y. Huang, M.-K. Seo, T. Sarmiento, Y. Huo, J. S. Harris, and M. L. Brongersma, Nat. Photonics **8**, 244 (2014).
3. L. Novotny and B. Hecht, *Principles of Nano-Optics* (Cambridge University, 2006).
4. W. L. Barnes, A. Dereux, and T. W. Ebbeseni, Nature **424**, 824 (2003).
5. E. Ozbay, Science **311**, 189 (2006).
6. R. Beams, D. Smith, T. W. Johnson, S.-H. Oh, L. Novotny, and A. N. Vamivakas, Nano Lett. **13**, 3807 (2013).
7. H. Ditlbacher, A. Hohenau, D. Wagner, U. Kreibig, M. Rogers, F. Hofer, F. R. Aussenegg, and J. R. Krenn, Phys. Rev. Lett. **95**, 257403 (2005).
8. A. Manjavacas and F. J. Garcia de Abajo, Nano Lett. **9**, 1285 (2009).
9. A. W. Sanders, D. A. Routenberg, B. J. Wiley, Y. Xia, E. R. Dufresne, and M. A. Reed, Nano Lett. **6**, 1822 (2006).
10. W. Wang, Q. Yang, F. Fan, H. Xu, and Z. L. Wang, Nano Lett. **11**, 1603 (2011).
11. Z. Li, K. Bao, Y. Fang, Y. Huang, P. Nordlander, and H. Xu, Nano Lett. **10**, 1831 (2010).
12. Y. Fedutik, V. V. Temnov, O. Schöps, U. Woggon, and M. V. Artemyev, Phys. Rev. Lett. **99**, 136802 (2007).
13. A. V. Akimov, A. Mukherjee, C. L. Yu, D. E. Chang, A. S. Zibrov, P. R. Hemmer, H. Park, and M. D. Lukin, Nature **450**, 402 (2007).
14. H. Wei, D. Ratchford, X. Li, H. Xu, and C.-K. Shih, Nano Lett. **9**, 4168 (2009).
15. A. Huck, S. Kumar, A. Shakoor, and U. L. Andersen, Phys. Rev. Lett. **106**, 096801 (2011).
16. R. Kolesov, B. Grotz, G. Balasubramanian, R. J. Stöhr, A. A. L. Nicolet, P. R. Hemmer, F. Jelezko, and J. Wrachtrup, Nat. Phys. **5**, 470 (2009).
17. J. Kim, H. Son, D. J. Cho, B. Geng, W. Regan, S. Shi, K. Kim, A. Zettl, Y.-R. Shen, and F. Wang, Nano Lett. **12**, 5598 (2012).
18. H. Qian, Y. Ma, Q. Yang, B. Chen, Y. Liu, X. Guo, S. Lin, J. Ruan, X. Liu, L. Tong, and Z. L. Wang, ACS Nano **8**, 2584 (2014).
19. K. F. Mak, C. Lee, J. Hone, J. Shan, and T. F. Heinz, Phys. Rev. Lett. **105**, 136805 (2010).
20. A. Splendiani, L. Sun, Y. Zhang, T. Li, J. Kim, C.-Y. Chim, G. Galli, and F. Wang, Nano Lett. **10**, 1271 (2010).
21. B. Radisavljevic, A. Radenovic, J. Brivio, V. Giacometti, and A. Kis, Nat. Nanotechnol. **6**, 147 (2011).
22. Z. Yin, H. Li, H. Li, L. Jiang, Y. Shi, Y. Sun, G. Lu, Q. Zhang, X. Chen, and H. Zhang, ACS Nano **6**, 74 (2012).
23. O. Lopez-Sanchez, D. Lembke, M. Kayci, A. Radenovic, and A. Kis, Nat. Nanotechnol. **8**, 497 (2013).
24. C. Lee, H. Yan, L. E. Brus, T. F. Heinz, J. Hone, and S. Ryu, ACS Nano **4**, 2695 (2010).
25. A. Reina, H. Son, L. Jiao, B. Fan, M. S. Dresselhaus, Z. Liu, and J. Kong, J. Phys. Chem. C **112**, 17741 (2008).
26. J. Takahara, S. Yamagishi, H. Taki, A. Morimoto, and T. Kobayashi, Opt. Lett. **22**, 475 (1997).
27. N. Scheuschner, O. Ochedowski, A.-M. Kaulitz, R. Gillen, M. Schleberger, and J. Maultzsch, Phys. Rev. B **89**, 125406 (2014).
28. K. Mak, K. He, C. Lee, G. H. Lee, J. Hone, T. F. Heinz, and J. Shan, Nat. Mater. **12**, 207 (2013).
29. H. J. Conley, B. Wang, J. I. Ziegler, R. F. Haglund, S. T. Pantelides, and K. I. Bolotin, Nano Lett. **13**, 3626 (2013).

optica

Integrated waveguide coupled Si_3N_4 resonators in the ultrahigh-Q regime

Daryl T. Spencer,[1,*] Jared F. Bauters,[2] Martijn J. R. Heck,[3] and John E. Bowers[1]

[1]Department of Electrical and Computer Engineering, University of California, Santa Barbara, California 93106, USA

[2]Aurrion, Inc., Goleta, California 93117, USA

[3]Department of Engineering, Aarhus University, Denmark

*Corresponding author: darylt@ece.ucsb.edu

Received 24 April 2014; revised 29 July 2014; accepted 3 August 2014 (Doc. ID 210465); published 8 September 2014

The vast majority of work on waveguide-coupled resonators focuses on decreasing losses in the waveguide and coupling region. Here we present fully integrated resonators based on an ultralow-loss Si_3N_4 waveguide platform. By tailoring the directional coupler excitation to the resonators, we are able to achieve lower loss single-mode coupling to multimode waveguide widths compared to straight bus waveguide directional couplers. This allows us to demonstrate record-high integrated waveguide coupled intrinsic quality factor (Q_{int}) values of 81 million at a 9.65 mm bend radius, with a future direction to both stronger and lower loss waveguide–resonator coupling. This result opens up integration possibilities for narrow linewidth integrated diode lasers, low noise feedback systems, microwave photonic research, and the ultrastable timing reference community.

OCIS codes: (140.4780) Optical resonators; (130.0130) Integrated optics; (230.7390) Waveguides, planar; (130.7408) Wavelength filtering devices.

http://dx.doi.org/10.1364/OPTICA.1.000153

The availability of fully integrable high-Q resonators, with quality factors approaching 100 million, can create a paradigm shift for the application of photonic integrated circuits (PICs) in a wide variety of applications. A monolithically integrated resonator and coupler allows for lithographic definition and control of the system, and integration with other optical devices that can greatly benefit from such narrowband filters and frequency references in the linear operation regime [1].

In the field of microwave photonics, these high-Q resonators can act as filters with a large tuning range over tens of gigahertz bandwidth. With bandpass widths of a few megahertz, such filters outperform best-in-class YIG-based microwave filters [2]. Such high-Q elements enable oscillators with lower-noise performance than oven-controlled crystal-based oscillators (OCXOs) in the microwave frequency range. Target applications include 60 GHz wireless systems where these oscillators can increase the spectral efficiency over systems based on CMOS technology, by enabling complex modulation formats, or increase the link distance by improving the signal-to-noise ratio [3]. This added energy efficiency is essential for ubiquitous implementation of future 4G and 5G wireless systems. In coherent Doppler radars, e.g., automotive, the probability of detection of, especially, small and slow-moving targets will be increased. This increase in probability can be up to 40% for 5 dB decrease in noise [4]. In the optical domain, such oscillators can be used to create combs of optical frequencies, with very accurate spacings. These combs can act as optical "rulers" for precision spectroscopy in fields such as high-resolution metrology and gas sensing, with applications to lidar and satellite positioning systems [5]. PIC-based gyroscopes based on such high-Q resonators will outperform MEMS-based gyros and become competitive with fiber-optic and ring-laser-based approaches for tactical grade gyro applications requiring resolutions of 0.1°/h [6,7].

Generally, waveguide platforms have achieved low loss using Si [8], InP [6], doped silica [9,10], or Si_3N_4 [11–16]. In Fig. 1, we show the state of the art in resonator performance for integrable coupling schemes, typically horizontal or vertical evanescent waveguide coupling. The trade-off between quality factor and bend radius is shown in both the microring regime (20–200 μm radius) and large bend radius regime (1–10 mm radius). Recent Si_3N_4 results from our group are highlighted in the 1–10 mm bend radius range, with new results in this Letter showing the highest integrated Q_{int} ever reported, to our knowledge.

2334-2536/14/030153-05$15/0$15.00

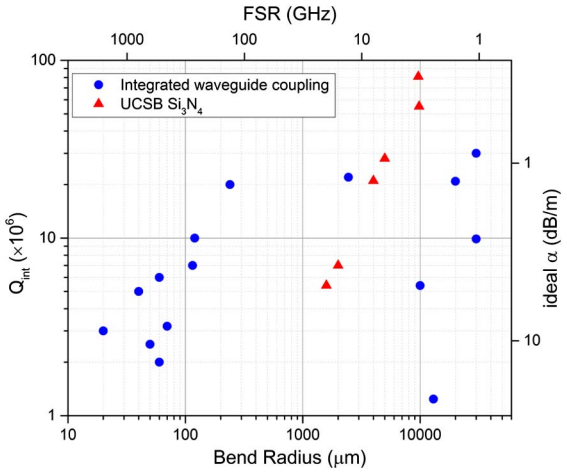

Fig. 1. State-of-the-art resonator comparison of Q_{int} versus bend radius for integrated waveguide-coupled resonators [6,8–16]. The propagation loss (α) and FSR are scaled assuming $\lambda = 1550$ nm, $n_{eff} = n_g = 1.5$, and lossless directional couplers according to Eq. (1). UCSB Si_3N_4 results [15,16], including this Letter, are highlighted in red triangles.

The theoretically obtainable Q_{int} for a given system takes into account the waveguide propagation loss, α (dB/m), directional coupler power ratio, κ, and excess directional coupler power loss per pass, γ. Equation (1) shows the obtainable Q_{load} for a given propagation loss [17]:

$$Q_{load} = \frac{2\pi n_{eff} L}{\lambda}[\kappa + \alpha L + \gamma]^{-1}. \quad (1)$$

The excess coupler loss adds parasitic loss and becomes important as it approaches the round-trip propagation loss αL. Parasitic losses can occur from scattering loss in the coupler as well as coupling into unwanted higher order or radiation modes as the coupling gap decreases, which occur for even high bend radius devices [18].

Figure 2 plots Eq. (1) without the power coupling term, κ, which is usually extracted through data analysis. In the low-loss regime of 0.2 dB/m and at a bend radius of 10 mm, efficient directional couplers with less than −30 dB excess insertion loss are required to not add appreciable loss to the system. Such low

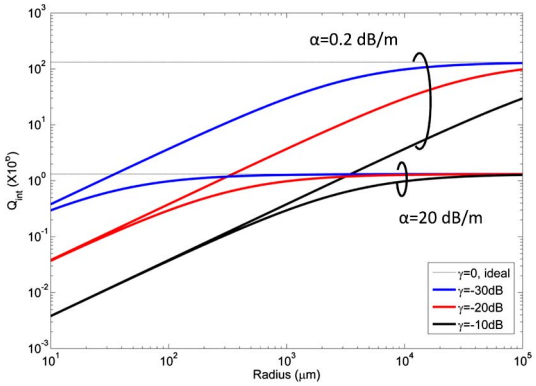

Fig. 2. Theoretically obtainable Q_{int} for a given directional coupler excess loss value, γ, and propagation loss, α, according to Eq. (1).

insertion losses are not possible to simulate in commercial software packages, and in this Letter we present experimental results showing low-loss adiabatic directional couplers in 81 million Q_{int} resonators. In our work, we target low confinement, fully monolithic Si_3N_4 waveguide structures that will be useful for future integration with silicon [19,20] and hybrid silicon III–V components [21]. High-quality Si_3N_4 is deposited via low pressure chemical vapor deposition (LPCVD) on a 15-μm-thick thermally grown SiO_2 layer on a silicon substrate. For this work, a thin 40 nm film is chosen to lower the confinement factor and decrease sidewall scattering loss at the expense of a higher bend radius device. Contact lithography defines the ring resonators and directional couplers. The bus waveguide-to-ring gap is generally >1 μm wide due to the low waveguide confinement and low coupling needed for high-Q resonators. The gaps in this study were chosen based on previous experimental results, and are identical on the add and drop ports. 3.1 μm of SiO_2 is deposited via LPCVD in three layers, with an 1150°C anneal after each layer. The sample is then chemically mechanically polished and a 15 μm thick thermal SiO_2 on Si top cladding is wafer bonded after plasma activation of the surfaces. The samples are annealed at 950°C for 3 h and diced for testing. The completed cross section is shown in Fig. 3(a), and further fabrication details can be found in [15,22].

The waveguide width now defines the number of supported modes. 7-μm-wide waveguides have produced single-mode resonators with 55 million Q_{int} [15]. Based on our previous work on ultralow-loss delay lines, the lowest loss of (0.045 ± 0.04 dB/m) has been observed in multimode waveguide spirals [22]. Assuming directional couplers without excess loss, this mean propagation loss in a resonator corresponds to a Q_{int} of 575 million. This low-loss core geometry of 11 μm × 40 nm has now been implemented in add–drop ring resonators at a bending radius of 9.65 mm, consistent with a free spectral range (FSR) of 3.3 GHz near 1580 nm. Figures 3(b)–3(d) present the simulated mode profiles for the three supported modes, TE_0, TM_0, and TE_1. The low-loss mode of interest is the TE_0 mode, which has an effective area of 33 μm^2 and core confinement factor of 3% at 1580 nm.

To study multimode resonators, care must be taken in the directional coupler design. In addition to requiring low excess coupler loss, as discussed earlier, any unwanted coupling to higher order modes will produce multiple families of resonances with different FSRs, and effectively lower the resonator Q. These corrupted spectra will produce spurious tones when filtering noise for applications such as microwave photonics. Figure 4 outlines directional coupler layouts for waveguide

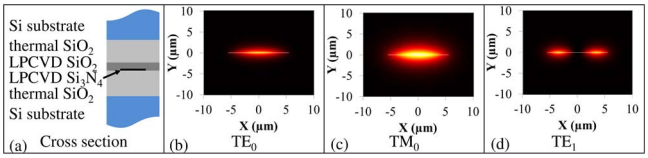

Fig. 3. (a) Waveguide cross section and (b)–(d) all supported modes of the 11 μm × 40 nm Si_3N_4 core geometry at a 9.65 mm bending radius, simulated with FIMMWAVE.

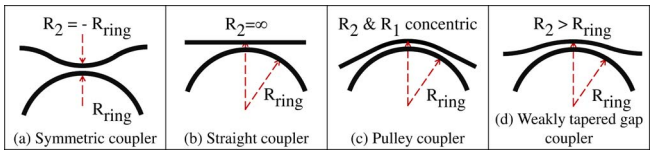

Fig. 4. Directional coupler layouts for ring resonators. The tapering of the gap is strongest for (a) symmetric coupling and identical for the (b) straight and (c) pulley couplers, while the (d) weakly tapered gap coupler smoothes the gap transition. We fabricated straight and weakly tapered gap couplers in this study.

coupled ring resonators. Figure 4(a) is a traditional symmetric coupler that is exactly beta matched but has the strongest tapering into the coupling region. Figures 4(b) and 4(d) show the two directional coupler designs studied in this Letter. The first was a straight bus waveguide coupled to the ring resonator, or "straight" coupler. We have studied these couplers on higher contrast waveguides, and our splits show an excess loss associated with a decrease in gap, yielding inefficiencies that limit the quality factor [15]. Additionally, these couplers had appreciable coupling to higher order modes, producing corrupted resonator spectra. To overcome this, we have designed a second "weakly tapered gap" directional coupler [Fig. 4(d)]. As a first experiment, we fabricate the bus waveguide with a bend radius that is 30% larger than the resonator radius to have two effects. The first is to decrease the beta mismatch between two arms of the coupler such that more efficient excitation of the fundamental mode is achieved over higher order modes. Additionally, weakly tapering the gap will yield a more adiabatic transition region from the input bus waveguide to the coupling region than the pulley, symmetric, and straight couplers of Figs. 4(a)–4(c), which we hypothesize will lower the excess loss of the coupler.

Figure 5 shows the simulated n_{eff} and n_g of the waveguide geometry's two TE modes, taking into account waveguide and bulk material chromatic dispersion [23,24]. We are mainly interested in the low-loss TE_0 mode. However, excitation of higher order modes from input tapers and/or directional couplers can corrupt the spectrum through multiple families

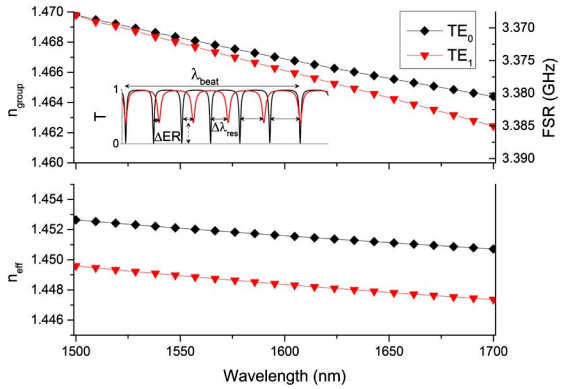

Fig. 5. Simulated TE effective and group indices for the 11 μm × 40 nm Si_3N_4 multimode waveguides studied in this Letter. Due to the fundamental TE_0 mode having a higher group index, there will be a relative resonance wavelength separation, $\Delta\lambda_{\text{res}}$ and overall beat wavelength, λ_{beat} (inset).

of resonance peaks that would have a difference of only 3 MHz in FSR at 1580 nm. This Vernier effect is shown schematically in Fig. 5 (inset) where the high n_g mode (TE_0) contains one extra resonance across a large wavelength span, termed the beat wavelength, λ_{beat}. The relative extinction ratio (ΔER) is referenced to the high n_g TE_0 mode. The separation between adjacent resonances of the two transverse modes, $\Delta\lambda_{\text{res}}$, increases with wavelength in reference to the high n_g mode. The TE_0 mode will thus have $m+1$ FSRs in λ_{beat}, where m is the number of TE_1 FSRs. The ratio of group indices is then

$$\frac{n_{g\text{TE}_0}}{n_{g\text{TE}_1}} = 1 + \frac{1}{m}. \tag{2}$$

Since the number of FSRs in λ_{beat} is dependent only on the group index ratio, measuring resonators with long cavity lengths allows for the beat wavelength to be within a reasonable measurable range. For a typical wavelength sweep of 100 nm, a 9.65 mm radius resonator will have ~3500 FSRs and a resolution down to 0.03% change in group index ratio. A higher n_g ratio will produce multiple beat frequencies in this range. To achieve the same measurement resolution would require a setup with high thermal and mechanical stability, and kilohertz level sweep accuracy for FSR extraction, such as a RF domain measurement [25,26]. We will experimentally analyze this multimode situation in the following section and use the beat wavelength to extract the resonances of each mode.

Measurement of the add–drop high-Q resonators was done in the frequency domain using a tunable external cavity laser (Agilent 86142A). The slowest sweep speed of 0.5 nm/s was used so as to avoid any ring-down effects that could occur [27]. Cleaved SMF28 fiber was used for coupling in/out of the device, and the output was coupled to a high-responsivity InGaAs detector. The photocurrent was terminated on a 1 GHz oscilloscope to enable high data rate acquisition. The wavelength regime of 1580 nm was studied for the highest Q factors, as this yields the lowest propagation loss of the platform [22]. A polarization controller was also used on the input to excite the lower loss TE polarization. The TM polarization, which has a lower confinement and higher bend loss than the TE_0 mode, was not excited due to the polarizing nature of S bends on the Si_3N_4 platform [28]. All results are averaged over multiple closely spaced resonances within 0.5 nm.

We first analyze the relative resonant wavelengths and extinction ratios (ERs) of the two directional coupler designs in the L band. Figure 6 compares a 5 μm gap straight coupler with a 3.8 μm weakly tapered gap coupler. The beat wavelength, λ_{beat}, is extracted from the two overlap points by curve fitting a second-order polynomial that accounts for dispersion. With the same nominal path length, the two resonators show $\lambda_{\text{beat}} = (73 \pm 2)$ nm, corresponding to ≈2500 resonances across this range. The ratio of n_g between TE_0 and TE_1 is found to be 1.00039 ± 0.00002, which matches well with our simulated ratio of 1.00040 ± 0.00002, for an n_g of 1.4674 and 1.4668, respectively, in the region of interest.

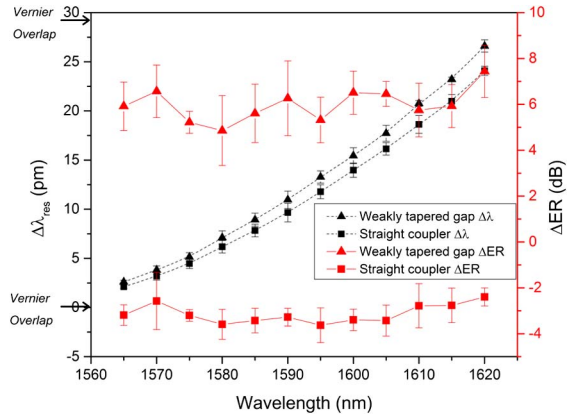

Fig. 6. Relative resonance wavelengths and ERs for the TE_0 and TE_1 modes across the region of interest. All numbers are taken relative to the fundamental TE_0 mode and averaged over multiple closely spaced resonances every 5 nm. The weakly tapered gap directional coupler resonator shows a beat wavelength of 73 nm similar to that of a straight directional coupler resonator, with an increase in absolute and relative ER.

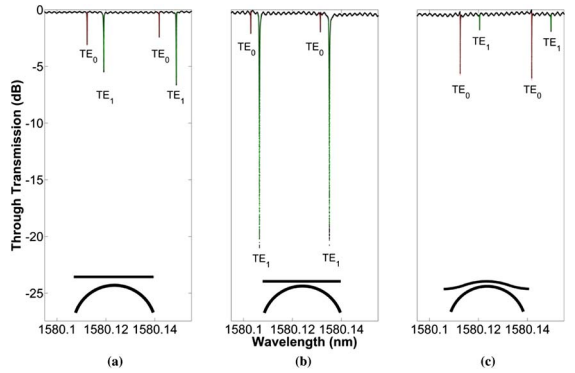

Fig. 7. Resonator spectra and fits near 1580 nm for three different directional coupler designs: (a) 5 μm straight bus waveguide, (b) 3.8 μm straight bus waveguide, and (c) 3.8 μm weakly tapered gap waveguide.

Additionally, the ΔER between modes in the two directional coupler designs changes sign. Due to these observations, we conclude that we have achieved stronger coupling to the fundamental TE_0 mode with the weakly tapered gap directional coupler as compared to the straight directional coupler.

Next, we analyze the individual resonances near 1580 nm to extract Q_{int} values. First, we show a comparison of straight couplers with two different waveguide–resonator bus gaps, 3.8 and 5 μm, in Figs. 7(a) and 7(b), respectively. The modes are labeled according to the previous modal analysis, and all devices are undercoupled due to the identical coupler layouts on the add and drop ports. For both straight coupler gaps, the higher order TE_1 mode is coupled much stronger than the lower loss fundamental mode, as observed by the magnitude of the ER. In this regime, the TE_0 mode has a maximum Q_{int} factor of 63 million at a 5 μm gap, similar to the results of the previous generation [15]. However, using a weakly tapered gap directional coupler at a 3.8 μm minimum gap at bus radius of 12.545 mm, we couple stronger and more efficiently to the fundamental TE_0 mode. This has the consequence of a higher ER than for the TE_1 mode, as seen in Fig. 7(c), as well as an even higher Q_{int} factor of 81 million, outlined in Table 1. This is the largest Q_{int} factor for a monolithic waveguide coupled resonator system to date, to our knowledge.

We have presented results on the highest integrated resonator Q_{int} values to date, to our knowledge, with a value of 81 million at a 9.65 mm bend radius. Using low confinement Si_3N_4/SiO_2 waveguides, we have utilized multimode waveguide widths and spectral analysis to extract propagation losses and directional coupler information for weakly tapered coupling gaps. These weakly tapered gap directional couplers are a critical path forward to higher quality factor integrated resonators that require increasingly efficient and low-loss coupling. Improved design of beta matched weakly tapered gap couplers should help reduce the loss of directional couplers, and full utilization of the Si_3N_4 platform, with record propagation loss of 0.05 dB/m, should be able to yield resonators with Q_{int} values of 600 million.

FUNDING INFORMATION

Defense Advanced Research Projects Agency (DARPA) (HR0011-12-C-0006); National Science Foundation (NSF) (DGE-1144085)

ACKNOWLEDGMENTS

The authors would like to thank Josh Conway, Scott Rodgers, Dan Blumenthal, Arne Leinse, and René Heideman for helpful discussions. The devices were partially fabricated at LioniX BV.

Table 1. Measured and Extracted Resonator Parameters for the Three Directional Coupler Designs Studied at 1580 nm, Assuming No Parasitic Losses ($\gamma = 0$)[a]

Gap (μm)	Mode	Q_{int} ($\times 10^6$)	Q_{load} ($\times 10^6$)	RTL (dB)	α (dB/m)	κ (%)	ER (dB)
5.0	TE_0	63	46	0.026	0.42	0.11	2.7
5.0	TE_1	27	13	0.061	1.00	0.72	6.1
3.8	TE_0	35	28	0.047	0.78	0.13	1.8
3.8	TE_1	41	4	0.038	0.63	4.07	20.2
3.8-taper	TE_0	**81**	**42**	**0.019**	**0.32**	**0.20**	**5.6**
3.8-taper	TE_1	30	26	0.055	0.90	0.11	1.4

[a]The bend radius is 9.65 mm, and nominal gap widths are shown. The measured Q_{load} and ER allow extraction of the power coupling coefficient (κ), Q_{int}, propagation loss (α), and round-trip loss (RTL). The RTL is the upper bound on γ for two directional couplers.

REFERENCES

1. M. J. R. Heck, J. F. Bauters, M. L. Davenport, D. T. Spencer, and J. E. Bowers, "Ultra-low loss waveguide platform and its integration with silicon photonics," Laser Photon. Rev., doi: 10.1002/lpor.201300183 (posted online March 5, 2014).
2. D. Marpaung, C. Roeloffzen, R. Heideman, A. Leinse, S. Sales, and J. Capmany, Laser Photon. Rev. **7**, 506 (2013).
3. D. Cabric, M. S. W. Chen, D. A. Sobel, S. Wang, J. Yang, and R. W. Brodersen, EURASIP J. Wirel. Commun. Netw. **2006**, 1 (2006).
4. J. R. Vig, "Introduction to quartz frequency standards," Res. Dev. Tech. Rep. SLCET-TR-92-1 1 (U.S. Army Electronics Technology and Devices Laboratory, 1992).
5. P. Maddaloni, M. Bellini, and P. De Natale, *Laser-Based Measurements for Time and Frequency Domain Applications* (Taylor & Francis, 2013).
6. C. Ciminelli, F. Dell'Olio, M. N. Armenise, F. M. Soares, and W. Passenberg, Opt. Express **21**, 556 (2013).
7. C. Ciminelli, F. Dell'Olio, and M. N. Armenise, IEEE Photon. J. **4**, 1844 (2012).
8. A. Biberman, M. J. Shaw, E. Timurdogan, J. B. Wright, and M. R. Watts, Opt. Lett. **37**, 4236 (2012).
9. R. Adar, Y. Shani, and C. Henry, Appl. Phys. Lett. **58**, 444 (1991).
10. R. Adar, M. R. Serbin, and V. Mizrahi, J. Lightwave Technol. **12**, 1369 (1994).
11. Q. Li, A. A. Eftekhar, M. Sodagar, Z. Xia, A. H. Atabaki, and A. Adibi, Opt. Express **21**, 18236 (2013).
12. A. Gondarenko, J. S. Levy, and M. Lipson, Opt. Express **17**, 11366 (2009).
13. K. Luke, A. Dutt, C. B. Poitras, and M. Lipson, Opt. Express **21**, 22829 (2013).
14. L. Zhuang, D. Marpaung, M. Burla, W. Beeker, A. Leinse, and C. Roeloffzen, Opt. Express **19**, 23162 (2011).
15. D. T. Spencer, Y. Tang, J. F. Bauters, M. J. R. Heck, and J. E. Bowers, in *IEEE Photonics Conference* (Institute of Electrical and Electronics Engineers, 2012), pp. 141–142.
16. M.-C. Tien, J. F. Bauters, M. J. R. Heck, D. T. Spencer, D. J. Blumenthal, and J. E. Bowers, Opt. Express **19**, 13551 (2011).
17. O. Schwelb, J. Lightwave Technol. **22**, 1380 (2004).
18. D. Ding, M. J. A. de Dood, J. F. Bauters, M. J. R. Heck, J. E. Bowers, and D. Bouwmeester, Opt. Express **22**, 6778 (2014).
19. T. Tsuchizawa and K. Yamada, IEEE J. Sel. Top. Quantum Electron. **17**, 516 (2011).
20. J. F. Bauters, M. L. Davenport, M. J. R. Heck, J. K. Doylend, A. Chen, A. W. Fang, and J. E. Bowers, Opt. Express **21**, 544 (2013).
21. M. Piels, J. Bauters, M. Davenport, M. Heck, and J. Bowers, J. Lightwave Technol. **32**, 817 (2013).
22. J. F. Bauters, M. J. R. Heck, D. D. John, J. S. Barton, C. M. Bruinink, A. Leinse, R. G. Heideman, D. J. Blumenthal, and J. E. Bowers, Opt. Express **19**, 24090 (2011).
23. H. R. Philipp, J. Electrochem. Soc. **120**, 295 (1973).
24. T. Bååk, Appl. Opt. **21**, 1069 (1982).
25. N. Uehara and K. Ueda, Appl. Phys. B **61**, 9 (1995).
26. B. J. J. Slagmolen, M. B. Gray, K. G. Baigent, and D. E. McClelland, Appl. Opt. **39**, 3638 (2000).
27. A. A. Savchenkov, A. B. Matsko, V. S. Ilchenko, and L. Maleki, Opt. Express **15**, 6768 (2007).
28. J. F. Bauters, M. J. R. Heck, D. Dai, J. S. Barton, D. J. Blumenthal, and J. E. Bowers, IEEE Photon. J. **5**, 6600207 (2013).

Research Article Vol. 1, No. 3 / September 2014 / Optica 158

CW-pumped single-pass frequency comb generation by resonant optomechanical nonlinearity in dual-nanoweb fiber

A. Butsch,* J. R. Koehler, R. E. Noskov, and P. St.J. Russell

Max Planck Institute for the Science of Light, Guenther-Scharowsky-Str. 1, 91058 Erlangen, Germany

**Corresponding author: anna.butsch@mpl.mpg.de*

Received 23 May 2014; revised 6 August 2014; accepted 6 August 2014 (Doc. ID 212716); published 10 September 2014

Recent experiments in the field of strong optomechanical interactions have focused on either structures that are simultaneously optically and mechanically resonant, or photonic crystal fibers pumped by a laser intensity modulated at a mechanical resonant frequency of the glass core. Here, we report continuous-wave (CW) pumped self-oscillations of a fiber nanostructure that is only mechanically resonant. Since the mechanism has close similarities to stimulated Raman scattering by molecules, it has been named stimulated Raman-like scattering. The structure consists of two submicrometer thick glass membranes (nanowebs), spaced by a few hundred nanometers and supported inside a 12-cm-long capillary fiber. It is driven into oscillation by a CW pump laser at powers as low as a few milliwatts. As the pump power is increased above threshold, a comb of Stokes and anti-Stokes lines is generated, spaced by the oscillator frequency of ~6 MHz. An unprecedentedly high Raman-like gain of $\sim 4 \times 10^6$ m^{-1} W^{-1} is inferred after analysis of the experimental data. Resonant frequencies as high as a few hundred megahertz are possible through the use of thicker and less-wide webs, suggesting that the structure can find application in passive mode-locking of fiber lasers, optical frequency metrology, and spectroscopy.

OCIS codes: (200.4880) Optomechanics; (190.5890) Scattering, stimulated; (060.4005) Microstructured fibers; (190.4370) Nonlinear optics, fibers.

http://dx.doi.org/10.1364/OPTICA.1.000158

1. INTRODUCTION

In recent years, a major thrust in optomechanics has been the observation of light–matter interactions at the single quantum level [1,2]. Remarkable microstructures have been developed in which both light and acoustic vibrations are tightly confined within a small volume for relatively long periods of time, and thus forced to interact strongly. An extensive review of the recent progress in this field can be found in [3].

Another goal of optomechanics has been the design of micro/nanostructures that display very high optomechanical nonlinearities, through either electrostrictive changes in refractive index [4,5] or radiation-pressure-driven changes in morphology [6,7]. For example, in small-core silica–air photonic crystal fibers, it has been shown that acoustic core resonances at few-gigahertz frequencies can be excited electrostrictively by pumping with dual-frequency laser light [8]. These core resonances then act back on the light, resulting in the generation of an optical frequency comb. This process, which was named stimulated Raman-like scattering (SRLS), has been used to passively mode lock a fiber ring laser at gigahertz frequencies [9].

Another example is the dual-nanoweb fiber (the subject of this work), a structure that displays a giant optomechanical nonlinearity as a result of the high mechanical compliance of two very thin, wide, and closely spaced glass "nanowebs" mounted inside a fiber capillary [see Fig. 1(a)] [10]. When light of only a few milliwatts is launched into the nanowebs so that the phase across them is constant (i.e., the even mode is excited), optical gradient forces cause the webs to be pulled

2334-2536/14/030158-07$15/0$15.00

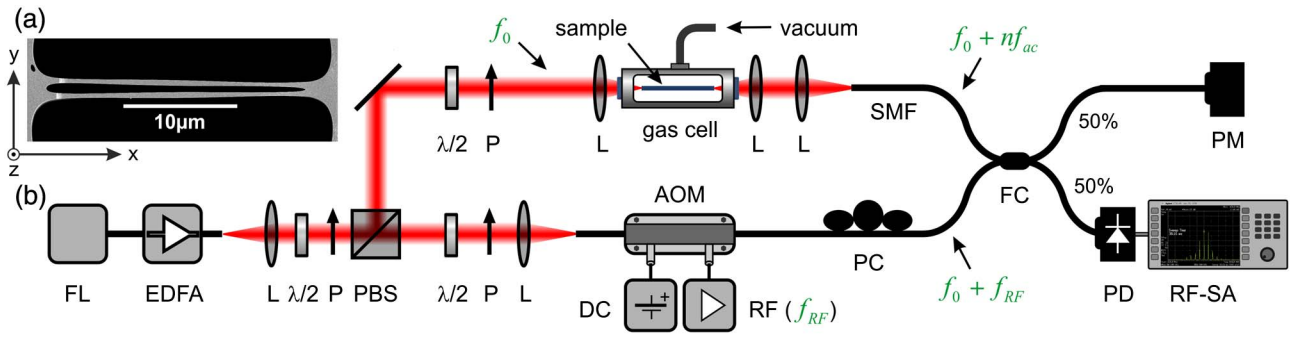

Fig. 1. (a) Scanning electron micrograph of the fiber core region: the width w of the dual-nanoweb waveguide is ~22 μm, the upper and lower web thicknesses in the center are $h_u \sim 460$ nm and $h_l \sim 480$ nm, and the gap thickness is $h_g \sim 550$ nm. The sample length L is 12 cm. (b) Schematic of the heterodyne detection setup with an evacuated dual-nanoweb fiber sample. FL, fiber laser; EDFA, erbium-doped fiber amplifier; L, lens; P, polarizer; PBS, polarizing beam splitter; AOM, acousto-optical modulator; SMF, single mode fiber; PC, polarization controller; FC, fiber coupler; PD, photodiode; RF-SA, radio-frequency spectrum analyzer; PM, power meter.

together, increasing the effective index of the mode. If the odd mode is instead excited, the webs are pushed apart, but the modal index still rises [11].

In a previous study, the frequency response of this nonlinearity was measured at different gas pressures [12]. When driven by a laser beam intensity-modulated at the frequency of the fundamental flexural resonance of the nanowebs, effective optomechanical nonlinearities ($m^{-1}\,W^{-1}$) some 60,000 times higher than the Kerr-related nonlinearity were measured.

Something more intriguing is observed, however, when the gas pressure is reduced to the μbar range (thus eliminating viscous damping and squeezed-film effects) and the structure is pumped with CW light. Above a sharp threshold of a few milliwatts, the output signal begins to oscillate in intensity and sidebands appear in the optical frequency spectrum [13]. Unlike in previous experiments with CW light where optical cavities with high Q factors (for example, in highly nonlinear fibers [14] or whispering gallery mode resonators [15]) were used to generate frequency combs via the electronic Kerr effect, the underlying mechanism in our case is SRLS. As we will show, this effect is initiated by scattering of light at thermally excited phonons. This gives rise to weak uncorrelated Stokes (S) and anti-Stokes (AS) signals. For certain combinations of the randomly fluctuating phases of these signals, the beat note with the pump light drives the acoustic resonance more strongly, further enhancing scattering into the sidebands. An optical frequency comb spaced by the acoustic resonant frequency (~6 MHz) is created. Symmetry between S and AS scattering causes suppression of pump-to-Stokes Raman gain in gases in the special case when both S and AS are phase-matched to the same coherence wave [16]. In our case, however, because of the much stronger thermal vibrations at 6 MHz (kT-driven molecular excitations are vanishingly weak at the multiterahertz frequencies typical of gases) enhanced by the high mechanical Q factor, a substantial population of stochastic thermal phonons is available to stimulate Stokes photon creation, or to cause frequency up-shifting to the anti-Stokes. As a result, no gain suppression is seen.

Here, we report in detail on this new phenomenon, which can be viewed as the first example of noise-seeded, optomechanical SRLS; the dual-nanoweb structure behaves like a sort of "artificial Raman-active molecule."

2. STRUCTURE, SETUP, AND EXPERIMENTAL RESULTS

The ~22 μm wide waveguide region of the dual-nanoweb fiber consists of two optically coupled nanowebs with slightly convex thickness profiles. The thicknesses of the upper and lower nanowebs are ~460 nm and ~480 nm at the center, and the gap between them is ~550 nm wide [Fig. 1(a)]. In the experiment, a 12 cm long sample was used, mounted in a gas cell with windows at each end and evacuated to a pressure of ~1 μbar. This strongly enhanced the Q factor of the acoustic vibrations and the strength of the resonant optomechanical nonlinearity [12]. As explained above, the system began oscillating when a few milliwatts of CW laser light at 1550 nm was launched into the fiber [13]. The resulting RF spectrum was measured with high resolution using the heterodyne setup depicted in Fig. 1(b).

The laser system comprised a narrow-linewidth single-mode fiber laser (3 dB linewidth ~3 kHz) and an erbium-doped fiber amplifier (EDFA). Using a combination of $\lambda/2$ plate and polarizer before and after the polarizing beam splitter, the power and polarization state in both the sample and the local oscillator (LO) paths could be controlled. TE-polarized light was launched into the sample and the transmitted signal, containing the pump and the optomechanically created sidebands, was coupled into a single mode fiber and mixed with the LO signal at a fiber coupler. In the LO path, an acousto-optical modulator was used to upshift the optical carrier frequency by 200 MHz. The beat note between the signals transmitted through the sample and LO path was then detected using a fast photodiode and visualized using a radio-frequency spectrum analyzer. The RF power P_n^{RF} of the beat note between the nth comb component with power P_n and the LO with power P_{LO} is proportional to the product of both optical powers, i.e., $P_n^{\mathrm{RF}} \propto P_n P_{\mathrm{LO}}$ [17].

In Fig. 2, a series of four RF spectra are shown, measured at different launched pump powers P_{IN} and constant P_{LO}, the RF power therefore being proportional to the optical power

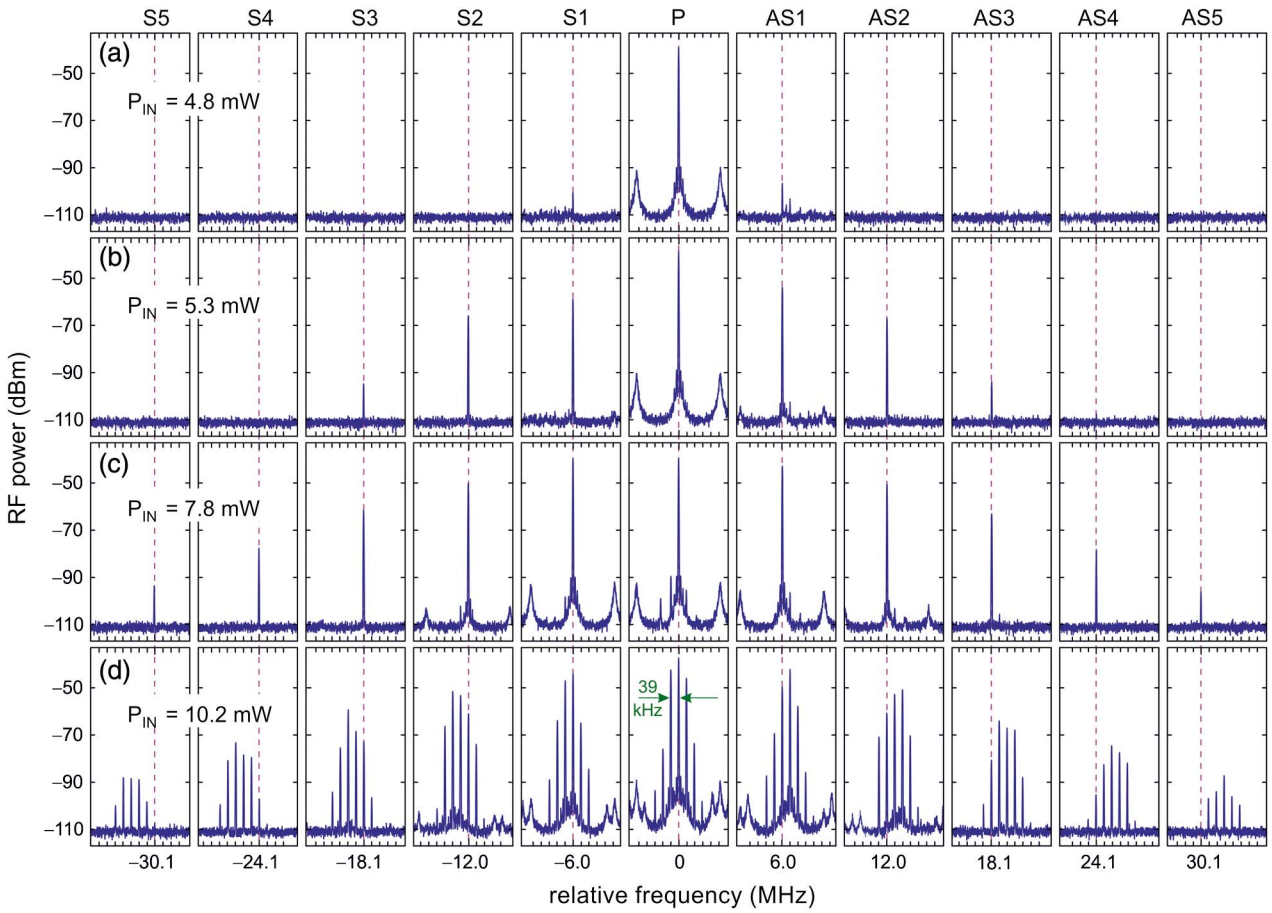

Fig. 2. RF spectra of the transmitted optical signal measured at different CW input powers. The frequency was scanned over 500 kHz around each of the comb sidebands at multiples of ±6.022 MHz. (a) Initial amplification of first-order S and AS components at 4.8 mW input power. (b) At 5.3 mW, three sidebands appear on each side of the pump peak. (c) S and AS components up to fifth order are detected at 7.8 mW input power. (d) At 10.2 mW, a fine structure of lines with a spacing of 39 kHz appears around each of the main comb components. The tick spacing on the frequency axis of each pane is 39 kHz.

of the corresponding comb component. Note that the laser system exhibits sidebands at ±210 kHz relative frequency, which are, however, suppressed by more than 53 dB relative to the main laser line and cannot seed any optomechanical sidebands due to the frequency mismatch. The spectrum at 4.8 mW exhibits, on either side of the pump peak (at zero relative frequency and ∼70 dB above the background noise), small S and AS peaks (∼10 dB above the noise level) at ±6.022 MHz, corresponding to the fundamental flexural resonance of the structure. As the input power is increased to 5.3 mW, six sidebands spaced by 6.022 MHz can already be distinguished. At 7.8 mW, the number of sidebands increases to ten. When the launched power is raised above ∼8 mW, a fine structure of the comb lines with a frequency spacing of 39 kHz appears, and at 10.2 mW, four to six secondary comb lines can be observed around each of the main peaks. When the air pressure inside the fiber is increased to a few mbar, viscous damping of the flexural vibrations causes the threshold power for the onset of comb generation to rise considerably, until above ∼100 mbar it is no longer possible to generate a frequency comb at the power levels available in the experiment.

To further characterize the system, we measured the SRLS gain spectrum using the copolarized dual-frequency (pump+S) excitation technique [8]. This involved inserting an electro-optic modulator driven by a function generator before the EDFA, its DC bias adjusted so that two equal amplitude sidebands are synthesized and the carrier wave strongly suppressed.

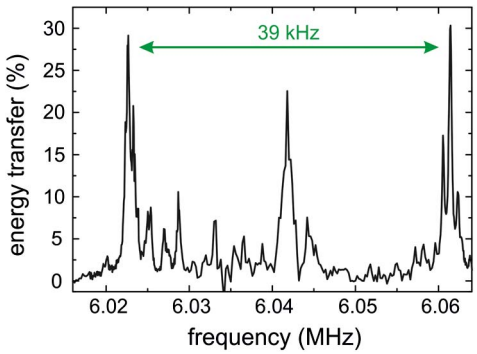

Fig. 3. Energy transfer from pump to Stokes as a function of the frequency spacing of the dual-frequency light (50% pump and 50% Stokes) at 2 mW launched total power.

Figure 3 shows the energy transfer from the pump to the S wave, after propagation through the dual-web fiber, as a function of the frequency spacing between them. The total launched power level was kept at a low ~2 mW so as to minimize conversion to higher-order sidebands. Interestingly, the spectrum reveals clusters of closely spaced sharp peaks, similar to those observed previously [12]. These peaks we attribute to flexural resonances localized at structural nonuniformities along the fiber sample. Two distinct resonances appear at 6.022 and 6.061 MHz, spaced 39 kHz and, as we will show later, the interaction between these resonances leads to the generation of the fine structure of the comb lines.

3. MECHANISM AND THEORY

In this section, we set up a theoretical model for the noise-initiated SRLS and determine its gain characteristics. We restrict the analysis to the lowest-order TE-polarized optical mode [single-lobed in the y and x directions, Fig. 1(a)] and the fundamental acoustic flexural mode (single-lobed in the x direction) [10]. The flat dispersion curve of the flexural mode and the small frequency shift (cut-off frequency ~6 MHz) ensure that the same phonon can cause phase-matched coupling between successive S and AS components (Fig. 4). This means that the model must take into account a large number of comb components, spaced by ~6 MHz.

The nonlinear wave equation for the electric field may be written as [8]

$$\frac{\partial^2 E}{\partial z^2} - \frac{n_m^2}{c^2}\frac{\partial^2 E}{\partial t^2} = \frac{1}{\varepsilon_0 c^2}\frac{\partial^2 P_{\mathrm{NL}}}{\partial t^2}, \tag{1}$$

where the nonlinear polarization P_{NL} describes the coupling between optical and acoustic fields. The refractive index of the optical mode is n_m, ε_0 is the dielectric permittivity, and c is the speed of light *in vacuo*. The optomechanical nonlinearity originates from the interdependence of optical gradient forces and deflection-dependent changes in n_m, and strongly dominates over the contributions of photoelasticity and electrostriction, which we therefore neglect. P_{NL} can therefore be expressed to first order as [18]

$$P_{\mathrm{NL}} = \varepsilon_0 \frac{\partial \varepsilon}{\partial \delta}\delta E = 2\varepsilon_0 n_m \frac{\partial n_m}{\partial \delta}\delta E. \tag{2}$$

The web deflection δ is governed by the flexural wave equation for a thin plate [19,20]:

$$D\left(1+\tau\frac{\partial}{\partial t}\right)\left(\frac{\partial^4\delta}{\partial x^4}+2\frac{\partial^4\delta}{\partial x^2\partial z^2}+\frac{\partial^4\delta}{\partial z^4}\right)+\sigma\frac{\partial^2\delta}{\partial t^2} = p_{\mathrm{opt}}+\tilde{f}\approx\frac{\varepsilon_0}{2}[E^2]_{y=y_{\mathrm{lower}}}^{y=y_{\mathrm{upper}}}+\tilde{f}, \tag{3}$$

where $D = Yh^3/[12(1-\nu^2)]$ is the flexural rigidity of a nanoweb with thickness h, Y is the Young's modulus, and ν is the Poisson's ratio. The parameter τ is related to the damping rate (see below). The driving term is given by the optical gradient pressure p_{opt}, which can be calculated using the Maxwell stress tensor [11]. To simplify the analysis, we neglect magnetic field components (they contribute only ~6% to the interweb force) and approximate p_{opt} acting on one web by evaluating the difference between the squared electric fields at its upper and lower surfaces [18]. Further, in Eq. (3), we have introduced a Langevin noise source $\tilde{f}$ describing the thermal excitation of acoustic waves, based on δ-correlated Gaussian noise [21].

Assuming that the fiber has no structural nonuniformities along its length, the electric field, containing an infinite number of copolarized equidistant-in-frequency components, can be written in the form

$$E(x,y,z,t) = s(x)f(y)\sqrt{\frac{P_0 Z_0}{2n_m}}\sum_n a_n(z,t)e^{i(\beta_n z-\omega_n t)} + \mathrm{c.c.}, \tag{4}$$

where Z_0 is the impedance of vacuum, P_0 is the launched optical power, and $s(x)f(y)$ represents the transverse field distribution of the optical mode, normalized so that $\int_{-w/2}^{w/2}|s(x)|^2\mathrm{d}x = 1$ and $\int_{-\infty}^{\infty}|f(y)|^2\mathrm{d}y = 1$. For the structures studied here, $s(x)f(y)$ can be taken to be independent of power for launched powers in the milliwatts range [10]. Within this normalization, $s(x)$ and $f(y)$ have units $\mathrm{m}^{-1/2}$. The dimensionless functions $a_n(z,t)$ represent the slowly varying field amplitudes of the comb lines, with frequency $\omega_n = \omega_0 + n\Omega$ and axial propagation constant $\beta_n = \beta_0 + nq$, where ω_0 is the angular frequency, β_0 is the wavevector of the pump mode, and $n = \pm1, \pm2, \ldots$ is the sideband order, negative values corresponding to S frequencies.

For a flexural wave with axial propagation constant q and frequency Ω close to the cut-off frequency, which is given approximately by $\Omega_{\mathrm{co}} \approx (\pi/w)^2\sqrt{D/\sigma}$, we can use the Ansatz:

$$\delta(x,z,t) = \delta_0(x)\sqrt{\frac{e_{\mathrm{ac}}}{2\sigma\Omega_{\mathrm{co}}^2}}b(z,t)e^{i(qz-\Omega t)} + \mathrm{c.c.}, \tag{5}$$

where $\sigma = \rho h$ is the mass per unit area of a web, e_{ac} is the acoustic energy per unit length in the axial direction, $\delta_0(x)$

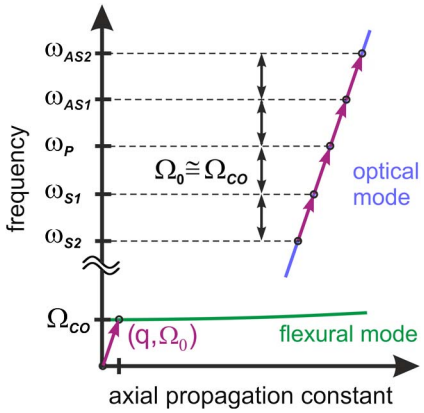

Fig. 4. Schematic of the dispersion diagram for SRLS by guided flexural waves with a cut-off angular frequency Ω_{co}. A phonon with frequency $\Omega_0 \approx \Omega_{\mathrm{co}}$ and propagation constant q automatically provides phase matching between successive optical S and AS components.

is the transverse profile of the flexural resonance (with units $m^{-1/2}$) normalized so that $\int_{-w/2}^{w/2} |\delta_0(x)|^2 dx = 1$, and $b(z, t)$ is the dimensionless slowly varying envelope of the flexural mode. The transverse profile has been taken for simplicity to be $\delta_0(x) = (2/w)^{1/2} \cos(\pi x/w)$, which approximates to its shape at the cut-off frequency. Substituting this expression into Eq. (3) in the absence of any driving terms and assuming exponential decay of sinusoidal oscillation in time yields a decay rate $\Gamma = \tau\Omega_{co}^2$.

Note that, although q is non-zero in the experiment, it is very small, taking the value $q = \beta_p - \beta_S \approx 2\pi f_{ac} n_m/c = 0.15\ m^{-1}$ for acoustic frequency $f_{ac} = 6$ MHz and modal index $n_m = 1.2$. This yields an axial acoustic wavelength of ~42 m, i.e., much longer than the fiber sample. Thus, in Eq. (3), we can assume that the z derivative of the deflection is negligibly small compared to its x derivative.

Now we apply the slowly varying envelope approximation to Eqs. (1) and (3), considering only those components of the optical driving term that oscillate with the same frequency and wavevector as the acoustic wave. Since the group velocity of the guided flexural wave at $\Omega_0 \approx \Omega_{co}$ is nearly zero (Fig. 4), we can neglect phonon propagation, i.e., set $\partial b/\partial z \approx 0$, and obtain the following set of coupled equations:

$$\frac{\partial a_n}{\partial z} + \frac{1}{v_g}\frac{\partial a_n}{\partial t} = i\kappa(b a_{n-1} + b^* a_{n+1}),$$
$$\frac{\partial b}{\partial t} + \left(\frac{\Gamma}{2} + \frac{\Omega^2 - \Omega_0^2}{2i\Omega}\right) b = i\gamma \sum_n a_n a_{n-1}^* + \xi_L, \quad (6)$$

where $v_g = \partial\omega/\partial\beta$ is the group velocity of the light (which is effectively identical for every frequency component) and ξ_L is the rate of seeding by Langevin noise, which is related to the forcing term in Eq. (3) via $\tilde{f} = -i\Omega\xi_L\zeta \exp(i(qz - \Omega t)) + \text{c.c.}$, where ζ and the other parameters in Eq. (6) are defined in Appendix A.

By eliminating $b(z)$ from Eqs. (6), the evolution of the fields can be rewritten for exact phase matching ($\Omega = \Omega_0$) and in the steady-state ($\partial/\partial t = 0$) for time-averaged values of all quantities as follows:

$$\frac{\partial a_n}{\partial z} = \frac{g_0 P_0}{2}\left(-a_{n-1}\sum_l a_l a_{l-1}^* + a_{n+1}\sum_l a_{l-1} a_l^*\right) + i\frac{2\kappa}{\Gamma}(\xi_L^{n-1} a_{n-1} + \xi_L^{n+1} a_{n+1}),$$
$$g_0 = \frac{4\kappa\gamma}{\Gamma P_0} = \frac{\omega_0 Q_{om}^2}{n_m c^2 h_p \sigma \Omega_0 \Gamma}\frac{\partial n_m}{\partial \delta}. \quad (7)$$

Since the frequency spacing between different optical comb lines and the spectral width of the comb in the experiment are much smaller than the carrier frequency of the pump wave, we have approximated ω_n by ω_0 for all n. The uncorrelated Langevin noise terms ξ_L^{n-1} and ξ_L^{n+1} (causing coupling to a_n from the lower- and higher-frequency sidebands) have the same statistics and are calculated anew for each realization of the code.

To quantify the gain factor g_0, we calculate the overlap between the optical mode and the flexural mode, using the numerical technique described in [11] and considering the geometry of the experimental structure. This results in $n_m = 1.24$, $\partial n_m/\partial\delta = -64 \times 10^3\ m^{-1}$ at the center of the optical mode, $h_p = -6.8 \times 10^{-6}$ m, and $Q_{om} = 661\ m^{-1/2}$. Further, we take the area density $\sigma = 10^{-3}\ kg/m^2$, the experimental values of the mechanical resonance frequency $\Omega_0 = 2\pi \times 6.022$ MHz and linewidth $\Gamma \approx 1$ kHz, and calculate the gain coefficient at $\lambda = 1.55$ μm to be $g_0 \approx 10^6\ m^{-1}\,W^{-1}$. This exceeds the SRLS gain in small-core PCF [8] by six orders of magnitude.

4. DISCUSSION

The data points in Fig. 5 represent the measured powers in each optical sideband (normalized to the total power) at several different values of launched power. A pronounced threshold is observed at ~4.9 mW, which is not observed in numerical solutions of Eq. (7), which show that the sidebands begin to grow immediately even at infinitesimal power levels.

To explain the existence of the oscillation threshold in the experiment, we have found it necessary to consider acoustic mode competition in the system, by analogy with cavity mode competition in lasers. As mentioned before, structural nonuniformities are known to exist along the fiber. These will cause the appearance of many acoustic resonances, each with a slightly different frequency, localized at different positions along the fiber (see Fig. 3). Since all these resonances interact with the same guided optical mode and have similar gain characteristics, they destructively interfere, suppressing the SRLS process as long as the input power stays below a critical value.

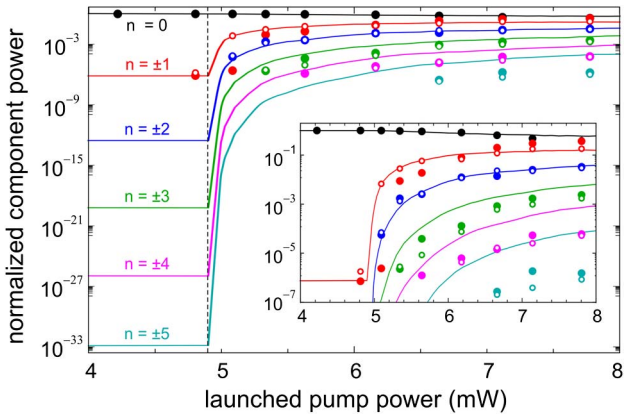

Fig. 5. Evolution of the power in the comb lines (normalized to the total output power) as a function of the launched pump power. Full and open circles represent experimental data for the S and AS components, respectively. Full lines show the theoretical expectations for the pump (black), the first-order (red), second-order (blue), third-order (green), fourth-order (magenta), and fifth-order (cyan) S and AS using the fit parameters $g_0 = 4 \times 10^6\ m^{-1}\,W^{-1}$ and an effective comb generation length $L_{eff} = 6$ cm. A distinct threshold for the onset of frequency comb generation occurs at a launched power of ~4.9 mW, marked by the dashed vertical line. Below threshold, the power in each comb line decreases exponentially with its order. The inset shows the experimentally relevant data range above a noise floor of $\sim 10^{-7}$ relative to the pump power.

In our model we assume that, due to the Lorentzian lineshape of the gain profile, there is a power-dependent line narrowing that gradually reduces the overlap between competing acoustic modes. Above the critical power, the overlap is weak enough and the mode competition eliminated, so that a subset of the localized acoustic modes switches from random motion with zero mean phonon amplitude to coherent vibration with finite mean phonon amplitude. Thus, the effective nonlinear interaction length L_{eff} increases and consecutive optical sidebands are generated and amplified via SRLS.

The theoretical plots in Fig. 5 (solid lines) were obtained by numerically solving a model for acoustic mode competition and calculating the average from a set of 1000 different realizations seeded by stochastic acoustic noise. Good quantitative agreement with the experimental data is obtained using $g_0 = 4 \times 10^6\ \text{m}^{-1}\,\text{W}^{-1}$ and $L_{\text{eff}} = 6$ cm as the effective nonlinear length. Given the uncertainties in the values of acoustic linewidth and L_{eff}, the agreement between the theoretical and experimental values of gain is good. Due to the resolution limit of the measurement, the estimated acoustic linewidth (1 kHz) is likely to be too high, leading to an underestimate of the experimental gain. Also, uncertainty in L_{eff} leads to uncertainty in the value of g_0, since only the product $g_0 L_{\text{eff}}$ can be measured experimentally.

Finally, we address the appearance of secondary frequency combs around each primary sideband at pump powers above ~8 mW [Fig. 2(d)]. These arise from the presence of a second localized resonance at a slightly different frequency, caused by nonuniformities in the nanoweb structure (we have recently observed this using a side-scattering technique, to be reported elsewhere). This second resonance has a higher threshold power and acts on all the frequency components of the primary comb, so that each of the primary sidebands (spaced by $f_1 = 6.022$ MHz) pumps a secondary comb with a slightly different frequency spacing ($f_2 = 6.061$ MHz), resulting in the generation of a multiplicity of finely spaced frequencies $f = f_0 + nf_1 + mf_2$. As the spacing of the secondary comb is 39 kHz larger than that of the primary comb, the fine structure of the comb lines is offset by $n(f_2 - f_1) = n \times 39$ kHz from the center of the nth primary sideband. The remarkably high gain factor of SRLS results in full energy transfer from the primary fifth S and AS signals to the secondary comb lines at a pump power of 10.2 mW. An extended theory (to be published in detail elsewhere), including acoustic mode competition and dual-comb generation, confirms this picture.

5. CONCLUSIONS

A mechanically highly compliant nanostructure, consisting of two very thin glass membrane waveguides, experiences strong optical gradient forces when light is launched into it. The resulting mechanical deformation results in a large increase in effective modal phase index, i.e., a giant optomechanical nonlinearity. As a result, when the structure is pumped with CW laser light at the few-milliwatts level, it behaves like an artificial Raman-active molecule, causing the generation of a frequency comb with spacing equal to the acoustic resonant frequency.

This is the first time that single-pass stimulated Raman-like scattering, seeded from noise, has been observed in a nanomechanical resonator. By using thicker and less-wide webs, resonant frequencies as high as a few hundred megahertz seem possible (albeit with lower gain), suggesting that the structure may be useful in optical frequency metrology, spectroscopy, and passive mode locking of fiber lasers.

APPENDIX A

The constants in Eq. (6) are the rate of coupling per unit length between the optical frequency components

$$\kappa = \frac{\omega_0}{2c}\frac{\partial n_m}{\partial \delta} Q_{\text{om}} \sqrt{\frac{2e_{\text{ac}}}{\sigma \Omega_0^2}} \tag{A1}$$

and the rate of coupling per unit time from the optical beat note to the acoustic resonance

$$\gamma = \frac{\varepsilon_0 Z_0 P_0 Q_{\text{om}}}{2h_p n_m \sqrt{2\sigma e_{\text{ac}}}}, \tag{A2}$$

where

$$Q_{\text{om}} = \int_{-w/2}^{w/2} \delta_0(x)|s(x)|^2 \mathrm{d}x \tag{A3}$$

is the optomechanical overlap integral and h_p is a characteristic length given by [18]

$$h_p = (|f(y_{\text{upper}})|^2 - |f(y_{\text{lower}})|^2)^{-1}, \tag{A4}$$

where y_{upper} and y_{lower} are the positions of the upper and lower boundaries of a single nanoweb.

The statistics of the Langevin noise seeding rate ξ_L in Eq. (6) are defined as [21]

$$\langle \xi_L(z,t) \rangle = 0 \quad \text{and}$$
$$\langle \xi_L(z,t)\xi_L^*(z',t') \rangle = \frac{k_B T}{e_{\text{ac}}} \Gamma \delta(z-z')\delta(t-t'). \tag{A5}$$

Here, k_B denotes Boltzmann's constant and T is the ambient temperature. These expressions are used to stochastically initiate the system in the numerical simulations.

Finally, the parameter ζ used to relate $\tilde{f}$ to ξ_L takes the form

$$\zeta = \frac{\sqrt{2\sigma e_{\text{ac}}}}{\Omega_0} \left(\int_{-w/2}^{w/2} \delta_0(x)\mathrm{d}x \right)^{-1} = \frac{\pi}{2\Omega_0} \sqrt{\frac{\sigma e_{\text{ac}}}{w}}. \tag{A6}$$

Note that this expression applies only to the fundamental flexural mode.

FUNDING INFORMATION

Max Planck Society

REFERENCES

1. R. Riviere, S. Deleglise, S. Weis, E. Gavartin, O. Arcizet, A. Schliesser, and T. J. Kippenberg, "Optomechanical sideband cooling of a micromechanical oscillator close to the quantum ground state," Phys. Rev. A **83**, 063835 (2011).
2. A. H. Safavi-Naeini, J. Chan, J. T. Hill, T. P. M. Alegre, A. Krause, and O. J. Painter, "Observation of quantum motion of a nanomechanical resonator," Phys. Rev. Lett. **108**, 033602 (2012).
3. M. Aspelmeyer, T. J. Kippenberg, and F. Marquardt, "Cavity optomechanics," arXiv:1303.0733v1 (2013).
4. P. Dainese, P. St.J. Russell, G. S. Wiederhecker, N. Joly, H. L. Fragnito, V. Laude, and A. Khelif, "Raman-like light scattering from acoustic phonons in photonic crystal fiber," Opt. Express **14**, 4141–4150 (2006).
5. G. Bahl, J. Zehnpfennig, M. Tomes, and T. Carmon, "Stimulated optomechanical excitation of surface acoustic waves in a microdevice," Nat. Commun. **2**, 403 (2011).
6. W. H. P. Pernice, M. Li, and H. X. Tang, "A mechanical Kerr effect in deformable photonic media," Appl. Phys. Lett. **95**, 123507 (2009).
7. D. Van Thourhout and J. Roels, "Optomechanical device actuation through the optical gradient force," Nat. Photonics **4**, 211–217 (2010).
8. M. S. Kang, A. Nazarkin, A. Brenn, and P. St.J. Russell, "Tightly trapped acoustic phonons in photonic crystal fibres as highly nonlinear artificial Raman oscillators," Nat. Phys. **5**, 276–280 (2009).
9. M. S. Kang, N. Y. Joly, and P. St.J. Russell, "Passive mode-locking of fiber ring laser at the 337th harmonic using gigahertz acoustic core resonances," Opt. Lett. **38**, 561–563 (2013).
10. A. Butsch, M. S. Kang, T. G. Euser, J. R. Koehler, S. Rammler, R. Keding, and P. St.J. Russell, "Optomechanical nonlinearity in dual-nanoweb structure suspended inside capillary fiber," Phys. Rev. Lett. **109**, 183904 (2012).
11. A. Butsch, C. Conti, F. Biancalana, and P. St.J. Russell, "Optomechanical self-channeling of light in a suspended planar dual-nanoweb waveguide," Phys. Rev. Lett. **108**, 093903 (2012).
12. J. R. Koehler, A. Butsch, T. G. Euser, R. E. Noskov, and P. St.J. Russell, "Effects of squeezed-film damping on the optomechanical nonlinearity in dual-nanoweb fiber," Appl. Phys. Lett. **103**, 221107 (2013).
13. J. R. Koehler, A. Butsch, T. G. Euser, and P. St.J. Russell, "Frequency comb generation via optomechanical nonlinearity in evacuated dual-nanoweb fibre," in *Frontiers in Optics Conference*, (Optical Society of America, 2013), paper FTh3B.3.
14. D. Braje, L. Hollberg, and S. Diddams, "Brillouin-enhanced hyperparametric generation of an optical frequency comb in a monolithic highly nonlinear fiber cavity pumped by a cw laser," Phys. Rev. Lett. **102**, 193902 (2009).
15. P. Del'Haye, A. Schliesser, O. Arcizet, T. Wilken, R. Holzwarth, and T. J. Kippenberg, "Optical frequency comb generation from a monolithic microresonator," Nature **450**, 1214–1217 (2007).
16. M. D. Duncan, R. Mahon, J. Reintjes, and L. L. Tankersley, "Parametric Raman gain suppression in D_2 and H_2," Opt. Lett. **11**, 803–805 (1986).
17. O. E. DeLange, "Optical heterodyne detection," IEEE Spectrum **5**, 77–85 (1968).
18. C. Conti, A. Butsch, F. Biancalana, and P. St.J. Russell, "Dynamics of optomechanical spatial solitons in dual-nanoweb structures," Phys. Rev. A **86**, 013830 (2012).
19. A. N. Norris, "Flexural waves on narrow plates," J. Acoust. Soc. Am. **113**, 2647–2658 (2003).
20. L. D. Landau and E. M. Lifshitz, *Theory of Elasticity* (Butterworth-Heinemann, 1986).
21. R. W. Boyd and K. Rzazewski, "Noise initiation of stimulated Brillouin scattering," Phys. Rev. A **42**, 5514–5521 (1990).

optica

Orbital-angular-momentum-preserving helical Bloch modes in twisted photonic crystal fiber

X. M. Xi,* G. K. L. Wong, M. H. Frosz, F. Babic, G. Ahmed, X. Jiang, T. G. Euser, and P. St.J. Russell

Max Planck Institute for the Science of Light, Guenther-Scharowsky Strasse 1, 91058 Erlangen, Germany

**Corresponding author: xiaoming.xi@mpl.mpg.de*

Received 9 June 2014; revised 4 August 2014; accepted 5 August 2014 (Doc. ID 213652); published 10 September 2014

In optical fiber telecommunications, there is much current work on the use of orbital angular momentum (OAM) modes for increasing channel capacity. Here we study the properties of a helically twisted photonic crystal fiber (PCF) that preserves the chirality of OAM modes of the same order, i.e., it inhibits scattering between an order +1 mode to an order −1 mode. This is achieved by thermally inducing a helical twist in a PCF with a novel three-bladed Y-shaped core. The effect is seen for twist periods of a few millimeters or less. We develop a novel scalar theory to analyze the properties of the twisted fiber, based on a helicoidal extension to Bloch wave theory. It yields results that are in excellent agreement with full finite element simulations. Since twisted PCFs with complex core structures can be produced in long lengths from a fiber drawing tower, they are of potential interest for increasing channel capacity in optical telecommunications, but the result is also of interest to the photonic crystal community, where a new kind of guided helical Bloch mode is sure to excite interest, and among the spin–orbit coupling community.

OCIS codes: (080.4865) Optical vortices; (060.0060) Fiber optics and optical communications.

http://dx.doi.org/10.1364/OPTICA.1.000165

Fiber modes carrying orbital angular momentum (OAM) have recently received considerable attention in connection with increasing channel capacity in optical communications [1–3]. Several approaches to efficiently excite such modes have been reported [4–7] and circularly symmetric fiber designs have been used to maintain high fidelity OAM order during transmission.

In recent years there has been considerable interest in helicoidal fiber structures in connection with, for example, elimination of higher order modes in large-mode-area fibers [8], chiral fiber gratings [9], and spin–orbit coupling [10]. Helically twisted photonic crystal fiber (PCF) has been shown to support leaky OAM cladding modes that phase match to the core light at certain wavelengths, causing dips in the transmitted spectrum [11]. At wavelengths between these dips, the twisted PCF displays optical activity [12,13].

Here we report that a continuously twisted PCF with a novel three-bladed core lifts the degeneracy between left- and right-spinning modes of the same OAM order. It is, therefore, able to inhibit scattering between these modes—something that is very difficult if not impossible to achieve in circularly symmetric fibers or untwisted sixfold-symmetric hollow-core PCFs [14]. Although fibers capable of preserving linear polarization states have been available for several decades, and cylindrically birefringent PCFs have recently been demonstrated [15], this is the first report to our knowledge of a fiber that can robustly preserve the sign of the OAM.

How is it that a fiber with a threefold symmetric core can support OAM modes? We show, using a newly developed semi-analytical theory, that azimuthal Bloch waves are able to circulate unimpeded around the core, creating an OAM mode when a resonant condition is satisfied. Clockwise and anticlockwise versions of these modes become nondegenerate when the fiber is twisted, rendering them resistant to external perturbations. The analysis produces results that agree remarkably well with full-vectorial finite element modeling (FEM).

Figures 1(a) and 1(b) show a schematic of the core structure and a scanning electron micrograph of the silica–air PCF used in the experiments. It was fabricated using the stack-and-draw technique [16], the three-bladed Y-shaped core being constructed by replacing four capillaries with solid rods in the preform stack. In the drawn fiber, the hollow channels had a

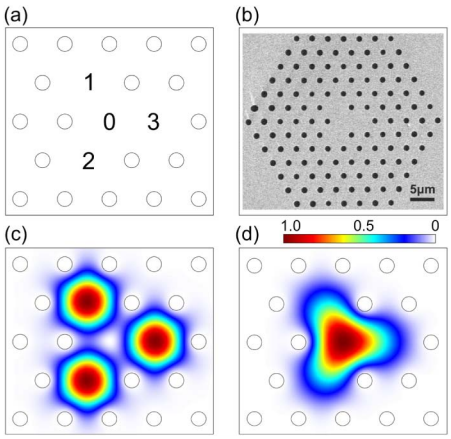

Fig. 1. (a) Schematic of the fiber core structure. (b) Scanning electron micrograph of the fiber used in the experiments. (c) Axial Poynting vector distribution of one of the ring modes at a wavelength of 800 nm and a twist rate of 1.26 rad/mm, calculated by finite element modeling in a helicoidal reference frame. (d) Axial Poynting vector distribution of the lowest order mode of the same twisted structure, which does not carry OAM.

diameter of ~1 μm and were spaced by ~3 μm; the outer diameter of the fiber was 116 μm. A continuous permanent twist (twist rate $\alpha = 2\pi/L$, where L is the helical period) was induced in the fiber by thermal postprocessing using a CO_2 laser as heat source [11,17,18].

A scalar eigenmode analysis of the untwisted fiber reveals that there are always two degenerate eigenmodes involving pairs of satellite cores (see Supplement 1). These can be superimposed to produce degenerate ring modes of OAM order $\ell = \pm 1$, in which the phase advances by $\pm 2\pi/3$ from core to core.

Full vectorial FEM solutions of Maxwell's equations in a helicoidal reference frame [13,19] show that four nondegenerate versions of these ring modes exist in the twisted fiber. All four have very similar Poynting vector distributions [Fig. 1(c) plots an individual profile for a twist rate of 1.26 rad/mm], and for twist rates larger than 0.1 rad/mm they are almost perfectly (within 3%) left- (LC, spin $s = +1$) or right- (RC, spin $s = -1$) circularly polarized. Since the phase is undefined at the center, the intensity profiles exhibit a central null.

The simulations also reveal that the lowest order mode is strongly concentrated in the central core [Fig. 1(d)] and is optically active, supporting nondegenerate LC and RC polarized modes with circular birefringence $B \sim b \times \alpha$, where α is in rad/mm and $b = 5 \times 10^{-7}$ mm/rad.

Knowing that ring modes exist in the structure allows us to construct a simple but highly instructive approximate model for the twisted system. We begin by considering a generic helical and azimuthally periodic structure, described mathematically by its dielectric constant distribution:

$$\varepsilon(\phi, r, z) = \varepsilon_0 + \varepsilon_1 \cos[3(\phi - \alpha z)] \exp[-(r-\rho)^2/w^2], \quad \textbf{(1)}$$

where ϕ is the azimuthal angle and r the radius. The factor of 3 in the argument of the cosine ensures that there are three subcores, i.e., three periods around the circle; the assumption is that the light is guided around an azimuthally periodic cylindrical shell, radial thickness w, at radius ρ from the axis.

A Bloch wave in general is written as the product of a perfectly periodic function and a phase progression at a rate given by the Bloch wavevector k_B [20]. The fields that fit into the twisted structure can be written in a modified Bloch wave form, once it is recognized that the periodic function that makes up the Bloch wave must rotate at the same rate as the structure. Ignoring the radial dependence (i.e., treating the structure as a thin helical shell of radius ρ), a suitable Ansatz is, therefore,

$$E_B(\phi, z) = e^{i(\beta_0+\gamma)z} \sum_n a_n \exp(i(k_B\rho + 3n)\phi - i3n\alpha z), \quad \textbf{(2)}$$

where $\beta_0 = k\sqrt{\varepsilon_0}$, k is the vacuum wavevector, n is the harmonic order, and γ is a small wavevector that is essentially the eigenvalue of the azimuthal Bloch modes carrying OAM (OAM Bloch modes or OBMs). This choice of Ansatz ensures that the azimuthal interference pattern created by any two of the harmonics in the summation will rotate at exactly the same rate as the fiber twist, as required.

Inserting Eqs. (1) and (2) into Maxwell's equations in cylindrical coordinates with no radial term,

$$\left(\frac{1}{\rho^2}\frac{\partial^2}{\partial\phi^2} + \frac{\partial^2}{\partial z^2} + k^2\varepsilon(\phi, z)\right) E_B = 0, \quad \textbf{(3)}$$

one then applies the standard condition that the sums of coefficients of terms with identical rates of phase progression must each independently equal zero [20]. This leads, after some algebra, to a set of homogeneous linear equations in the amplitudes a_n:

$$(2(\gamma - 3n\alpha) + (k_B + 3n/\rho)^2/\beta_0)a_n - \kappa(a_{n-1} + a_{n+1}) = 0, \quad \textbf{(4)}$$

where the coupling constant is defined by $\kappa = k^2\varepsilon_1/(2\beta_0)$ and it is assumed that $\beta_0 \gg |\gamma + 3n\alpha|$ for values of n within the required truncation range (a good approximation in our case). The truncated equation set can then be solved numerically for the dispersion relation $\gamma(k_B)$ and the eigenmodal shapes of the Bloch waves.

The OBMs are free to propagate (with a constant azimuthal group velocity component) around the circle in either direction, encountering effectively an infinite sequence of periods. The closed nature of the azimuthal path means, however, that only certain discrete values of k_B are permitted, which leads directly to the resonance condition $k_B^\ell = \ell/\rho$, where ℓ is the OAM order. Once this condition is satisfied for the lowest order harmonic, it is automatically satisfied for all the others, with the difference that the OAM order of the nth harmonic is $\ell_n = \ell + 3n$.

With this information, Eq. (4) can be rewritten as the equation set

$$\left(2(\gamma_\ell - 3n\alpha)\rho + \frac{(\ell + 3n)^2}{\beta_0 \rho}\right) a_n - \kappa\rho(a_{n-1} + a_{n+1}) = 0, \quad (5)$$

which, once solved, will establish a relationship between the OAM order ℓ and the eigenvalue γ_ℓ of the $n = 0$ harmonic. The propagation constant of the nth OBM harmonic is then $\beta_0 + \gamma_\ell - 3n\alpha$. When the OBM reaches the endface of the fiber, each nth harmonic will give rise to a free-space beam with OAM order $\ell_n = \ell + 3n$, provided its azimuthal wavevector component is not larger than k.

Figure 2 shows the wavevector diagram for the experimental parameters (wavelength 800 nm, twist period 5 mm, radius $\rho = 3$ μm) plotted over four Brillouin zones. OBMs form at $\ell = \pm 1$, as marked by the vertical dashed lines. The OBM group velocity (given by $\partial\omega/\partial\mathbf{k}$, where ω is the optical angular frequency and $\mathbf{k}$ the wavevector) points normal to the curves [20], so that the solutions for the $\ell = +1$ mode rotate toward the right, whereas those for the $\ell = -1$ mode rotate toward the left (note that the scales on the horizontal and vertical axes are not the same, so that the local gradient of the curve is exaggerated). Of crucial interest here, however, is that the propagation constants of the two modes are different, i.e., they are nondegenerate. The spectral content of each mode is also plotted in Fig. 2, showing the relative strengths of the four most significant OAM components.

For accurate comparison with experiment, and to assess the accuracy of the Bloch wave analysis, we employed a finite element model to calculate the values of propagation constant in the helicoidal reference frame. These must be transformed back into the laboratory frame using the relationship

$$\gamma_\ell = \gamma_\ell^{\mathrm{tw}} + (\ell + s)\alpha, \quad (6)$$

where $\gamma_\ell^{\mathrm{tw}}$ is the eigenvalue of the ℓth OBM in the twisted frame and $s = \pm 1$ is the spin angular momentum order [12].

The calculated effective refractive indices of the $n = 0$ harmonic of these modes at 800 nm are plotted in Fig. 3(a) as a function of twist rate. The indices of the $\ell = +1$ OBMs increase with twist rate, while those of the $\ell = -1$ OBMs fall. The index splitting is proportional to the twist rate, as may also be seen in Fig. 3(a). The results of the scalar analysis agree very well with the full numerical simulations. To obtain these fits, the following parameter values were used: $\kappa\rho = 0.078$, $\rho = 3.08$ μm, and $\beta_0\rho = 34.144$.

In addition to the large OAM splitting, there is a smaller nondegeneracy between LC- and RC-polarized modes (all four OBMs are more than 97% circularly polarized for twist rates greater than 0.1 rad/mm). FEM calculations of optical activity $B = |n_{\mathrm{OBM}}^{\mathrm{LC}} - n_{\mathrm{OBM}}^{\mathrm{RC}}|$ for each OBM are plotted against twist rate in Fig. 3(b). The Fano-like feature at ~4.6 rad/mm is caused by an anti-crossing between the $n = +1$ harmonic of the $\ell = -1$ OBM (total OAM = 0) and the non-OAM lowest order mode.

A schematic of the experimental setup is shown in Fig. 4(a). A diode laser with wavelength ~800 nm was used as a light source. A quarter-wave plate was used to select either LC- or RC-polarized light before launching into the fiber. The length of twisted PCF used in the experiment was ~5 cm with a twist rate of ~1.26 rad/mm. The first four

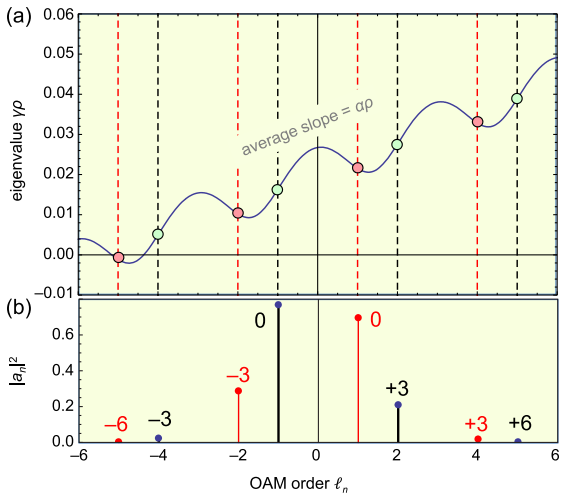

Fig. 2. (a) Illustrative wavevector diagram for an OBM, plotted over four Brillouin zones. It was obtained by solving Eq. (4) with $\beta_0\rho = 27.3$, $\alpha\rho = 0.0038$, and $\kappa\rho = 0.1$, including seven harmonics. Its shape is identical in each Brillouin zone (this ensures that every harmonic of the OBM shares the same group velocity—see text), and it is tilted at an average slope $\alpha\rho$ (this ensures that the field pattern rotates with the helical structure). (b) Normalized strengths of each harmonic. The numbers correspond to the harmonic orders n of the backward-spinning (black) and forward-spinning (red) OBMs.

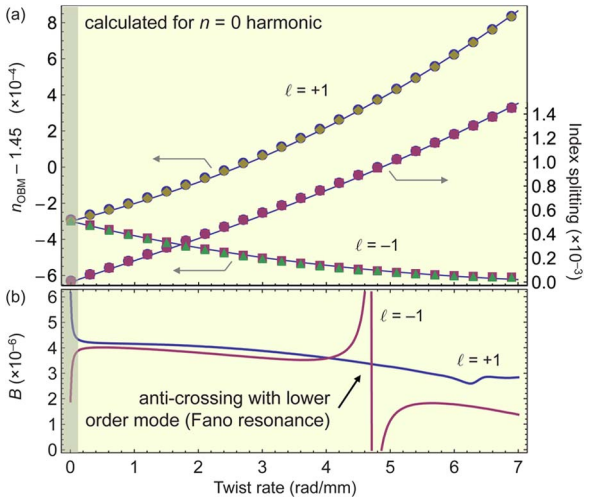

Fig. 3. (a) Comparison of FEM and analytical model. Left-hand axis: calculated refractive indices n_{OBM} at 800 nm of the $n = 0$ harmonic of the $\ell = +1$ and −1 OBMs, plotted versus twist rate. The dots correspond to full vector finite element modeling and the solid lines are solutions of the analytical OBM model. The index of the nth Bloch harmonic is $n_{\mathrm{OBM}} - 3n\alpha/k$. LC and RC polarized OBMs have refractive indices that differ by $\sim 3 \times 10^{-6}$ [see (b)]. Right-hand axis: index splitting between $\ell = +1$ and −1 OBMs, plotted versus twist rate. Within the narrow shaded region on the left, the $(s, \ell) = (-1, +1)$ and $(+1, -1)$ modes are less than 97% circularly polarized (within the accuracy of the FEM, the other two OBMs are at least 99.9% circularly polarized at zero twist rate). (b) FEM calculations of the optical activity of each OBM, plotted against twist rate (see text).

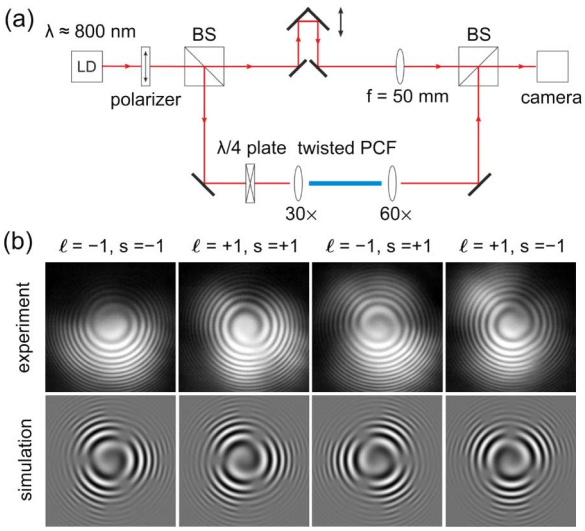

Fig. 4. (a) Schematic of the experimental setup for generating and characterizing OAM states in the twisted PCF. LD, laser diode; BS, beam splitter. (b) Experimentally recorded (top) and calculated (bottom) interference patterns created when ring modes with different combinations of spin and OAM order interfere with an expanded Gaussian reference beam.

higher order modes could be independently excited by adjusting the launching conditions. To verify that these modes do indeed carry OAM, an interferometric technique was employed, similar to that commonly used for observing the phase structure of optical vortices [21]. The output from the twisted PCF was superimposed on an expanded Gaussian reference beam and imaged onto a CCD camera. The path difference between the two arms was controlled using an adjustable delay line in the reference arm. A spiral-shaped interference pattern is expected if the light from the fiber carries OAM. This is indeed the case, single-spiral interference patterns being observed, as shown in Fig. 4(b), which confirms the principal OAM order of the modes. The handedness of the spiral indicates of the sign of ℓ. The experimental results are in excellent agreement with numerical simulations. Note that the visibility of the spiral fringes is not expected to be 100%, owing to the presence of the other Bloch harmonics (OAM order $\ell + 3n$). The visibility will be reduced further by unavoidable excitation of non-OAM fundamental modes, concentrated in the central core [Fig. 1(d)].

When the same experiment was carried out using an untwisted PCF, only concentric circles were seen in the interference pattern, no matter how the polarization and input conditions were adjusted. Although in principle it should be possible, by careful design of the OAM launch beam, to excite an isolated OBM rotating in one direction, it is likely that slight imperfections in the azimuthal periodicity will scatter light between the degenerate $\ell = \pm 1$ OBMs.

To confirm these results, ~50 m of twisted fiber with hole diameter of ~1.6 μm, hole spacing of ~5.2 μm, and pitch of 5 mm was produced in a fiber drawing tower. The fiber was wound on a spool of diameter 16 cm. Using a 1550 nm laser and a spatial light modulator (SLM) setup to synthesize a three-lobed pattern carrying OAM [14], a clear single-spiral interference pattern was observed at the fiber output for excitation of the $\ell = \pm 1$ OBMs. Preservation of the $\ell = \pm 1$ states may be further enhanced by increasing the twist rate.

Twisted PCF with a "three-bladed" core supports a new kind of guided helical Bloch mode consisting of a superposition of Bloch harmonics with OAM orders $\ell \pm 3n$, coupled together by the twist. Each of these harmonics has a different propagation constant, given by $\beta_0 + \gamma_\ell - 3n\alpha$, so that the OBM has multiple values of refractive index, just as is the case for Bloch waves in regular periodic media [21]. Two nondegenerate OBMs exist in the twisted fiber, with opposite signs of OAM. The splitting in modal index is proportional to the twist rate, and both LC and RC versions of each mode exist, with slightly different propagation constants. Full details of the twisted Bloch wave model, the implications of which we believe are quite wide-ranging, will be reported elsewhere. We note, finally, that many more higher order OBMs will exist in PCFs with rings of cores placed farther away from the axis, although a full understanding of these modes will require further detailed analysis. Since long lengths of twisted PCF can readily be produced in a fiber drawing tower, OBMs may be useful in increasing the number of channels in optical communications.

ACKNOWLEDGMENTS

Authors Xi and Wong prepared twisted PCF by postprocessing, made the optical measurements, carried out the finite element modeling, and wrote the paper. Frosz, Babic, Ahmed, and Xi (assisted by Jiang) developed special equipment for drawing long lengths of twisted PCF in the fiber pulling tower. Euser assisted with SLM-based beam synthesis. Russell conceived the experiments, developed the analytical theory, and wrote the paper.

See Supplement 1 for supporting content.

REFERENCES

1. G. Gibson, J. Courtial, M. J. Padgett, M. Vasnetsov, V. Pas'ko, S. M. Barnett, and S. Franke-Arnold, Opt. Express **12**, 5448 (2004).
2. Y. Awaji, N. Wada, Y. Toda, and T. Hayashi, in *37th European Conference and Exposition on Optical Communications*, OSA Technical Digest (CD) (Optical Society of America, 2011), paper We.10.P1.55.
3. N. Bozinovic, Y. Yue, Y. X. Ren, M. Tur, P. Kristensen, H. Huang, A. E. Willner, and S. Ramachandran, Science **340**, 1545 (2013).
4. D. McGloin, N. B. Simpson, and M. J. Padgett, Appl. Opt. **37**, 469 (1998).
5. P. Z. Dashti, F. Alhassen, and H. P. Lee, Phys. Rev. Lett. **96**, 043604 (2006).
6. Y. Yan, J. Wang, L. Zhang, J. Y. Yang, I. M. Fazal, N. Ahmed, B. Shamee, A. E. Willner, K. Birnbaum, and S. Dolinar, Opt. Lett. **36**, 4269 (2011).
7. N. Bozinovic, S. Golowich, P. Kristensen, and S. Ramachandran, Opt. Lett. **37**, 2451 (2012).
8. X. Ma, C.-H. Liu, G. Chang, and A. Galvanauskas, Opt. Express **19**, 26515 (2011).

9. V. I. Kopp, V. M. Churikov, J. Singer, N. Chao, D. Neugroschl, and A. Z. Genack, Science **305**, 74 (2004).
10. C. N. Alexeyev, A. N. Alexeyev, B. P. Lapin, G. Milione, and M. A. Yavorsky, Phys. Rev. A **88**, 063814 (2013).
11. G. K. L. Wong, M. S. Kang, H. W. Lee, F. Biancalana, C. Conti, T. Weiss, and P. St.J. Russell, Science **337**, 446 (2012).
12. X. M. Xi, T. Weiss, G. K. L. Wong, F. Biancalana, S. M. Barnett, M. J. Padgett, and P. St.J. Russell, Phys. Rev. Lett. **110**, 143903 (2013).
13. T. Weiss, G. K. L. Wong, F. Biancalana, S. M. Barnett, X. M. Xi, and P. St.J. Russell, J. Opt. Soc. Am. B **30**, 2921 (2013).
14. T. G. Euser, G. Whyte, M. Scharrer, J. S. Y. Chen, A. Abdolvand, J. Nold, C. F. Kaminski, and P. St.J. Russell, Opt. Express **16**, 17972 (2008).
15. T. G. Euser, M. A. Schmidt, N. Y. Joly, C. Gabriel, C. Marquardt, L. Y. Zang, M. Förtsch, P. Banzer, A. Brenn, D. Elser, M. Scharrer, G. Leuchs, and P. St.J. Russell, J. Opt. Soc. Am. B **28**, 193 (2011).
16. P. St.J. Russell, J. Lightwave Technol. **24**, 4729 (2006).
17. S. T. Oh, K. R. Lee, U. C. Paek, and Y. J. Chung, Opt. Lett. **29**, 1464 (2004).
18. W. Shin, Y. L. Lee, B. A. Yu, Y. C. Noh, and K. Oh, Opt. Commun. **282**, 3456 (2009).
19. A. Nicolet, F. Zolla, Y. O. Agha, and S. Guenneau, COMPEL **27**, 806 (2008).
20. P. St.J. Russell, Appl. Phys. B **39**, 231 (1986).
21. S. Ramachandran and P. Kristensen, J. Nanophoton. **2**, 455 (2013).

optica

Noninvasive nonlinear focusing and imaging through strongly scattering turbid layers

ORI KATZ,[1] ERAN SMALL,[1] YEFENG GUAN,[1,2] AND YARON SILBERBERG[1,*]

[1]Department of Physics of Complex Systems, Weizmann Institute of Science, Rehovot, Israel

[2]State Key Laboratory of Optoelectronic Materials and Technologies, Sun Yat-sen University, Guangzhou 510275, China

*Corresponding author: yaron.silberberg@weizmann.ac.il

Received 13 May 2014; revised 7 July 2014; accepted 7 July 2014 (Doc. ID 211998); published 11 September 2014

Diffraction-limited imaging through complex scattering media is a long-sought-after goal with important applications in biomedical research. In recent years, high-resolution wavefront shaping has emerged as a powerful approach to generate a sharp focus through highly scattering, visually opaque samples. However, it requires a localized feedback signal from the target point of interest, which necessitates an invasive procedure in all-optical techniques. Here, we show that by exploiting optical nonlinearities, a diffraction-limited focus can be formed inside or through a complex sample, even when the feedback signal is not localized. We prove our approach theoretically and numerically, and experimentally demonstrate it with a two-photon fluorescence signal through highly scattering biological samples. We use the formed focus to perform two-photon microscopy through highly scattering, visually opaque layers.

OCIS codes: (030.6140) Speckle; (180.0180) Microscopy; (110.7050) Turbid media; (290.4210) Multiple scattering; (180.4315) Nonlinear microscopy.

http://dx.doi.org/10.1364/OPTICA.1.000170

The inherent inhomogeneity of complex samples such as biological tissues induces light scattering, which limits the resolution of light focusing and poses a major hurdle to deep-tissue microscopy [1]. Adaptive optics techniques are very effective in correcting the aberrations induced by sample index mismatch and thin tissues [2–4]. However, until recently, these techniques were considered impractical for turbid and thick multiply scattering samples, where no unscattered, "ballistic" light components remain and the propagating light is diffused to form complex speckle patterns with no simple relation to the incident wavefront [5,6]. This conception changed after the 2007 work of Vellekoop and Mosk [7,8], where it was shown that high-resolution wavefront shaping can be used to create a high-intensity, diffraction-limited focus deep in the diffusive light propagation regime where essentially no ballistic photons are present, such as through a thick layer of white paint or the shell of an egg.

Diffraction-limited focusing by wavefront shaping is attained even when the number of degrees of control is much smaller than the number of scattered modes, i.e., with a correction that is far from being perfect [7–14]. Indeed, as a result, only a small fraction of the initial light energy is actually focused by this technique, but the high-contrast focus can still be very valuable for many applications, and in particular for nonlinear microscopy. The main limitation of wavefront-shaping techniques is that a direct feedback from the target point is required, either by directly observing it with a camera [8–14], or by embedding a "guide star" at the target position [12,13]. Both these requirements are invasive and are thus incompatible with most imaging applications. Very recently, wavefront shaping was combined with acoustics to obtain the feedback signal noninvasively [15–20], though with focal dimensions exceeding the optical wavelength.

Here, we show that nonlinear optical feedback, such as the one widely used for two-photon microscopy, can be used in epidetection geometry to obtain diffraction-limited focusing through strongly scattering turbid samples. Furthermore, we demonstrate that this focus can be used for nonlinear imaging (here demonstrated in two-photon microscopy) in reflection mode in a totally noninvasive manner. We show that one can focus an ultrashort pulse on an extended object hidden behind a scattering medium by optimizing the *total nonlinear signal* that is produced in the specimen. This technique should be adaptable to most nonlinear microscopy techniques, such as two- and three-photon fluorescence (2PF, 3PF), second- and third-harmonic generation (SHG, THG), four-wave mixing, and coherent anti-Stokes Raman scattering (CARS). We show

that the optimization of a nonlinear signal of sufficient order results in a single, tightly focused spot, even when the optimized signal is collected from a very large area on the object, specifically by epidetection through the same scattering medium. Such a result cannot be obtained by optimizing a linear signal such as total intensity of fluorescence or reflected intensity. Nonlinear optimization has been shown before to correct also for the temporal distortions of ultrashort pulses propagating through scattering media [21]; thus, the generated focus is also short in temporal duration and hence intense. Furthermore, by raster-scanning this focal spot, exploiting the so-called memory effect [22,23], an image could be collected from the vicinity of the optimized focus [11,12,24]. We believe that these results form an important step toward optical focusing deep inside scattering tissues and imaging through turbid layers.

Figure 1(a) shows the setup we have used for demonstrating our technique with two-photon excited fluorescence microscopy, one of the most widely used nonlinear imaging modalities in neuroscience [25]. Pulses ~100 fs long from a Ti:sapphire laser illuminate a fluorescent object after passing through a phase-only spatial light modulator. As a first experiment, an optical diffuser was used to introduce scattering and a thin, two-photon homogeneous fluorescence screen served as the distributed object. The total excited fluorescence signal is epidetected through the scattering medium with a single sensitive integrating detector. The resulting spatial distribution of the two-photon excited fluorescence on the fluorescent screen target is inspected by a camera placed on the other side of the medium, *but its image is not used for the wavefront shaping optimization* (see Fig. S1 in Supplement 1), an important advantage over the previous works on nonlinear signal optimization [21,26]. Figure 1(b) shows the speckle, spatially scattered fluorescence pattern recorded from the screen prior to optimization. We then used an optimization procedure based on a genetic algorithm [27] to find the SLM phase pattern that maximizes the total two-photon fluorescence signal measured in epidetection. Figure 1(c) shows the resulting optimized focus point on the screen. The progress of the total detected signal during the optimization process is shown in Fig. 1(d) and in Media S1. As can be observed in Fig. 1(c), by optimizing the total backward-scattered 2PF signal collected via the illumination optics with a large-area detector, the excitation pulses focused to a single diffraction-limited focal spot on the object, *though its location is not controlled or predetermined.* Note that the total enhancement in the signal is rather small (about 50% over its initial value), although the focused intensity is enhanced by a considerably larger factor. In the simple case of a planar fluorescent object and where no temporal pulse distortions are present, the total signal enhancement factor is expected to be $\sim N_{\mathrm{SLM}}^{N}/N_{\mathrm{speckles}}$, where N_{SLM} is the number of controlled SLM pixels, N is the order of the nonlinearity ($N = 2$ for 2PF), and N_{speckles} is the number of speckle grains that initially illuminate the fluorescence object and that contribute to the initial signal [See Eq. (S1) in Supplement 1].

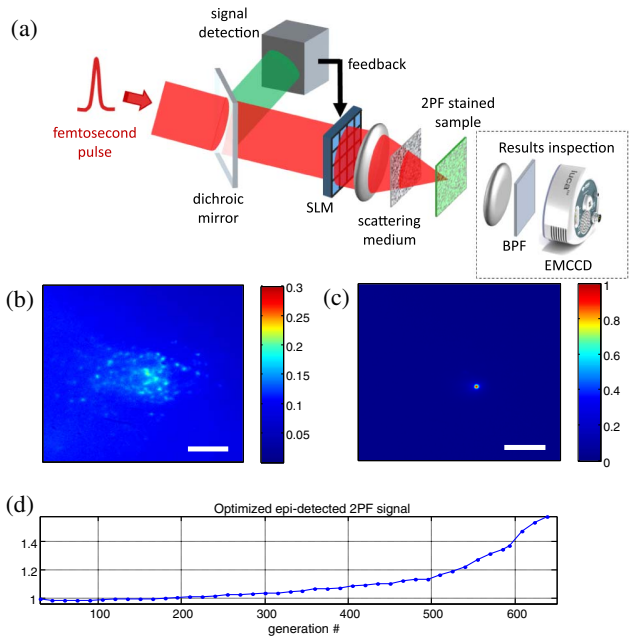

Fig. 1. Noninvasive focusing through scattering samples. (a) Experimental system. 100 fs pulses are sent via a spatial light modulator (SLM) and focused through a diffuser on a two-photon fluorescent screen. The fluorescence is collected via the same optics and used as a signal for an optimization algorithm. An auxiliary imaging system records the speckle image on the screen. (b) Speckle pattern recorded from the 2PF screen before optimization. (c) Optimized focus via maximization of total epi 2PF. (d) Progress of the optimization process. Scale bars, 100 μm.

Once a sharp spot is formed, it may be raster-scanned to obtain a microscopic image of the fluorescent object hidden behind the scattering layer [11,12]. The image is collected point-by-point, in a similar manner to image formation in standard two-photon microscopy, by scanning the focal point through the sample; for example, by using the same SLM as a scanning device [12], although fast scanning mirrors can be utilized for increased speed. The field of view (FOV) of this imaging technique is limited by the range where the single SLM wavefront correction is effective, which is dictated in the diffusive light propagation regime by the optical memory effect [22–24]. This range is analogous to the isoplanatic patch size in turbulent media [28]. In a diffusive medium of thickness L, the HWHM angular FOV of the memory effect can be estimated by $\Delta\theta_{\mathrm{FOV}} \approx \lambda/\pi L$ [22]. As a result, similar to other memory-effect-based techniques [11,12,24] a large FOV is available only when the target distance from the diffusive layer is considerably larger than the effective layer thickness, as is the case when imaging in an eggshell geometry or "around corners" in reflection geometry [24]. Wide-field imaging in the diffusive regime inside thick, multiply scattering tissues (i.e., at depths larger than the transport mean free path) presents a challenge. Note that, for the scanning to be effective, it is crucial to conjugate the correcting SLM and scanning optics plane with the distorting scattering layer plane [11,12,24].

An experimental demonstration of focusing and raster imaging using this technique is presented in Fig. 2. In this experiment, the fluorescent screen is replaced by a cluster of two-photon fluorescence Fluorescein crystallites on a glass cover slip, placed at a distance of ~2 mm behind the optical diffuser (Newport 10° light-shaping diffuser). After the same optimization procedure, the formed focus (whose exact position on

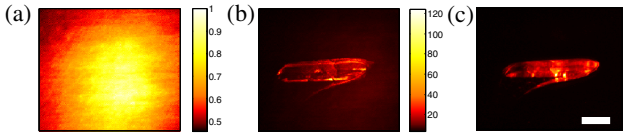

Fig. 2. Two-photon imaging through an optical diffuser using the memory effect. (a) Standard 2PF microscopy image of an object (cluster of Coumarin 307 crystallites) as observed through a diffuser. (b) After optimizing the total 2PF signal, a focus is formed. A bright and crisp image of the two-photon object is obtained by collecting the signal in epigeometry, while the focus is raster-scanned by adding linear phase ramps to the SLM phase pattern. (c) Transmission microscope image of the same object without the scattering medium is presented for comparison. Scale bar, 100 μm.

the object is unknown and depends on the initial conditions and fluorescent structure), was scanned by adding linear phase ramps on top of the SLM correction phase pattern. The image that was obtained with the optimized focus [Fig. 2(b)] is not just of higher resolution and contrast when compared to the blurred standard two-photon microscopy image, but is also approximately an order of magnitude brighter than an image obtained without optimization [Fig. 2(a)]. The true image of the object, with the diffuser removed, is shown in Fig. 2(c).

The experimental results show that optimizing a nonlinear signal is a promising path to forming a diffraction-limited spot on a planar object in the diffusive light propagation regime, where no ballistic unscattered light is present. This result is related to recent results in adaptive optics, where two-photon optimization is used to refocus light at depths of an order of one transport mean free path [29], where an initial focus is present in the unoptimized field, and to nonlinear photoacoustic focus formation on a planar target [30]. However, as we show below, careful analysis of the focus formation process shows that in the general case of a three-dimensional fluorescent object located in the diffusive regime, *a higher order* ($N > 2$) *nonlinearity is required to assure focusing to a single speckle grain.* For a linear signal, as in standard fluorescence imaging, energy conservation dictates that the total integrated signal would not change when the energy is focused tightly or spread over a large area if the fluorophores are distributed homogeneously in the specimen. In contrast, an integrated *nonlinear* signal does not obey such a conservation law, and the total integrated signal could be larger the tighter the beam is focused, depending on the order of nonlinearity. Simple geometrical considerations can help to determine the range where this mechanism could be applied.

To obtain some insight, consider first a simple planar nonlinear object producing an Nth-order nonlinear signal, and assume that the incoming beam is scattered to a number of speckles N_{speckles} on the object. The total generated signal power would be proportional to

$$P_{\text{tot}} \propto N_{\text{speckles}} \cdot \left(\frac{P_{\text{laser}}}{N_{\text{speckles}}}\right)^N = P_{\text{laser}}^N \left(\frac{1}{N_{\text{speckles}}}\right)^{N-1}, \quad \textbf{(1)}$$

where P_{laser} is the total beam power on the sample. Clearly, for a linear signal (i.e., $N = 1$) there is no advantage in reducing the number of speckles since the total signal is independent of the size of the beam (i.e., N_{speckles}), as we have argued above [Eq. (1)]. However, the situation is different in the case of a nonlinear signal ($N > 1$), where the total signal power would maximize for a beam where N_{speckles} is minimized, i.e., for the most focused beam ($N_{\text{speckles}} = 1$).

The fact that our samples (either the uniform 2PF screen used in Fig. 1 or the sample used in Fig. 2) were thin was important for this process to work. To understand the issue with a thick nonlinear medium, it is instructive to consider a Gaussian beam focused to a waist w_0 inside such a thick medium, producing an Nth-order nonlinear incoherent signal, such as N-photon fluorescence. In that case, for $N > 1$ nonlinearity, the total nonlinear signal can be approximated by the signal generated inside a cylinder of volume V along the beam confocal parameter $b = 4\pi\omega_0^2/\lambda$. Under this assumption, the total generated (or detected) signal would be proportional to

$$P_{\text{tot}} \propto V \cdot I_{\text{laser}}^N \propto (b \cdot \pi w_0^2) \cdot \left(\frac{P_{\text{laser}}}{w_0^2}\right)^N \propto w_0^4 \cdot \left(\frac{P_{\text{laser}}}{w_0^2}\right)^N \propto \frac{P_{\text{laser}}^N}{w_0^{2(N-2)}}. \quad \textbf{(2)}$$

An exact solution for focused Gaussian–Lorentzian or diffraction-limited beam can be found in Xu and Webb [31].

It is evident that for $N = 2$, e.g., 2PF, the total signal is constant, independent of w_0. Intuitively, the effect of the increased intensity by tighter focusing is compensated by the shrinking effective excitation volume [31]. Hence, optimization in a thick, homogenous second-order medium is not possible. Only for $N > 2$, i.e., only for a nonlinearity which is higher than a second order such as the one used in 3PF microscopy [32], does the signal increase by focusing. This should be contrasted with the result of Eq. (1) for a planar nonlinear object, where any nonlinearity of $N > 1$ was sufficient to ensure focusing down to a single speckle grain. We note that this fact is closely related to harmonic generation in bulk crystals and the determination of optimal focusing [33].

To complement this naïve basic analysis, we performed exact numerical simulations that produce results which are on par with this conclusion. Figure 3 shows results of simulations emulating the actual process: the speckle field was calculated by applying a random phase structure, and the nonlinear signal generated by the speckle field was integrated and used as feedback for optimization of wavefront correction using the same genetic algorithm. Note that in these simulations, as in our experiments, the field is first scattered by a thin layer and then propagated through free space to the nonlinear medium, which was homogeneous and nonscattering. The simulation results, which are averaged over 10 realizations of disorder for each case, show that 2PF does not lead to optimized focusing in thick three-dimensional objects, while 3PF worked well in all geometries.

Nonlinear feedback signal has been utilized previously for temporal compression; as has been shown in previous works [21,26,34], nonlinear optimization not only focuses the pulse in space, but also *compresses the pulse in time*, compensating for

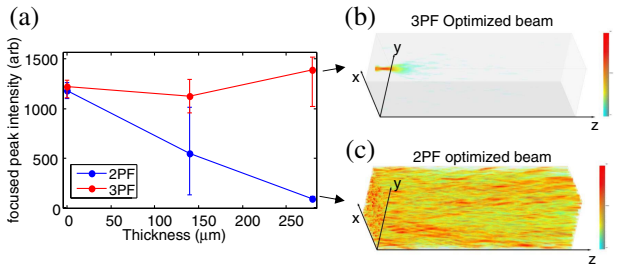

Fig. 3. Results of simulations of optimization of 2PF and 3PF signals. A speckle field is simulated, and the calculated total nonlinear signal is then used as feedback in a genetic algorithm for wavefront shaping. (a) shows the resulting peak enhancement of such a simulation with three different thicknesses of the nonlinear medium. In thin media, both nonlinearities led to convergence and significant enhancement of the peak intensity. In thick media, however, only 3PF led to focusing and peak enhancement (b). Two-photon effects did not converge and left the speckle field practically unchanged (c).

temporal distortions and resulting in a spatiotemporal focus. We expect, therefore, that the optimized focal points here are also temporally short, although we have not verified this by measurements.

Note that the analysis and simulations assumed a homogeneous distribution of the nonlinear medium, which is of course far from being realistic and actually represents a worst-case scenario. In actual samples, where the nonlinear agent is distributed unevenly in the specimen, it might well be that the algorithm would perform better, as a concentrated region of high nonlinearity would serve as "guide stars" and help the optimization process. As an example, Fig. 4 shows focusing, through a 1 mm slice of brain tissue, on a nonlinear object placed ~300 μm behind it. The algorithm finds an optimal focus which is, not surprisingly, located on a spot of highly concentrated fluorophore. Interestingly, we have observed that as the signal of one bright spot eventually fades due to photobleaching, the search algorithm will switch to another focal spot on another crystallite, bleaching it as well, and so on. We have confirmed in numerical simulations that two-photon nonlinearity is sufficient in many such cases where the volumetric nonlinear object is sparsely tagged or whenever there is even a weak ballistic unscattered component in the beam, on par with the recent experimental results of Tang *et al.* with 2PF [29], and Fiolka *et al.* with linear time-gated signal optimization [35]. An important advantage of our

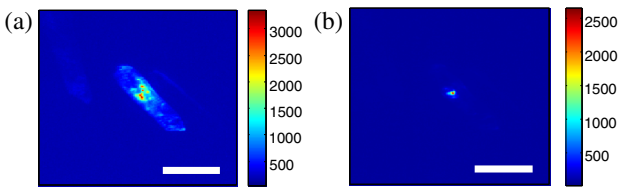

Fig. 4. Experimental focusing through a 1 mm thick brain tissue. An object (Coumarin 307 crystallites) is placed behind the fixed brain slice. (a) Image of the 2PF as measured by the inspection camera prior to the optimization. (b) After optimizing, the total 2PF measured through the scattering layer leads to a focal point which is actually localized on one of the strongest fluorescing crystallites. Scale bars, 100 μm.

nonlinearity-based technique over linear-signal-based approaches employing either time-gated detection [35], ultrasonic tagging [15], or photoacoustics [20] is that, given a sufficient order of nonlinearity and measurement signal-to-noise, the generation of a single diffraction-limited focus is guaranteed. The main drawback of the technique is that the exact position of the focus is undetermined.

It is important to note that in the experiment of Fig. 4, as the target object was placed a relatively short distance from the scattering tissue compared to the tissue thickness, it was not possible to scan the focused spot over a range of more than a few micrometers, in accordance with the limitations of the memory effect.

An important practical hurdle to generating the focus deep inside volumetric fluorescent samples such as weakly tagged biological tissues is the large nonlinear background signal generated near the surface of such samples [36]. Although the global maximum for the optimized signal is obtained for the most tightly focused beam [Eq. (2)], the measurement of the small total signal enhancement [Eq. (S1) in Supplement 1] on top of the large background is expected to be a challenge in cases where the target object is not strongly fluorescing. This hurdle may be overcome by limiting the detection volume via ultrasonic tagging [15–17], photoacoustics [30], or spatial filtering [36]. The above analysis and discussion assumed an incoherent nonlinear process, in particular two- and three-photon fluorescence. In coherent processes, such as second- and third-harmonic generation and CARS, phase-matching considerations could have a significant effect. We will not discuss them here, but generally we expect the above conclusions to be valid in cases where the phase-matching length is not large.

FUNDING INFORMATION

European Research Council (ERC) (QUAMI); Israel Science Foundation - ICORE (Circle of Light); Israel Nanotechnology Initiative (INI) (FTA).

See Supplement 1 for supporting content.

REFERENCES

1. V. Ntziachristos, Nat. Methods **7**, 603 (2010).
2. R. K. Tyson, *Principles of Adaptive Optics*, 2nd ed. (Academic, 1998).
3. Nature Photonics Technology Focus: Adaptive optics. Nat. Photonics **5**, 15 (2011).
4. M. J. Booth, D. Débarre, and A. Jesach, Opt. Photon. News **23**(1), 22 (2012).
5. P. Sebbah, *Waves and Imaging through Complex Media* (Kluwer, 2001).
6. J. W. Goodman, *Speckle Phenomena in Optics: Theory and Applications* (Roberts and Company, 2007).
7. A. P. Mosk, A. Lagendijk, G. Lerosey, and M. Fink, Nat. Photonics **6**, 283 (2012).
8. I. M. Vellekoop and A. P. Mosk, Opt. Lett. **32**, 2309 (2007).
9. I. M. Vellekoop, A. Lagendijk, and A. P. Mosk, Nat. Photonics **4**, 320 (2010).
10. E. G. van Putten, D. Akbulut, J. Bertolotti, W. L. Vos, A. Lagendijk, and A. P. Mosk, Phys. Rev. Lett. **106**, 193905 (2011).
11. I. M. Vellekoop and C. M. Aegerter, Opt. Lett. **35**, 1245 (2010).

12. C.-L. Hsieh, Y. Pu, R. Grange, G. Laporte, and D. Psaltis, Opt. Express **18**, 20723 (2010).
13. I. M. Vellekoop, E. G. van Putten, A. Lagendijk, and A. P. Mosk, Opt. Express **16**, 67 (2008).
14. S. M. Popoff, G. Lerosey, R. Carminati, M. Fink, A. C. Boccara, and S. Gigan, Phys. Rev. Lett. **104**, 100601 (2010).
15. X. Xu, H. Liu, and L. V. Wang, Nat. Photonics **5**, 154 (2011).
16. K. Si, R. Fiolka, and M. Cui, Nat. Photonics **6**, 657 (2012).
17. Y. M. Wang, B. Judkewitz, C. A. DiMarzio, and C. Yang, Nat. Commun. **3**, 928 (2012).
18. F. Kong, R. H. Silverman, L. Liu, P. V. Chitnis, K. K. Lee, and Y. C. Chen, Opt. Lett. **36**, 2053 (2011).
19. B. Judkewitz, Y. M. Wang, R. Horstmeyer, A. Mathy, and C. Yang, Nat. Photonics **7**, 300 (2013).
20. T. Chaigne, O. Katz, A. C. Boccara, M. Fink, E. Bossy, and S. Gigan, Nat. Photonics **8**, 58 (2014).
21. O. Katz, E. Small, Y. Bromberg, and Y. Silberberg, Nat. Photonics **5**, 372 (2011).
22. I. Freund, M. Rosenbluh, and S. Feng, Phys. Rev. Lett. **61**, 2328 (1988).
23. S. Feng, C. Kane, P. A. Lee, and D. A. Stone, Phys. Rev. Lett. **61**, 834 (1988).
24. O. Katz, E. Small, and Y. Silberberg, Nat. Photonics **6**, 549 (2012).
25. B. A. Wilt, L. D. Burns, E. T. W. Ho, K. K. Ghosh, E. A. Mukamel, and M. J. Schnitzer, Annu. Rev. Neurosci. **32**, 435 (2009).
26. J. Aulbach, B. Gjonaj, P. Johnson, and A. Lagendijk, Opt. Express **20**, 29237 (2012).
27. D. B. Conkey, A. N. Brown, A. M. Caravaca-Aguirre, and R. Piestun, Opt. Express **20**, 4840 (2012).
28. D. L. Fried, J. Opt. Soc. Am. **72**, 52 (1982).
29. J. Tang, R. N. Germain, and M. Cui, Proc. Natl. Acad. Sci. USA **109**, 8434 (2012).
30. P. Lai, L. Wang, J. W. Tay, and L. V. Wang, "Nonlinear photoacoustic wavefront shaping (PAWS) for single speckle-grain optical focusing in scattering media," arXiv:1402.0816 (2014).
31. C. Xu and W. W. Webb, in *Topics in Fluorescence Spectroscopy* (Springer, 2002), pp. 477–480.
32. N. G. Horton, K. Wang, D. Kobat, C. Clark, F. Wise, C. Schaffer, and C. Xu, Nat. Photonics **7**, 205 (2013).
33. G. D. Boyd and D. A. Kleinman, J. Appl. Phys. **39**, 3597 (1968).
34. D. Yelin, D. Meshulach, and Y. Silberberg, Opt. Lett. **22**, 1793 (1997).
35. R. Fiolka and M. Cui, Opt. Express **20**, 16532 (2012).
36. P. Theer and W. Denk, J. Opt. Soc. Am. A **23**, 3139 (2006).

Research Article Vol. 1, No. 3 / September 2014 / Optica 175

High-resolution and broadband all-fiber spectrometers

Brandon Redding,[1] Mansoor Alam,[2] Martin Seifert,[2] and Hui Cao[1,*]

[1]Department of Applied Physics, Yale University, New Haven, Connecticut 06520, USA

[2]Nufern, East Granby, Connecticut 06026, USA

*Corresponding author: hui.cao@yale.edu

Received 10 April 2014; revised 23 July 2014; accepted 20 August 2014 (Doc. ID 209611); published 11 September 2014

The development of optical fibers has revolutionized telecommunications by enabling long-distance broadband transmission with minimal loss. In turn, the ubiquity of high-quality, low-cost fibers has enabled a number of additional applications, including fiber sensors, fiber lasers, and imaging fiber bundles. Recently, we showed that a multimode optical fiber can also function as a spectrometer by measuring the wavelength-dependent speckle pattern formed by interference between the guided modes. Here, we reach a record resolution of 1 pm at a wavelength of 1500 nm using a 100 m long multimode fiber, outperforming the state-of-the-art grating spectrometers. We also achieved broadband operation with a 4 cm long fiber, covering 400–750 nm with 1 nm resolution. The fiber spectrometer, consisting of the fiber, which can be coiled to a small volume, and a monochrome camera that records the speckle pattern, is compact, lightweight, and low cost while providing ultrahigh resolution, broad bandwidth, and low loss.

OCIS codes: (060.2370) Fiber optics sensors; (120.6200) Spectrometers and spectroscopic instrumentation; (300.6190) Spectrometers.

http://dx.doi.org/10.1364/OPTICA.1.000175

1. INTRODUCTION

Spectrometers are widely used tools in chemical and biological sensing, material analysis, and light source characterization. Traditional spectrometers use a grating to disperse light, and the spectral resolution scales with the optical pathlength from the grating to the detectors, imposing a tradeoff between device size and resolution. In recent years the development of "miniature" spectrometers has enabled a host of new applications due to their reduced cost and portability. However, they still rely on grating dispersion, and thus the spectral resolution is lower than the large bench-top spectrometers. In order to develop a compact spectrometer without sacrificing resolution, we turn to a multimode fiber (MMF), where a long pathlength is easily achieved in a small footprint by coiling the fiber. Of course, replacing the grating with a MMF also requires the spectrometer to operate according to a different paradigm.

In a grating-based spectrometer, light from different spectral bands is mapped to different spatial positions. However, this one-to-one spectral-to-spatial mapping is not strictly required, and spectrometers have also been built using dispersive elements with more complex spectral-to-spatial mapping. In these implementations, different spectral bands are mapped to different spatial intensity patterns. These intensity patterns function as fingerprints identifying the spectral content of an unknown probe. This approach has enabled spectrometers based on disordered photonic crystals [1] and random scattering media [2,3], which have the advantage of being very compact. Multiple scattering of light in a disordered structure increases the optical pathlength by folding the paths in a confined geometry, enhancing the spectral decorrelation of transmitted speckle. The resulting high spatial–spectral diversity enabled the development of a random spectrometer on a silicon chip, where the footprint is especially limited [3]. However, light transmission through a strongly scattering medium is usually low, limiting the sensitivity to weak signals. A photonic bandgap fiber bundle has also been used as a spectrometer [4]. To increase the intensity throughput, the transmission bands of the constituent fibers are broad and

2334-2536/14/030175-06$15/0$15.00

overlapping, which limits the wavelength resolution to ~10 nm [4].

In this work, we show that using a single MMF as the dispersive element overcomes many of these limitations. In a MMF, interference among the guided modes creates wavelength-dependent speckle patterns, providing the required spectral-to-spatial mapping [5,6]. The spectral resolution is then determined by the minimal change in wavelength that generates an uncorrelated speckle pattern. In a MMF, the spectral correlation width of the speckle scales inversely with the length of the fiber [7–9]. Since optical fibers have been optimized for long-distance transmission with minimal loss, long fibers can be used to provide fine resolution without sacrificing sensitivity. In addition, the fiber can be coiled into a small footprint, enabling a compact, high-resolution, low-loss spectrometer.

Large-core optical fibers can easily support hundreds to thousands of spatial modes. The speckle pattern produced by interference between these modes is determined by their relative amplitude and phase. For monochromatic input light, the electric field at the end of a fiber of length L can be written as the sum of the contribution from each guided mode:

$$\mathbf{E}(r,\theta,\lambda,L) = \sum_m A_m \boldsymbol{\psi}_{\mathbf{m}}(r,\theta,\lambda) \times \exp[-i(\beta_m(\lambda)L - \omega t + \varphi_m)], \quad (1)$$

where A_m and ϕ_m are the amplitude and the initial phase of the mth mode, which has spatial profile $\boldsymbol{\psi}_{\mathbf{m}}$ and propagation constant β_m. A shift of the input wavelength λ modifies the propagation constant, causing the guided modes to accumulate different phase delays, $\beta_m(\lambda)L$, as they travel along the fiber and thereby changing the speckle pattern. The sensitivity of the speckle pattern to a change in wavelength therefore increases with L. The spectral resolution of the fiber spectrometer, given by the minimum wavelength shift that produces an uncorrelated speckle pattern, thus scales inversely with the length of the fiber [5].

We note that Eq. (1) assumes an ideal multimode optical fiber in which the modal distribution (i.e., the coefficients A_m) remains fixed for the length of the fiber. Experimentally, small imperfections in the fiber or bending/twisting of the fiber introduces mode coupling which can affect the spectral resolution of the fiber spectrometer. In the limit of strong mode coupling, the spectral resolution scales as $L^{-1/2}$ instead of L^{-1}. However, the mode coupling length of standard glass core fibers is much longer than the lengths of the fibers used for the spectrometers [10]. Moreover, we observed that the spectral correlation width scaled linearly with the fiber length up to 100 m, confirming that mode coupling has a negligible effect on the spectral resolution of the fiber spectrometers.

2. HIGH-RESOLUTION FIBER SPECTROMETER

In order to push the resolution limit of the fiber spectrometer, we selected a 100 m long, step-index MMF (core diameter = 105 μm, NA = 0.22). The fiber supported ~1000 modes at $\lambda = 1500$ nm [11]. The 100 m fiber was coiled on a 3" diameter spool and fixed by resin for mechanical stability. A photograph of the coiled fiber, placed on top of an insulating block, is shown in Fig. 1(a). A monochrome camera (Xenics Xeva 1.7–320) was used to record the far-field speckle patterns. In general, the speckle from a MMF depends not only on the input wavelength, but also on the polarization and spatial profile of the input light. To ensure that the same wavelength always produced identical speckle pattern, the probe light was coupled through a polarization-maintaining single-mode fiber (SMF) to the MMF. The SMF was fused to the MMF, as seen in Fig. 1(b), to ensure the same combination of guided modes was excited in the MMF every time.

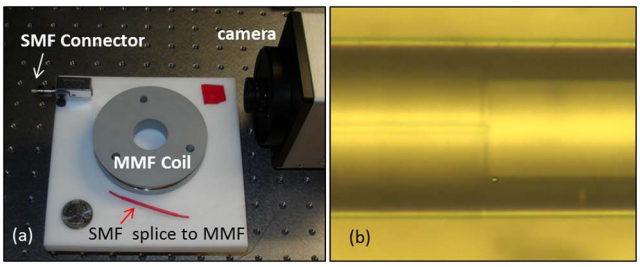

Fig. 1. (a) Photograph of the fiber spectrometer. Probe light is coupled to the polarization-maintaining SMF which is fused to the MMF. The light then excites a superposition of guided modes in the MMF, which travel 100 meters around the 3" coil. The output end of the fiber was secured to an insulating block placed in front of a monochrome camera, which records the wavelength-dependent speckle pattern in the far field. (b) Optical microscope image of a SMF spliced to a MMF, confirming that the SMF core was fused to the MMF core to minimize the coupling loss. By coupling the probe light through the polarization-maintaining SMF to the MMF, we ensure that the same combination of guided modes is always excited in the MMF.

A representative speckle pattern, recorded at an input wavelength of $\lambda = 1500$ nm, is shown in Fig. 2(a). Due to the long length of the fiber, a tiny change in wavelength was sufficient to produce uncorrelated speckle patterns. To quantify this sensitivity, we calculated the spectral correlation function of the speckle intensity, $C(\Delta\lambda,x) = \langle I(\lambda,x)I(\lambda+\Delta\lambda,x)\rangle / [\langle I(\lambda,x)\rangle \langle I(\lambda+\Delta\lambda,x)\rangle] - 1$, where $I(\lambda,x)$ is the intensity at a position x for input wavelength λ, and $\langle\ldots\rangle$ represents the average

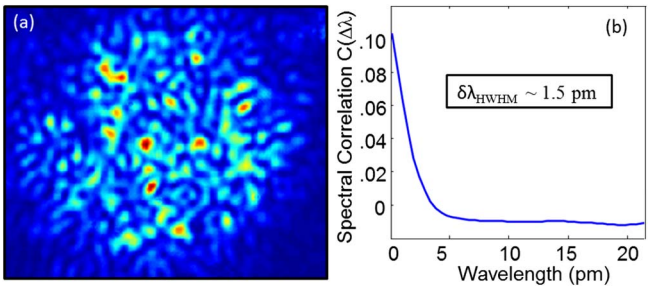

Fig. 2. (a) Speckle pattern recorded at $\lambda = 1500$ nm from the end of a 100 m long step-index MMF (core diameter = 105 μm, NA = 0.22). From the number of speckles, we estimated that approximately 400 spatial modes were excited in the MMF. (b) Measured spectral correlation function of the speckle pattern, showing a half-width at half-maximum (HWHM) of 1.5 pm. The small spectral correlation width enables high resolution.

over λ. We then averaged $C(\Delta\lambda, x)$ over each position x in the speckle pattern. The correlation function is plotted in Fig. 2(b). The correlation width, defined as the change in wavelength required to reduce the correlation by half, was found to be merely 1.5 pm. This value provides an estimate for the resolution of the fiber spectrometer, although the actual resolution also depends on the noise of the measurements and the reconstruction algorithm.

In order to use the 100 m MMF as a spectrometer, we first calibrated its transmission matrix, which characterizes the spectral-to-spatial mapping properties of the fiber. The transmission matrix, T, was defined as $I = T \cdot S$, where I is a vector describing the discretized speckle pattern and S is the discretized input spectra [6]. Each column in T represents the speckle pattern produced by one spectral channel. The calibration procedure consisted of recording the speckle pattern for each spectral channel in S, thereby measuring T one column at a time. For the 100 m fiber spectrometer, we calibrated a transmission matrix consisting of 200 spectral channels from $\lambda = 1500.0$ nm to $\lambda = 1500.1$ nm in steps of 0.5 pm using a tunable laser (Agilent 81600B). The speckle pattern in Fig. 2(a) contains approximately 400 speckles, indicating that ~400 spatial modes were excited in the MMF. We thus selected 400 independent spatial channels for the calibration of T. After calibration, we recorded the speckle pattern for various probe wavelengths and attempted to reconstruct the input spectra. The reconstruction was performed using a combination of matrix pseudo-inversion and nonlinear optimization [6]. Figure 3(a) shows the reconstructed spectra for a series of narrow spectral lines across the operating bandwidth. The linewidth is ~1 pm and the signal-to-noise ratio (peak-to-background ratio) is over 1000. We then tested the spectral resolution of the 100 m fiber spectrometer by resolving two closely spaced spectral lines. In order to synthesize such a test probe spectrum, we separately recorded speckle patterns at two closely spaced probe wavelengths and then added these speckle patterns in intensity. We then attempted to reconstruct the spectra from the synthesized speckle pattern. As shown in Fig. 3(b), the fiber spectrometer was able to resolve two lines separated by merely 1 pm. This spectral resolution is beyond the capabilities of even the largest bench-top grating spectrometers, which cannot realistically compete with the long pathlength achieved in an optical fiber.

Of course, a MMF with such high spectral resolution is also sensitive to environmental perturbations. In fact, MMFs have

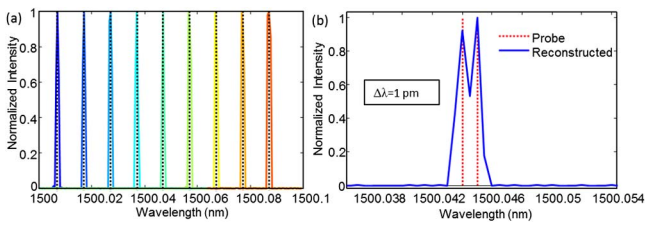

Fig. 3. (a) Reconstructed spectra for a series of narrow lines using the 100 m long MMF spectrometer. The probe frequencies are marked by vertical black dotted lines. (b) Reconstructed spectrum (blue line) of two narrow spectral lines separated by 1 pm. The red dotted lines mark the center wavelengths of the probe lines.

been used for a variety of environmental sensing applications, including temperature [12,13], pressure [14], and vibration sensing [15]. In these systems, a perturbation such as a change in the ambient temperature introduces a slight change in the refractive index of the glass fiber [13]. As a result, light travelling in the fiber experiences a slightly different propagation constant. In a sufficiently long fiber, this difference can add up to a significant change of the phase delay and alter the speckle pattern. Since our fiber spectrometer relies on a given wavelength consistently producing the same speckle pattern, changes in temperature would corrupt the reconstruction process.

In order to minimize mechanical perturbations, the fiber was secured to the spool using resin. We also spliced a SMF to the MMF to avoid any change in the input coupling condition [Fig. 1(b)]. However, changes in the ambient temperature in the lab still affected the fiber spectrometer. We estimated that a change of ~0.01°C was sufficient to produce an uncorrelated speckle pattern in a 100 m fiber [6]. In other words, the fiber environment should be held at a constant temperature, to within ~0.01°C. Although thermal stabilization at this level is possible, it would add complexity and cost to the fiber spectrometer. Next, we present a simple correction technique which can significantly improve the robustness of the fiber spectrometer to temperature fluctuations.

As the ambient temperature varies, the refractive index of the fiber glass changes due to the thermo-optic effect, $n(T + \delta T) = n(T)\ (1 + 7 \times 10^{-6}\delta T)$, and the length of the fiber changes due to thermal expansion, $L(T + \delta T) = L(T)\ (1 + 5 \times 10^{-7}\delta T)$ [13]. To understand the effect such changes have on the speckle pattern, we refer back to Eq. (1), which expresses the field at the output end of the fiber. The change in the refractive index affects the spatial profile $\boldsymbol{\psi}_{\mathbf{m}}$ of the modes and their amplitude A_m and initial phase ϕ_m, as well as the propagation constants β_m. The resulting change in the accumulated phase, $\beta_m(\lambda, T)L(T)$, is amplified by the length of the fiber. For long fibers and small changes in temperature, the effects of the changes to $\boldsymbol{\psi}_{\mathbf{m}}$, A_m, and ϕ_m on the speckle pattern are negligible compared with that to $\beta_m(\lambda, T)L$. Thus, we consider only the change in accumulated phase below.

If the temperature changes from T (the temperature during the calibration of the fiber spectrometer) to $T + \delta T$, the phase delay for the mth mode becomes $\beta_m(\lambda, T + \delta T)L(T + \delta T)$. It is equal to the phase delay at T for a slightly different wavelength $\lambda + \delta\lambda$, i.e., $\beta_m(\lambda + \delta\lambda, T)L(T) = \beta_m(\lambda, T + \delta T)\ L(T + \delta T)$. In principle, the wavelength change $\delta\lambda$ depends on the mode index m in the MMF. However, our numerical simulations reveal that for small temperature variations, the change in phase delay is approximately the same for all modes, and thus $\delta\lambda$ is nearly mode-independent. This means the speckle pattern generated by input light of wavelength λ at temperature $T + \delta T$ resembles the speckle pattern produced by the wavelength $\lambda + \delta\lambda$ at temperature T. Thus, the reconstruction algorithm would recover an input wavelength of $\lambda + \delta\lambda$ from the speckle pattern for λ at $T + \delta T$. This allows us to correct the temperature change δT by a wavelength shift $\delta\lambda$. Although the value of $\delta\lambda$ depends on λ, the operating bandwidth (0.1 nm) is much less than the wavelength

(1500 nm), and the thermo-optic coefficient and thermal expansion coefficient are almost constant across this bandwidth. Thus the variation of $\delta\lambda$ across the bandwidth is negligible, and we can adjust for a small change in the ambient temperature by applying a single $\delta\lambda$ correction factor. Usually the temperature change is slow, and therefore we propose to periodically interrogate the fiber spectrometer with a laser of a fixed wavelength to measure the $\delta\lambda$ that accounts for the current temperature, and then apply this simple correction to subsequent measurements.

To gauge the efficacy of this approach, we experimentally investigated the stability of the fiber spectrometer. Note that the measurements in Fig. 3 were performed within a few minutes after calibrating the MMF. The successful spectral reconstruction indicates that within this time, environmental conditions had not changed significantly. We then continued to record speckle patterns for ~10 h after calibration. Every ~1.5 min, we recorded speckle patterns at nine wavelengths across the spectrometer operating bandwidth. Figure 4(a) plots the reconstructed spectra from three sets of measurements. In the first set (bottom row), which was recorded ~1 min after calibration, each probe wavelength was accurately reconstructed. However, in the second and third set of measurements, recorded 10 and 20 min after calibration, the reconstructed lines are shifted relative to the probe lines due to changes in the ambient temperature. Nonetheless, the reconstruction algorithm still identified a narrow line for each measurement. This indicates that the speckle pattern produced by a wavelength λ at temperature $T + \delta T$ matched the speckle pattern produced by a nearby wavelength, $\lambda + \delta\lambda$, at the calibration temperature T. In addition, we note that for a given set of measurements recorded within a ~30 s time period [i.e., one row in Fig. 4(a)], each reconstructed line was shifted by the same amount. This confirmed our expectation that a single wavelength shift $\delta\lambda$ could be used to correct for the temperature-induced changes in all reconstructed spectra.

To correct for this wavelength shift, we assumed that the measurement at $\lambda = 1500.045$ nm was performed using a known reference laser. We then calculated the $\delta\lambda$ shift between 1500.045 nm and the peak wavelength of the reconstructed spectrum, and applied this same $\delta\lambda$ to the spectra reconstructed from other measurements. As shown in Fig. 4(b), each reconstructed line matched the probe line after this simple correction. To quantitatively assess the efficacy of this correction, we calculated the error between the reconstructed peak wavelength and the actual probe wavelength for all 4000 measurements recorded over the 10-h testing period. We then repeated the correction procedure by using the first probe line as a reference laser to estimate the current $\delta\lambda$. Figure 4(c) presents a histogram of the errors in the reconstructed wavelengths before and after this correction. Due to thermal fluctuations, the peak position of the reconstructed lines varied by as much as 15–20 pm from the actual wavelength before correction. However, after this simple correction, 95% of the measurements were accurate to within ±3 pm. In practice, a reference laser with a well-defined frequency may be used to repeatedly recalibrate the fiber spectrometer, significantly reducing the sensitivity to environmental perturbations. Note that this software correction was performed without any effort to stabilize the ambient temperature of the MMF. By combining the software correction with thermal and mechanical stabilization, we expect the MMF spectrometer with ultrahigh resolution could be made robust against environmental perturbations.

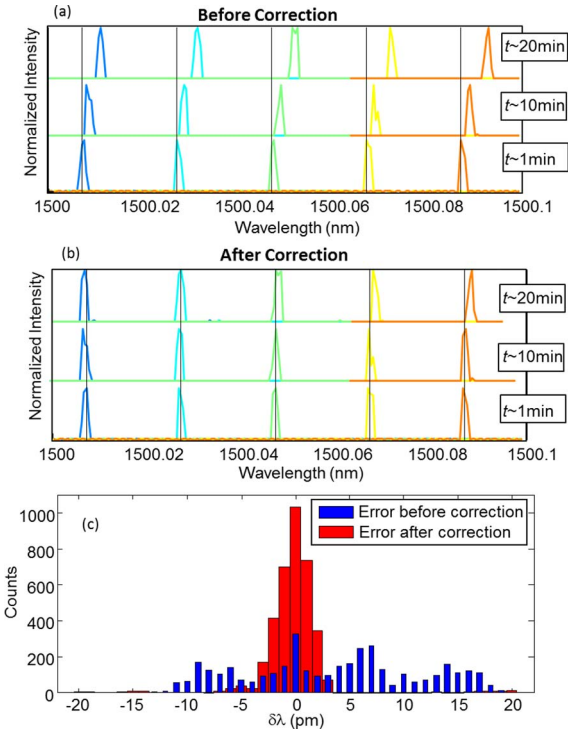

Fig. 4. (a) Each row shows five spectra reconstructed from the speckle patterns of five probe lines measured within ~30 s of each other at some time, t, after calibration (indicated next to the curves). Vertical black lines mark the spectral position of the probe lines. At $t \sim 1$ min (bottom row), the MMF spectrometer accurately recovers all five probe lines; but at $t \sim 10$ min (middle row) and 20 min (top row), the reconstructed lines shift from the actual wavelengths due to temperature fluctuations. Fortunately, all five lines in the same row (recorded within 30 s of each other) drift together, and thus a single wavelength shift $\delta\lambda$ can be used to correct for the drift. (b) Wavelength shift $\delta\lambda$ of the probe line at $\lambda = 1500.045$ nm was used to correct the drift of other lines in the same row. The corrected spectra match the probe lines well. (c) Histogram of the error between the input wavelength and reconstructed wavelength, $\delta\lambda$, for 4000 measurements recorded over 10 h. Before correction, the error ranges from −15 to +15 pm due to thermal fluctuations. After correction, 95% of the measurements fall within ±3 pm of the correct wavelength.

3. BROAD BANDWIDTH FIBER SPECTROMETER

In addition to ultrafine spectral resolution, MMF spectrometers can also operate with very broad bandwidth. In this section, we demonstrate broadband operation in the visible spectrum using a 4 cm long MMF (105 μm diameter core, NA = 0.22). In order to calibrate the wavelength-dependent speckle patterns in the visible spectrum, we used a broadband supercontinuum light source (Fianium WhiteLase SC400-4) in combination with a monochromator (Acton Research Corp. SpectraPro 500). The monochromator selected a narrow

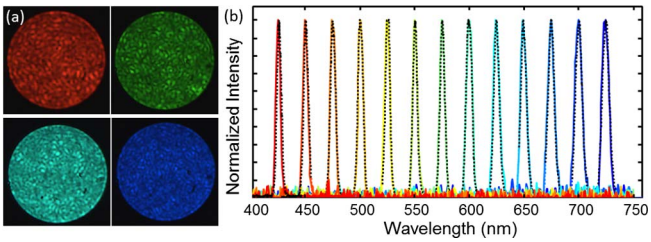

Fig. 5. (a) Speckle patterns recorded using a color CCD camera at the end of a 4 cm MMF. (b) Reconstructed spectra for a series of ~10 nm wide probes across the visible spectrum. Each solid colored line shows the reconstructed spectrum from a separate measurement and the black dotted lines show the corresponding spectra measured separately by a grating spectrometer.

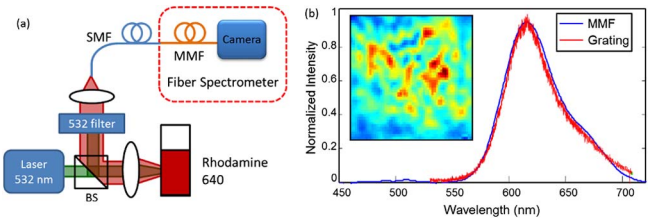

Fig. 6. (a) Schematic of the experimental setup for the photoluminescence measurement. The Rhodamine dye solution in the cuvette was pumped by a diode laser at $\lambda = 532$ nm, and the emission was collected by a SMF which was coupled to the MMF. (b) Photoluminescence spectrum of the Rhodamine dye measured by the fiber spectrometer and a grating spectrometer. The inset is a close-up of the speckle produced by the Rhodamine emission at the end of the 4 cm MMF.

(~0.2 nm full width at half maximum) band of the supercontinuum emission which was first coupled to a single-mode polarization-maintaining fiber and then to the MMF. The SMF ensured excitation of the same superposition of guided modes in the MMF and allowed us to test different light sources after calibration. To illustrate the speckle patterns formed by different colors, we used a color charge-coupled device (CCD) camera to record red, green, and blue speckles at the end of the MMF, as shown in Fig. 5(a). In the actual calibration and testing of the fiber spectrometer, we used a monochrome CCD camera (Allied Vision Manta). From the number of speckles, we estimated that ~700 spatial modes were excited in the MMF.

For the 4 cm fiber, the spectral correlation function of speckle has a HWHM of ~2 nm. We calibrated a transmission matrix consisting of 700 spectral channels from $\lambda = 400$ nm to $\lambda = 750$ nm in steps of 0.5 nm, and 4800 spatial channels. Not all the spatial channels are independent, although the shorter wavelengths provide more independent spatial channels than at $\lambda = 1500$ nm. We oversampled spatially in order to have a better reconstruction of broadband spectra [6]. After calibration, we switched to the lowest resolution grating (150 grooves/mm) in the monochromator and increased the exit slit width to obtain a tunable probe of ~10 nm bandwidth. We recorded a series of speckle patterns across the visible spectrum (400–750 nm), and separately measured the probe spectrum with a commercial grating spectrometer. The reconstructed spectra, shown in Fig. 5(b), match the spectra recorded by the grating spectrometer. We also tested the spectral resolution of the 4 cm fiber spectrometer, and found that it was able to resolve two narrow lines separated by 1 nm. Furthermore, unlike the 100 m fiber spectrometer, the short fiber spectrometer is relatively insensitive to environmental perturbations. For the same change in temperature, the change in accumulated phase delay is reduced by more than 3 orders of magnitude due to the difference in the fiber lengths. Consequently, the 4 cm fiber spectrometer is robust against temperature fluctuation within ~10°C [6].

After calibration, we used the 4 cm fiber spectrometer to measure the spectra of photoluminescence from Rhodamine 640 dye solution in a cuvette. Figure 6(a) is a schematic of the experimental setup. The output beam from a diode laser operating at $\lambda = 532$ nm was focused to the solution to excite the Rhodamine molecules. The emission was collected and focused to a SMF, which was coupled to the MMF. A long-pass filter was placed in front of the SMF to block the pump light. The inset of Fig. 6(b) is part of the speckle pattern produced by the photoluminescence at the end of the 4 cm MMF. Despite the broad bandwidth of the emission, speckle was still clearly visible, enabling the fiber spectrometer to reconstruct the spectrum. In Fig. 6(b), the photoluminescence spectrum measured by the fiber spectrometer coincides with the spectrum recorded separately by the grating spectrometer. The accurate measurement of the photoluminescence spectrum also confirmed that the SMF delivered the signal to the MMF in the same spatial mode used in the calibration.

4. DISCUSSION

In summary, a MMF spectrometer, consisting of a fiber and a camera, can provide high spectral resolution and large bandwidth while maintaining a small footprint. Using a 100 m long fiber coiled on a 3" spool, we were able to resolve two lines separated by 1 pm at $\lambda = 1500$ nm. A simple wavelength correction technique was developed to dramatically improve the stability of the ultrahigh-resolution fiber spectrometer against ambient temperature fluctuation. On the other extreme, a 4 cm long fiber can provide broadband operation, covering the visible spectrum (400–750 nm) with decent resolution (1 nm). It accurately captured the photoluminescence spectrum of Rhodamine dye.

MMF spectrometers offer clear advantages over traditional grating spectrometers. The most attractive feature is the ability to achieve high resolution with a compact size. This could enable portable miniature spectrometers with resolution currently only available in large bench-top systems. In addition, optical fiber is extremely low cost and lightweight, and has almost negligible loss over the lengths suitable for the spectrometer application. The reconstruction algorithm is fast and provides comparable accuracy to a grating spectrometer provided the probe signal is sufficient for an accurate measurement of the speckle pattern [16]. The input power dynamic range of the fiber spectrometer depends largely on the sensitivity and dynamic range of the camera used to record the speckle pattern and the coupling efficiency of the probe signal

into the MMF. Although high-resolution fiber spectrometers are sensitive to environmental perturbations, a combination of thermal and mechanical stabilization with software correction could enable robust performance.

The main limitation of the fiber spectrometer is that the probe signal must be confined to a fixed spatial mode and polarization state to ensure that a given wavelength always generates the same speckle pattern. In our implementation, this was done by first coupling the probe signal to a single-mode, polarization-maintaining fiber. This could limit the sensitivity of the fiber spectrometer to measure optical sources with low spatial coherence such as thermal sources, whose emission cannot be efficiently coupled to a SMF. Moreover, if a source (e.g., a multimode laser) contains multiple spectral lines, each having a distinct spatial pattern, they may couple to the SMF with different efficiencies. Although the wavelengths of all spectral lines can be measured accurately, their relative intensities may be distorted. Such a problem also exists for a grating spectrometer which collects light through a narrow slit, but the requirement for input to a fiber spectrometer is more restrictive. While the entrance slit in a grating spectrometer can be opened further to collect more light at the cost of lower resolution, exchanging the SMF for a few-mode fiber is more complicated. The input light must be spatially incoherent, namely, the light coupled to different spatial modes of the few-mode fiber must have an uncorrelated phase, so that the speckle patterns generated by each mode will add in intensity. The transmission matrix then needs to be recalibrated in order to include the speckle patterns not only from each spectral channel, but also from each spatial mode in the few-mode fiber. This would reduce the operation bandwidth, since the reconstruction algorithm has to find both the spatial profile and the spectral content of the input signal. We therefore expect the fiber spectrometer to be most useful in applications which already require light to be delivered by SMFs. Examples include optical wavemeters, spectral channel monitors used in telecommunications, or fiber-based sensors. In addition, spectroscopy techniques which utilize spatial confocality to probe small spatial volumes can use a SMF for signal collection, enabling integration with the fiber spectrometer. Examples include optical coherence tomography, microphotoluminescence spectroscopy, and micro-Raman spectroscopy. The operating wavelength, bandwidth, and spectral resolution of the fiber spectrometer can be easily tuned to match the needs of a given application.

FUNDING INFORMATION

National Science Foundation (NSF) (ECCS-1128542).

ACKNOWLEDGMENTS

We are grateful to Peter Rakich and Heedeuk Shin for aid in fiber splicing and providing access to their tunable laser. We also thank Kerry Vahala, Doug Stone, and Sebastien Popoff for useful discussions.

REFERENCES

1. Z. Xu, Z. Wang, M. Sullivan, D. Brady, S. Foulger, and A. Adibi, "Multimodal multiplex spectroscopy using photonic crystals," Opt. Express **11**, 2126–2133 (2003).
2. T. W. Kohlgraf-Owens and A. Dogariu, "Transmission matrices of random media: means for spectral polarimetric measurements," Opt. Lett. **35**, 2236–2238 (2010).
3. B. Redding, S. F. Liew, R. Sarma, and H. Cao, "Compact spectrometer based on a disordered photonic chip," Nat. Photonics **7**, 746–751 (2013).
4. Q. Hang, B. Ung, I. Syed, N. Guo, and M. Skorobogatiy, "Photonic bandgap fiber bundle spectrometer," Appl. Opt. **49**, 4791–4800 (2010).
5. B. Redding and H. Cao, "Using a multimode fiber as a high-resolution, low-loss spectrometer," Opt. Lett. **37**, 3384–3386 (2012).
6. B. Redding, S. M. Popoff, and H. Cao, "All-fiber spectrometer based on speckle pattern reconstruction," Opt. Express **21**, 6584–6600 (2013).
7. E. G. Rawson, J. W. Goodman, and R. E. Norton, "Frequency dependence of modal noise in multimode optical fibers," J. Opt. Soc. Am. **70**, 968–976 (1980).
8. P. Hlubina, "Spectral and dispersion analysis of laser sources and multimode fibres via the statistics of the intensity pattern," J. Mod. Opt. **41**, 1001–1014 (1994).
9. W. Freude, C. Fritzsche, G. Grau, and L. Shan-Da, "Speckle interferometry for spectral analysis of laser sources and multimode optical waveguides," J. Lightwave Technol. **4**, 64–72 (1986).
10. K.-P. Ho and J. M. Kahn, *Mode Coupling and its Impact on Spatially Multiplexed Systems*, Vol. **VIB** of Optical Fiber Telecommunications (Academic, 2013).
11. J. W. Goodman, *Speckle Phenomena in Optics* (Roberts & Company, 2007).
12. T. Okamoto and I. Yamaguchi, "Multimode fiber-optic Mach–Zehnder Interferometer and its use in temperature measurement," Appl. Opt. **27**, 3085–3087 (1988).
13. H. S. Choi, H. F. Taylor, and C. E. Lee, "High-performance fiber-optic temperature sensor using low-coherence interferometry," Opt. Lett. **22**, 1814–1816 (1997).
14. K. Pan, C. M. Uang, F. Cheng, and F. T. S. Yu, "Multimode fiber sensing by using mean-absolute speckle-intensity variation," Appl. Opt. **33**, 2095–2098 (1994).
15. O. A. Oraby, J. W. Spencer, and G. R. Jones, "Monitoring changes in the speckle field from an optical fibre exposed to low frequency acoustical vibrations," J. Mod. Opt. **56**, 55–66 (2009).
16. B. Redding, S. M. Popoff, Y. Bromberg, M. A. Choma, and H. Cao, "Noise analysis of spectrometers based on speckle pattern reconstruction," Appl. Opt. **53**, 410–417 (2014).

Research Article Vol. 1, No. 3 / September 2014 / Optica 181

Two-photon instant structured illumination microscopy improves the depth penetration of super-resolution imaging in thick scattering samples

PETER W. WINTER,[1,*] ANDREW G. YORK,[1] DAMIAN DALLE NOGARE,[2] MARIA INGARAMO,[3] RYAN CHRISTENSEN,[1] AJAY CHITNIS,[2] GEORGE H. PATTERSON,[3] AND HARI SHROFF[1]

[1]Section on High Resolution Optical Imaging, National Institute of Biomedical Imaging and Bioengineering, National Institutes of Health, Bethesda, Maryland 20892, USA

[2]Section on Neural Developmental Dynamics, Eunice Kennedy Shriver National Institute of Child Health and Human Development, National Institutes of Health, Bethesda, Maryland 20892, USA

[3]Section on Biophotonics, National Institute of Biomedical Imaging and Bioengineering, National Institutes of Health, Bethesda, Maryland 20892, USA

*Corresponding author: peter.winter@nih.gov

Received 8 May 2014; revised 31 July 2014; accepted 31 July 2014 (Doc. ID 211803); published 12 September 2014

Fluorescence imaging methods that achieve spatial resolution beyond the diffraction limit (super-resolution) are of great interest in biology. We describe a super-resolution method that combines two-photon excitation with structured illumination microscopy (SIM), enabling three-dimensional interrogation of live organisms with ~150 nm lateral and ~400 nm axial resolution, at frame rates of ~1 Hz. By performing optical rather than digital processing operations to improve resolution, our microscope permits super-resolution imaging with no additional cost in acquisition time or phototoxicity relative to the point-scanning two-photon microscope upon which it is based. Our method provides better depth penetration and inherent optical sectioning than all previously reported super-resolution SIM implementations, enabling super-resolution imaging at depths exceeding 100 μm from the coverslip surface. The capability of our system for interrogating thick live specimens at high resolution is demonstrated by imaging whole nematode embryos and larvae, and tissues and organs inside zebrafish embryos.

OCIS codes: (110.0180) Microscopy; (100.6640) Superresolution; (170.2520) Fluorescence microscopy; (180.0180) Microscopy.

http://dx.doi.org/10.1364/OPTICA.1.000181

1. INTRODUCTION

The speed, gentleness, molecular specificity, and contrast of fluorescence microscopy make it a powerful and versatile research tool, enabling diverse applications from cell biology to neuroscience. Although fluorescence imaging continues to improve [1,2], technical barriers still prevent these methods from reaching their full potential. Blurring introduced by diffraction limits the spatial resolution of widefield microscopy to ~250 nm laterally and ~500–750 nm axially, obscuring much detail at the subcellular scale. The effects of diffraction may be overcome with super-resolution techniques [3], but imaging three-dimensional (3D) samples presents additional challenges. At sufficient distances from the coverslip, the increasingly severe effects of optical aberrations [4] and scattering [5] degrade resolution and the signal-to-noise ratio (SNR) so that obtaining even diffraction-limited performance is difficult. Emerging techniques that provide super-resolution at depth and in 3D are thus of great practical interest in biology.

Stimulated emission depletion (STED) microscopy can provide sub-100-nm lateral resolution *in vivo* [6], but its

resolution is easily degraded by depth-dependent aberrations or scattering that distort the shape of excitation and depletion beams. Combining STED microscopy with adaptive optics can compensate for or reduce aberrations [7], and using two-photon (2P) excitation reduces scattering [8]; either approach improves STED microscopy at depth. Single-molecule imaging techniques enable sub-100-nm resolution in live cells [9], but out-of-focus background in 3D samples confounds the ability to localize individual molecules precisely (or at all), ultimately reducing imaging resolution and SNR. Using 2P [10] or selective plane [11] illumination can help to reduce background, thus extending the useful imaging range of these techniques. Despite these advances, neither STED nor single-molecule imaging has matured to the point that 3D acquisition in thick samples (i.e., imaging stacks >10 μm) is routine: the slow acquisition speed and high photobleaching/toxicity entailed by each of these super-resolution methods have limited the vast majority of live imaging applications to single imaging planes at or near the coverslip surface.

In contrast, linear structured illumination microscopy (SIM) offers a more modest ∼2× improvement in resolution beyond the diffraction limit than other super-resolution methods, but is far gentler and faster, thus facilitating the collection of tens to hundreds of live cellular volumes [12]. Linear SIM has historically been implemented by exciting the sample with a series of sinusoidal illumination patterns, imaging the fluorescence onto a multipixel detector, and computationally postprocessing and combining the resulting raw images to produce a super-resolution image. Sinusoidal illumination has the advantage of requiring relatively few illumination pattern positions, but suffers from an inability to physically reject out-of-focus light (i.e., optical sectioning is achieved entirely with computation). By using a single excitation focus in combination with a pinhole, as in image scanning microscopy (ISM) [13] (or multiple point-like excitation foci [14,15] in combination with pinholes) instead of sharp sinusoidal excitation patterns [16], out-of-focus background is inherently rejected by the microscope (i.e., without computation) [see Note S1 in Supplement 1], and depth penetration can be improved to enable 3D super-resolution imaging ∼50 μm from the coverslip surface [14]. Despite the apparent differences between sinusoidal SIM and point-based SIM implementations derived from ISM [13], the mechanism of resolution enhancement is the same [17] and, in fact, the same software can be used to process data generated by the two types of SIM [18]. Using multifocal 2P illumination has been shown to further improve SIM performance in thick samples, due to the inherently lower background afforded by 2P excitation [19]. Very recently, methods that perform the majority of postprocessing optically [20–22], instead of computationally, have been developed. The power of these methods is their speed: by eliminating the need for excess raw images, live, optically-sectioned super-resolution imaging at video rate or faster is possible (e.g., "instant SIM," ISIM [20]).

Here we present the first implementation of instant SIM that uses 2P excitation (2P ISIM), enabling imaging with ∼150 nm lateral and ∼400 nm axial resolution, at depths exceeding ∼100 μm. Relative to point-scanning 2P excitation microscopy (on which our microscope is based), our method offers improved resolution with no drawbacks in imaging speed or phototoxicity. Relative to all previous super-resolution SIM implementations, 2P ISIM offers better inherent optical sectioning, background rejection, and depth penetration, which we demonstrate on thick samples including bead phantoms, live nematode embryos and larvae, and zebrafish embryos.

2. RESULTS

Resolution enhancement in point-based SIM techniques can be understood first by considering resolution enhancement in a standard point-scanning confocal microscope. By closing the pinhole almost completely down in a confocal microscope, the point spread function (PSF) is reduced laterally by ∼1.4×, as the microscope's PSF becomes the product of approximately equal excitation and emission PSFs [22,23], and the frequency support of the microscope is doubled. However, this resolution is never achieved in practice in confocal microscopy as the almost-closed pinhole rejects far too much emission light, and any improvement in resolution is abrogated by the severely diminished SNR.

Point-based SIM [13–15,19–22] methods deliver ∼1.4× improvement in resolution over widefield microscopy without sacrificing signal by collecting emission with a multipixel detector, treating each pixel as a small pinhole, reassigning the light from each pixel onto a common origin, and summing the result. One method of reassignment is to shrink each emission focus locally before [20] or after [14,19] image acquisition, without changing the distance between foci. Alternatively, reassignment may be implemented by increasing the distance between adjacent emission foci while leaving their size unchanged (Fig. S1), which provides a convenient method for instant, point-based SIM, as has been demonstrated with single-photon (1P) excitation ("rescan microscopy" [21]). We implemented this same method of reassignment to enhance the resolution of 2P excitation microscopy, using an emission-side galvanometric mirror (galvo) to double the distance between adjacent scan points before image acquisition with a camera (Fig. 1 and Figs. S1 and S6 and Note S2 in Supplement 1, and the Methods section below. Use of the 2× expansion factor was determined empirically from measurements of the system excitation and emission PSFs, and from the performance of the system at various expansion factors (Note S2 in Supplement 1).

To study the resolution improvement enabled by 2P ISIM, we fixed U2OS human osteosarcoma cells and immunolabeled the microtubule cytoskeleton with Alexa Fluor 488 [Fig. 2(a)]. Compared to imaging in conventional, diffraction-limited 2P mode (i.e., scanning only the excitation-side galvo while holding the emission-side galvo fixed), the additional scanning introduced in 2P ISIM sharpened the image and resulted in microtubules with finer apparent width [Figs. 2(b) and 2(c)]. As in multifocal SIM [14,19] and ISIM [20], applying deconvolution further improved lateral resolution, resulting in microtubules with apparent width ∼160 nm and allowing us to resolve microtubules spaced by as little as 120 nm (Fig. S7 in

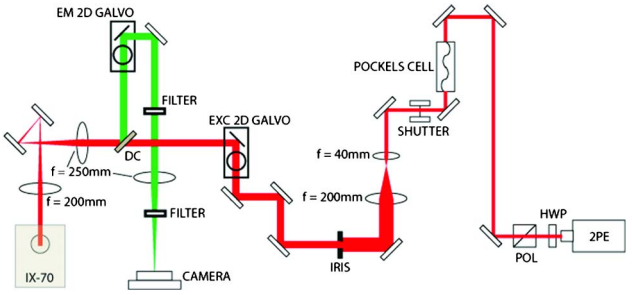

Fig. 1. Pulsed femtosecond laser (2PE) provides two-photon excitation to the sample (red), and fluorescence (green) is collected and imaged onto a camera. The remaining elements are used to shape, modulate, shutter, or scan the excitation, or scan and filter the emission (see text for more detail). Symbol key: HWP, half wave plate; POL, polarizer; EXC 2D GALVO, galvanometric mirror used to scan the excitation through the sample; DC, dichroic mirror; IX-70, microscope frame used to house the objective and sample (not shown); EM 2D GALVO, galvanometric mirror used to rescan the emission. Reflective mirrors are shown as rectangles, and other lenses referred to in the text are shown as ellipsoids with focal lengths as indicated. Note that the drawing is not to scale.

Supplement 1). We further quantified the resolution afforded by 2P ISIM by imaging 100-nm-diameter, yellow–green beads (Fig. S8 in Supplement 1), finding that 2P ISIM followed by deconvolution doubled the lateral resolution of the microscope when operated in diffraction-limited 2P excitation mode (from 311 ± 10 nm to 146 ± 5 nm, 30 beads). 2P ISIM did not improve the axial resolution of our system beyond the gains provided by deconvolution (predeconvolution, 668 ± 33 nm; postdeconvolution, 438 ± 22 nm, equivalent to the improvement obtained on images acquired in diffraction-limited 2P excitation mode). By "axial resolution," we mean the axial FWHM of a subdiffractive bead as opposed to "sectioning," which we define as the ability to distinguish two thin planes

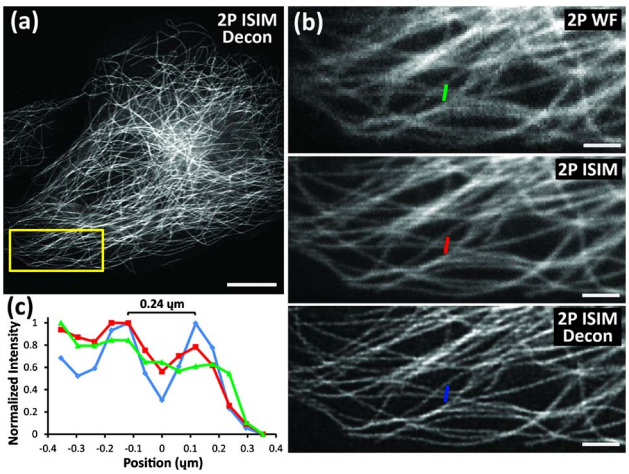

Fig. 2. Resolution enhancement in two-photon instant structured illumination microscopy (2P ISIM). (a) Immunolabeled microtubules in a fixed U2OS human osteosarcoma cell, as viewed in 2P ISIM, after deconvolution. (b) Higher-magnification view of the yellow rectangular region in (a), emphasizing resolution differences between images taken in 2P widefield (2P WF), 2P ISIM, and deconvolved 2P ISIM modes. (c) Line-outs of microtubules marked in green, red, and blue in (b). Scale bar: 10 μm in (a) and 3 μm in (b). See also Fig. S7 in Supplement 1.

in z. We suspect the lack of improvement in z is due to aberrations in our 1P emission PSF that enlarge its axial extent compared to the diffraction-limited result predicted by theory. In this case, the recorded image is dominated by the axial extent of the 2P excitation PSF and the photon reassignment process does not result in any improvement in axial resolution.

Having verified that 2P ISIM doubled the lateral resolution of the 2P microscope, we next characterized its performance at depths further from the coverslip in phantom samples consisting of subdiffractive fluorescent beads embedded in a scattering matrix [5.0% agarose gel containing 2.5%, 62 nm diameter nonfluorescent polystyrene beads (Fig. 3)]. Compared to previous forms of multifocal structured illumination microscopy, 2P ISIM provided better imaging depth in scattering samples: we observed recognizable images of individual beads at depths up to ~125 μm [Fig. 3(a)], even though the images at depth deteriorated relative to those collected at the coverslip surface. In contrast, we were unable to observe recognizable beads at depths >50 μm from the coverslip surface when using 1P excitation (1P ISIM [18]). When setting the illumination conditions for similar SNR at the coverslip, both SNR and the signal-to-background ratio (SBR) degraded much faster with depth when using 1P rather than 2P illumination [Fig. 3(b)]. We also compared 2P ISIM to 2P multifocal SIM (2P MSIM [19]), and found similar, albeit less dramatic, improvements in SBR and SNR when using 2P ISIM [Fig. 3(b)]. Next, we examined signal degradation and background levels independently (Fig. S9 in Supplement 1). In all three methods, signal deteriorated significantly as a

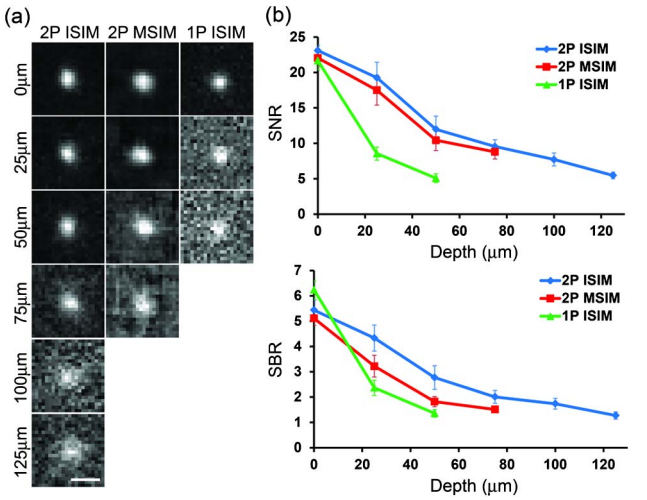

Fig. 3. Two-photon ISIM improves SNR and SBR relative to single-photon implementations. (a) Representative images of subdiffractive fluorescent beads in a scattering matrix, as observed in 2P ISIM, 2P MSIM, and 1P ISIM systems. All images are autoscaled independently, and "0 μm" corresponds to the coverslip surface. Scale bar: 500 nm. The limited range of the 2P MSIM piezo stage prevented us from comparing 2P ISIM and 2P MSIM at depths greater than 75 μm from the coverslip, and data are not shown for depths further than 50 μm from the coverslip for the 1P ISIM system due to low SBR. (b) Graphs indicating falloff in SNR and SBR as a function of depth from the coverslip surface. Means and standard deviations are indicated from measurements taken on 6 beads at each depth (see also Fig. S9 in Supplement 1). Note that these images were not deconvolved.

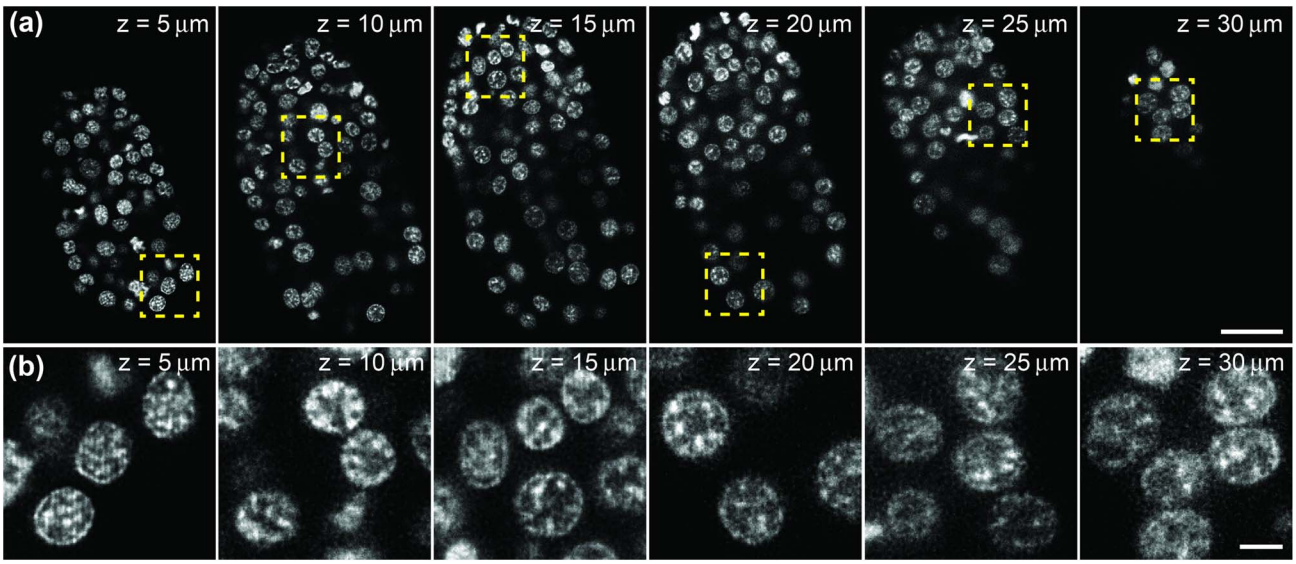

Fig. 4. Two-photon ISIM enables visualization of subnuclear chromatin structure throughout nematode embryos. (a) Selected slices at indicated axial distance from the coverslip, through a live nematode embryo (bean stage). Scale bar: 10 μm. (b) Higher magnification views of yellow rectangular regions in (a), emphasizing subnuclear chromatin structure throughout the imaging volume. Scale bar: 2 μm. All images have been deconvolved. See also Media 1.

function of depth, with 1P ISIM signal diminishing the fastest. Background remained essentially constant for 2P ISIM but increased significantly with 1P ISIM, and to a lesser extent with 2P MSIM. Consistent with these observations, when comparing the background rejection ability of all three techniques in a thick fluorescent lake (Fig. S10 in Supplement 1), 2P ISIM offered the best sectioning performance. We conclude that the superior performance of 2P ISIM at depth relative to other forms of point-based structured illumination microscopy results from (i) the use of 2P illumination (less scattering of excitation, and thus higher signal generation in thick samples) and (ii) the lack of excitation and emission crosstalk inherent to parallelized methods such as 1P ISIM and 2P MSIM (leading to lower levels of background in thick samples) [24].

To demonstrate that the benefits of 2P ISIM also apply in thick, live samples, we imaged transgenic *Caenorhabditis elegans* embryos expressing GFP–H2B [Fig. 4(a), Media 1]. In these samples, scattering prevents super-resolution imaging at depths more than ~15 μm from the coverslip when using 1P illumination [14] (Fig. S11 and Media 2 in Supplement 1): subnuclear chromatin structure is evident close to the coverslip surface, but image quality rapidly worsens at depth so that nuclei eventually resemble featureless blobs. The loss in image resolution and contrast at depth that result from using 1P illumination cannot be compensated for simply by increasing the exposure time, which serves mainly to increase the background (Fig. S12 in Supplement 1). When using 2P ISIM, we observed only a slight degradation in signal at increasing depth, which was easily compensated for by applying a modest ramp in input intensity during volumetric acquisition (Methods). Unlike 1P ISIM, we were easily able to observe subnuclear chromatin structure throughout all planes of the imaging stack [Fig. 4(b)].

We then used 2P ISIM to image the nervous system in whole, live, anesthetized *C. elegans* larvae (Fig. 5) with the transcriptional reporter *psax-3::GFP*. SAX-3 is the *C. elegans* ROBO receptor homolog and is widely expressed throughout the nervous system [25]. By stitching together 10 fields of view, we reassembled an entire L2 stage larva, visualizing neurons and neurites throughout its ~350 μm length [Fig. 5(a), Media 3]. In addition to the GFP signal that highlighted these neuritis and cell bodies, we visualized autofluorescence in the 425–475 nm range from the larval body and gut structures (pseudo-red color, Fig. 5). This second color proved useful in defining the extent of the worm body, as well as internal regions such as the isthmus, terminal bulb of the pharynx, intestine, and intestinal lumen. Higher-magnification views within this dataset highlight the dorsal and ventral nerve cords [Fig. 5(b)], and resolved these processes [to an apparent width <200 nm, Fig. 5(c)], as well as the cell bodies and neurites of nerve ring neurons [Fig. 5(d)]. Our resolution and SNR were sufficiently high to distinguish closely spaced neuronal structures in both lateral [Fig. 5(d)] and axial [Figs. 5(e) and 5(f)] views of the nerve ring, and to capture transverse neurites that spanned the head of the larva [Fig. 5(e), in Media 3].

We also investigated the performance of 2P ISIM in thicker live samples. Our technique allowed us to visualize the microtubule network in a 38–40 h zebrafish eye in transgenic zebrafish engineered to have GFP-tagged microtubules, enabling inspection of the cytoskeleton of the developing lens beneath both the corneal and lens epithelial layers, at depths greater than 100 μm from the coverslip surface [Fig. 6(a), Media 4]. Upon close inspection of individual XY slices [Figs. 6(b)–6(f)] and a medial XZ slice [Fig. 6(g)], the rudimentary organization of the lens can be clearly observed, with multiple layers of microtubule networks forming clear, concentric spherical shells surrounding a central core. Although eventually the secondary lens fibers are elongated and well organized into symmetric layers [26], at this stage, microtubules in the lens are more disordered and 3D reconstruction revealed a surprisingly

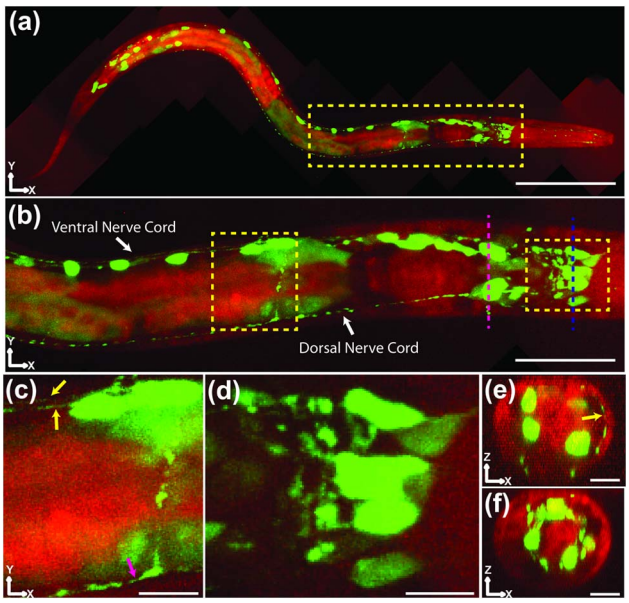

Fig. 5. Two-color, 2P ISIM imaging in a live, anesthetized nematode larva. (a) Ten 2P ISIM volumes were acquired and stitched together to generate a two-color (green, GFP; red, blue-shifted autofluorescence) XY maximum intensity projection of an L2 nematode larva expressing transcriptional reporter *psax-3*::*GFP*, which is widely expressed throughout the nervous system. The head of the animal lies to the right, while the tail is located to the left. The yellow rectangle denotes the nerve ring and anterior portion of the nematode gut. Scale bar: 60 μm. (b) Higher-magnification view of the yellow rectangular region in (a), emphasizing nerve cords and nerve ring. Numerous head neurons and ventral cord motor neurons are visible in this view, as well as autofluorescent structures like the terminal bulb of the pharynx and the intestine. Scale bar: 20 μm. (c), (d) Higher-magnification views of yellow rectangular regions in (b). The yellow arrows show both the left and right fascicles of the ventral nerve cord, while the magenta arrow denotes the dorsal nerve cord. A neuronal process connecting the dorsal and ventral nerve cords is visible just anterior to the magenta arrow. In (d), neurons and neuronal processes in the nematode head can be resolved. Scale bar: 4 μm in (c), (d). The green colormap has been saturated in order to highlight dim neurites and subneuronal structures. (e), (f) Axial cuts through the imaging volume, corresponding to magenta and blue dashed lines in (b). Head neurons are visible in both views, while a neurite crossing the dorsal region of the head is denoted by a yellow arrow in (e). Scale bar: 5 μm. Neurites and fasciculating neurites denoted by yellow arrows in (c) and (e) have apparent lateral width <200 nm. All images were deconvolved. See also Media 3.

dense network of cytoskeletal fibers that appeared to curve tortuously throughout the volume of the lens [Figs. 6(a), 6(b), and 6(d); Media 5]. Despite our modest imaging rate of 1.67 frames per second (0.33 frames per second after 5× frame averaging), we were able to capture dividing cells in the lateral proliferative zone without significant motion blur [Fig. 6(a)]. Furthermore, although scattering degraded image quality farther into the sample, affecting both lateral and (to a greater extent) axial resolution [Fig. S13 in Supplement 1], we were still able to resolve thin microtubule bundles of apparent lateral width <200 nm throughout our 110 μm imaging volume [Figs. 6(b)–6(e)].

The zebrafish samples also facilitated a comparison between 2P ISIM and conventional, point-scanning 2P imaging on a Leica SP5 microscope (an example of a modern, commercial 2P system used by biologists). We compared a lateral view of the midbrain–hindbrain boundary in a 36 h old zebrafish embryo on both systems [Fig. 7]. Although a rigorous comparison between the two systems is difficult due to differences in objectives, excitation power, and detection efficiency, at similar NA and acquisition speed, 2P ISIM delivered images with higher resolution and better SNR. For example, both microscopes revealed that microtubule filaments appeared to assemble into polygonal shapes throughout the volume [an example in Fig. 7(a) is shown ~20 μm from the coverslip]. While these structures appeared mostly continuous in the conventional 2P system, 2P ISIM clearly revealed the punctate nature of the individual bundles that made up the polygons [Fig. 7(b), Media 6]. The superior resolution of 2P ISIM also resolved fine filament bundles in axial views of the sample along the long axes of cells [Figs. 7(c) and 7(d), Media 7], which were otherwise obscured in the conventional 2P microscope.

3. DISCUSSION

Our technique improves the spatial resolution of point-scanning 2P microscopy (2PM), requiring only simple modifications to the emission-side optical train of this workhorse system. Relative to the recent rescanning microscopy technique [21] (where a detection pinhole is needed to prevent out-of-focus emission from landing on the camera), 2P excitation eliminates the need for a detection pinhole in the emission path because out-of-focus emission does not occur (i.e., optical sectioning is inherent in the excitation process) [Note S1, 27]. This allows direct expansion of the illumination pattern without the need to first descan, thereby simplifying instrument design and alignment. Relative to our previous instant SIM implementation, 2P ISIM utilizes a single excitation focus instead of an array of foci, which also simplifies instrument design by eliminating the need for microlens arrays. 2P ISIM capability can thus be straightforwardly added to many existing 2P systems. Similar to our previous ISIM implementation [20], 2P ISIM approximately doubled the lateral spatial resolution of the conventional microscope that we modified, without any tradeoff in data acquisition speed or phototoxicity. Moreover, the longer wavelengths, 2P effect, and focused illumination employed offer better resolution, depth penetration, and inherent optical sectioning capability in thick fluorescent specimens relative to all previous SIM implementations. Since our technique requires an areal detector (camera) instead of a point detector (photomultiplier tube), it is more susceptible to scattering of emission than conventional 2PM. Nevertheless, combining 2P ISIM with chemical clearing methods [28,29] mitigates this issue and may prove immediately fruitful, likely enabling super-resolution imaging at unprecedented depth.

Many improvements to conventional 2PM would also benefit 2P ISIM, as the latter technology is based on the former. For example, excitation efficiency might be improved with dispersion compensation, which we did not incorporate here.

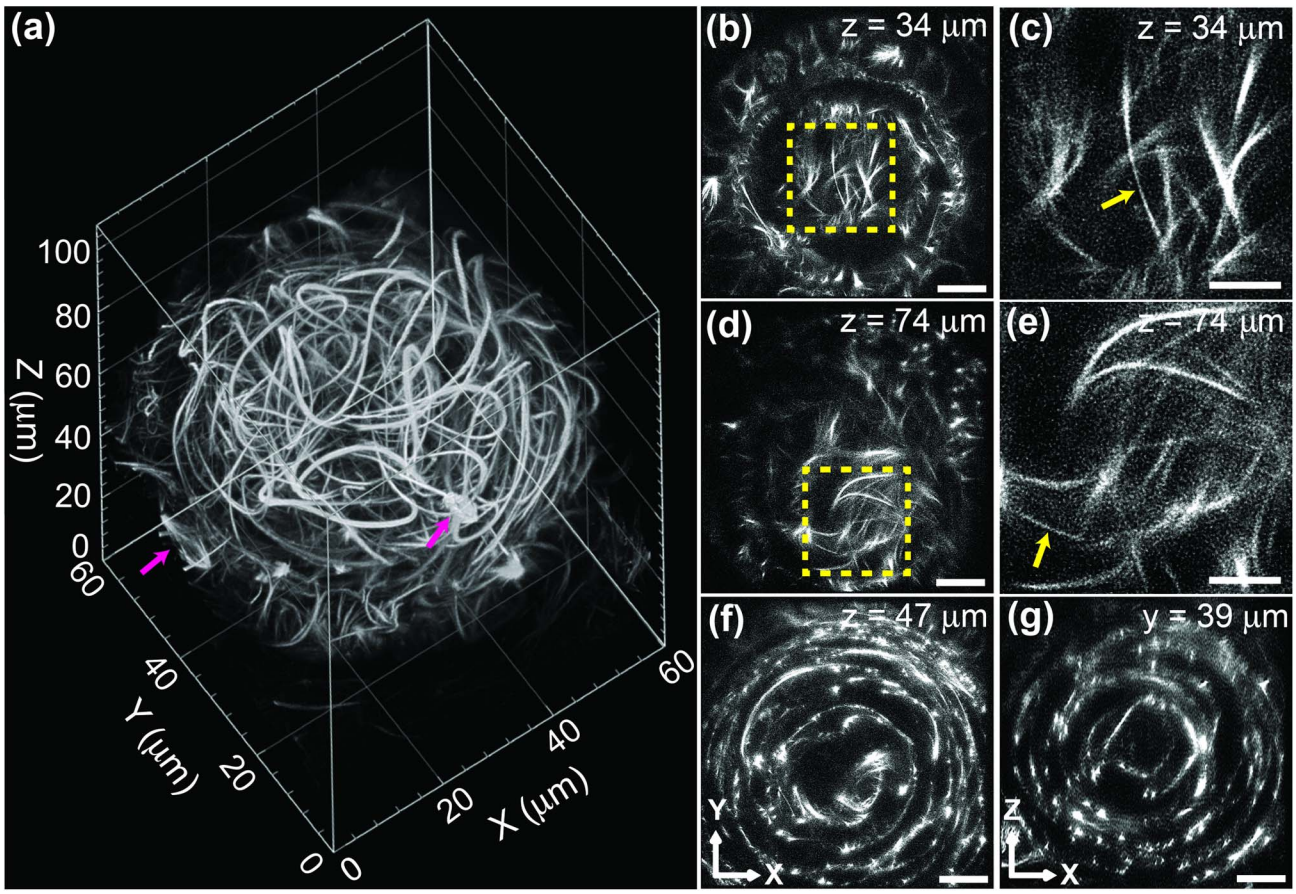

Fig. 6. 2P ISIM enables super-resolution imaging in volumes of ~100 μm thickness. (a) Rendering of ~60 × 60 × 110 μm volume (eye of 38–40 h old, live zebrafish embryo) captured with 2P ISIM. Single microtubules, bundles of microtubules, and dividing cells (magenta arrows) are visible in the volume. See also Media 4. (b), (d), (f) XY slices at indicated axial (Z) distance from the base of the stack. See also Media 5. Scale bar: 10 μm. (c), (e) Higher-magnification views of the yellow regions in (b), (d), emphasizing thin filaments (yellow arrows) with apparent width <200 nm. Scale bar: 5 μm. (g) XZ slice at indicated lateral (Y) distance from the origin of the stack, emphasizing concentric, circular cytoskeletal organization within the eye. Scale bar: 10 μm. All data presented in this figure were deconvolved.

Using adaptive optics on both the excitation [30] and emission side [31] would likely improve the SNR and resolution, especially axially and at increasing depths from the coverslip. Finally, the speed of the galvanometric mirrors limits our current full field of view (FOV) frame rate to 1.67 Hz (and typically less than 0.5 Hz, as we frame-averaged all datasets). Increasing the frame rate can be easily achieved by reducing the FOV along the slow galvo axis (e.g., by reducing our FOV to ~60 μm × 15 μm from ~60 μm × 60 μm, a frame rate of ~7 frames per second may be achieved). This flexibility contrasts with 2P MSIM [19], where the current scan pattern requires that 340 individual frames be collected to produce a single super-resolved image with a ~33 μm × 33 μm FOV, thereby preventing frame rates greater than ~0.3 Hz. Implementing resonant scanners would also improve our hardware speed, although in live biological samples we often found our frame rate more limited by signal than hardware, and synchronization of scanners may prove difficult. Finally, an alternative route to high-speed operation may be to parallelize the excitation. In this case, care must be taken when choosing the number and spacing of additional excitation foci to balance increases in speed against degradation in sectioning and to make best use of the available laser power.

4. METHODS

A. Optical System

The output from an 80 MHz Ti:sapphire oscillator capable of producing pulses of 140 fs duration (Coherent, Chameleon Ultra II) was used as the 2P excitation source. The laser beam was passed through a Glan-Laser calcite polarizer (Newport, 10GL08AR.16) and a half-wave plate (HWP, Newport, 10RP52-2), and the HWP was placed in a motorized rotation mount (Thorlabs, PRM1Z8E) for automated power control. After passing through the polarization optics, the beam was passed through a Pockels cell (Conoptics, 350-80-LA-02 KD*P Series E-O modulator and Driver 302M) and mechanical shutter (Thorlabs, SH05) for further intensity control. The Pockels cell provided rapid (on the μs scale) intensity modulation with incomplete extinction, whereas the mechanical shutter operated more slowly (on the ms scale), but provided complete extinction. Next, the beam was expanded 5× with

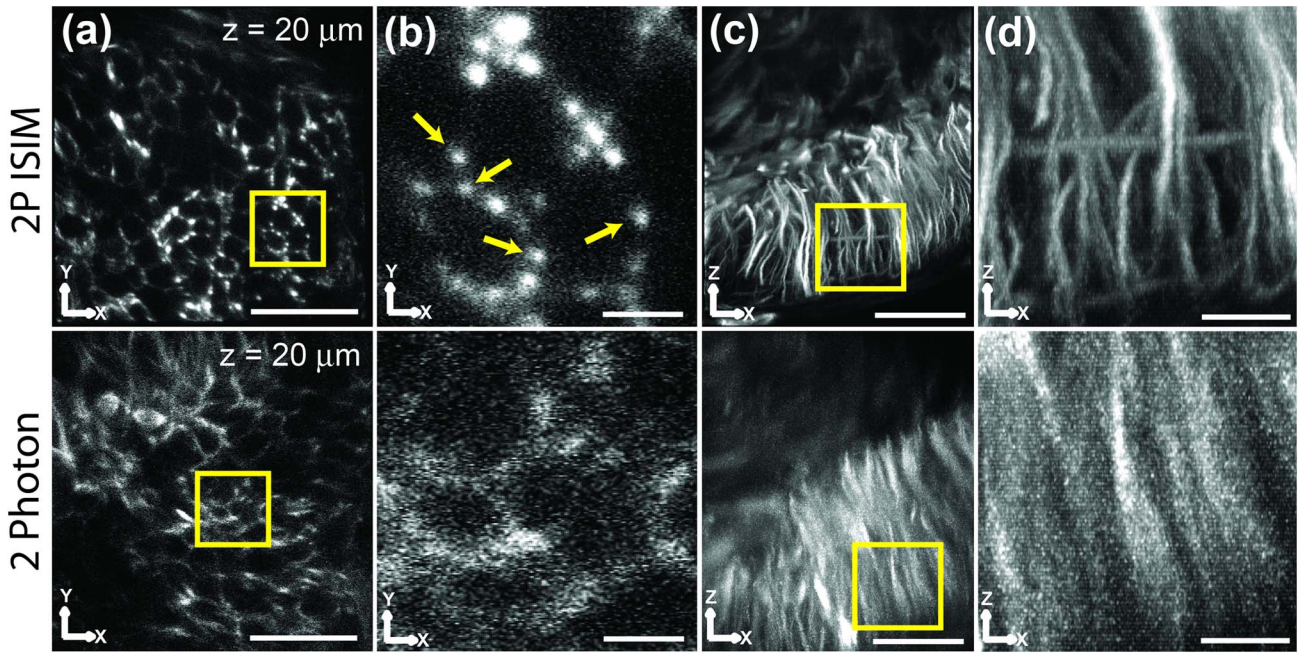

Fig. 7. 2P ISIM provides better resolution and SNR than conventional 2P microscopy. The same brain region in a zebrafish embryo was imaged in 2P ISIM (top row) and on a conventional, point-scanning 2P system (the Leica SP5, bottom row). (a) XY slices ~20 μm from the coverslip. Scale bar: 20 μm. (b) Higher-magnification views of region marked by the yellow square in (a). Scale bar: 3 μm. Yellow arrows indicate individual microtubule bundles. (c) XZ maximum intensity projections of the volumes. Scale bar: 20 μm. (d) Higher-magnification views of the region marked by the yellow square in (c). Scale bar: 5 μm. Images are raw, i.e., they have not been deconvolved. See also Media 6 and Media 7.

two achromatic lenses (Thorlabs, $f = 40$ mm and $f = 200$ mm, AC254-040-B-ML, AC254-200-B-ML), passed through an iris (which served to reduce the beam diameter during alignment), and directed onto a two-dimensional galvanometric mirror assembly (Thorlabs, GVS012). The point midway between each mirror in the galvo assembly was imaged onto the back focal plane of a 60×, 1.2 NA objective (Olympus, UPLSAPO60XWPSF) using two achromatic lenses (Thorlabs, $f = 250$ mm and $f = 200$ mm, AC508-250-A-ML, AC254-200-A-ML) placed in a $4f$ telescope configuration between objective back focal plane and galvo assembly. Rotations of the galvanometric mirror assembly thus translated the excitation at the sample plane. The objective was housed in a microscope frame (Olympus, IX-70), and a reflective mirror (Chroma, 21010) was placed inside the filter turret in order to direct the beam into the objective. Samples were housed on an automated XY stage (ASI, S3192100FT) equipped with a 300 μm z axis piezo top plate (ASI, PZ-2300).

Fluorescence was collected through the same 60× objective lens, and passed through the same 200 mm/250 mm achromatic telescope mentioned above. A dichroic mirror (DC, Iridian, 6 mm thick and transmits 488 nm, 561 nm, 700–1100 nm, BJR000005) separated fluorescence from excitation, and was placed between the 250 mm achromat and a second, two-dimensional galvanometric mirror (Thorlabs, GVS012) assembly. The second galvo system was placed one focal length away from the 250 mm achromat, imaging the back focal plane of the objective lens onto the midpoint between galvo mirrors. Rotations of the galvo thus served to rescan fluorescence originating from the sample plane. A final achromatic lens (Thorlabs, $f = 250$ mm, AC508-250-A-ML) was placed one focal length after the galvo assembly, and served to focus the fluorescence image onto an electron-multiplying CCD (CAMERA, Andor, DU-885K-CS0-#VP, back-thinned with 1004 × 1002, 8 μm × 8 μm pixels and a CCI-23 control card). Two 680 nm short pass filters (Semrock, FF01-680/SP-25) were also included in the emission path to eliminate 2P illumination light reflected by the dichroic. These optics are shown in schematic form in (Fig. 1).

The optical magnification between sample and camera was $(200/3 * 250/250) = 67\times$, resulting in a pixel size of 119.5 nm, which was confirmed using transmitted light images of a reticle. However, in SIM mode, the 2× expansion factor produced when the emission-side 2D galvo is scanned reduces the pixel size to 60 nm, which we confirmed by translating a sample of fluorescent beads a known distance with our automated stage.

B. Data Acquisition and Imaging Parameters

1. 2P ISIM

All 2P ISIM data were collected on a PC running 32 bit Windows XP SP3, with an Intel Xeon X3450 4 Core CPU, 2.67 GHz/core, and 3 GB RAM. Hardware components were controlled using custom control software written in LabVIEW (National Instruments, Version: 2012 SP1), and image acquisition was accomplished using manufacturer's software (Andor, Solis Version: 4.12.30003.0) via external trigger mode. Acquisition of 3D data required integrated control of the mechanical shutter, Pockels cell, 2D galvos, camera, and piezo stage. All devices were controlled by external voltage

using digital and analog outputs from a multichannel DAQ device (National Instruments, PCI-6733) and BNC connector block (National Instruments, BNC-2110). The mechanical shutter and camera were triggered via digital outputs, and the Pockels cell, 2D galvos, and piezo z stage were controlled by analog output. Due to its low impedance, we built a buffer amplifier to provide additional current to optimally drive the Pockels cell.

Rastering the illumination spot across the sample was accomplished by scanning one mirror from each 2D galvo assembly at 2 Hz and the other at 900 Hz. Note that in order to double the distance between adjacent emission foci before imaging, the amplitude and frequency of the waveforms delivered to excitation- and emission-side galvo assemblies was identical (this choice is justified in Note S2 in). Given the amplitude of our scan pattern, 900 Hz was the fastest scan speed at which we could maintain synchronization between the excitation- and emission-side galvos. During imaging, scanning of the galvos was initiated via the fire out signal from the camera. Figure S2 in Supplement 1 shows examples of the triangular and sinusoidal waveforms used to control the 2D galvo assemblies. Figure S3 in Supplement 1 shows examples of the control waveforms for the mechanical shutter, camera, and piezo stage for a 3D stack consisting of 4 image planes separated by 1 μm, with 2 frames acquired per plane.

As the fast-axis excitation galvo changes direction at the end of each sinusoidal line scan, it slows down, resulting in a significant increase in the total 2P illumination dose delivered to the sample near the edges of the FOV. The fluorescence signal rate F is proportional to I^2t, where I is the instantaneous illumination intensity and t the dwell time of the excitation. A sinusoidal galvo scan implies that the dwell time of the galvo can be described by a secant waveform. We therefore fed the Pockels cell a $\sqrt{\text{cosine}}$ waveform, which improved image uniformity (Figs. S3 and S4 in Supplement 1).

Andor Solis settings for all images were identical: the camera was cooled to −65°C, the exposure time was set to 500 ms, electron multiplication gain set to 300, the preamplifier gain to 3.8×, vertical pixel shift speed set to 3.72715 μs, and the horizontal pixel shift readout rate set to 35 MHz at 14 bits. Triggering was set to kinetic acquisition mode via external trigger, and data spooled to the hard disk as. tiffs.

Images for all figures were collected at 1.0–1.5 mW average power, as measured at the sample. All images were collected using 900 nm wavelength illumination except for Fig. 5, where GFP was excited at 950 nm and autofluorescence excited at 750 nm. For the images in Fig. 5, an additional 525 nm bandpass filter (Semrock, FF01-525/50-25) was included during GFP imaging, and a 442 nm bandpass filter (Semrock, FF01-442/46-25) was included during autofluorescence imaging. Details on frame averaging, total frame time, z step size, and total number of z slices for all 2P ISIM images can be found in Table S1 in Supplement 1. The average illumination intensity was held constant during acquisition of all 3D data sets except for the *C. elegans* embryo shown in Fig. 4, where the average illumination intensity per 2D slice was linearly ramped from 100% to 125% of its initial value during the 3D acquisition.

2. 2P MSIM

We used a previously described 2P MSIM system to acquire images [19], employing the same 1.2 NA objective used for 2P ISIM experiments. For images of fluorescent beads, the exposure time was set to 30 ms per image, and the z step size set to 200 nm. For each 2D slice, 340 images were acquired, resulting in an effective imaging rate of ∼0.1 Hz. For images of the thick fluorescent lake, the exposure time was also 30 ms per image and the z step size set to 100 nm.

3. 1P ISIM

We used a previously described 1P ISIM system to acquire images [20], employing the same 1.2 NA objective used for 2P ISIM experiments. For all data presented here, the laser was set to maximum power. For the images of fluorescent beads in 3D gels, the exposure time was 80 ms per image, and the z step between images was 200 nm. For images of the thick fluorescent lake, the exposure time was 40 ms per image, and the z step was 100 nm. For images of *C. elegans* embryos in Fig. S11 in Supplement 1, the exposure time was 80 ms per image and the z step was 250 nm. For the *C. elegans* images presented in Fig. S12 in Supplement 1, the low-exposure images were taken at 80 ms exposure and the high-exposure images taken at 800 ms exposure. For both of these datasets, the z step size was 250 nm.

C. System Alignment

Alignment of most of the optics in our 2P ISIM is straightforward. Particular care was taken when aligning the relative scan patterns of the excitation- and emission-side 2D galvos. Figure S5 in Supplement 1 shows the effects of an initial rotary offset between the images produced by these two galvo assemblies. We corrected this offset by rotating the scan pattern of one of the galvo assemblies relative to the other assembly using the LabVIEW Cartesian Coordinate Rotation VI. In principle, the scan pattern of either galvo can be modified. We chose to modify the scan pattern of the excitation-side galvo assembly to match the emission-side galvo assembly. The optimal scan pattern correction was determined empirically by scanning identical regions in a thick fluorescent slide (Chroma, 92001) with either the excitation-side or emission-side galvos alone, and then examining the images as pseudo-colored overlays in Image J (NIH, version: 1.48c). By applying a rotation angle of 2.81°, we were able to minimize the offset until it was no longer discernible. We then oriented the camera to match the scan pattern of the emission-side 2D galvo assembly.

In addition to alignment of the galvo scan patterns, correct setting of the phase offset between the excitation- and emission-side fast galvos was critically important for optimal performance. Figure S6 in Supplement 1 shows the effects of small mismatches in the phase alignment of the two fast galvos. Mismatches of even 1° result in a distinctive doubling artifact. Mismatches of less than 1°, while not producing a perceptible doubling, greatly reduce the lateral resolution of the system along the fast galvo scan axis by smearing intensity across the camera. We found the best way to align the relative phases of the fast-scanning galvos was to image 100 nm, yellow–green

fluorescent beads (Invitrogen, F8803) at different phase offsets and analyze their FWHM.

D. Conventional 2P Microscopy

A Leica SP5 inverted confocal microscope equipped with an ultrafast pulsed laser (SpectraPhysics, Mai Tai DeepSee) tuned to 900 nm at 2.18 W was used for conventional 2P experiments (Fig. 7). A bidirectional resonance scanner operating at 8000 Hz with 32 lines of scan averaging was used for image acquisition, resulting in a 2D acquisition time of ~4 s. Stacks were acquired using a 20× NA 1.0 objective lens (Leica, HCX APO 20X) at 11.6× zoom, with 0.25 μm steps between slices. Single slices measured 1024 × 1024 pixels for a field of 63.53 μm^2 (62 nm pixel size).

E. Bead Samples

We prepared two kinds of bead samples in this manuscript: fluorescent bead layers for measuring PSFs at the coverslip surface and fluorescent beads embedded in 3D scattering gels for measuring PSF degradation at depth. Fluorescent bead layers were prepared by coating 24 × 50 mm #1.5 coverslips (VWR, 48393241) with 100 mg/ml poly-L lysine (Sigma, P8920), depositing 20–40 μL of 100 nm diameter yellow–green fluorescent beads (Invitrogen, F8803, 1:1000 dilution in water) on the coverslips, waiting for 10 min, and gently washing the coverslips in water to remove excess beads from the coverslip. Samples were then immersed in water for imaging. Fluorescent beads in 3D scattering gel samples were prepared by suspending 100 nm diameter yellow–green fluorescent beads at 1:250 dilution into a solution containing 5% agarose (Sigma, A9539) and 2.5% nonfluorescent 0.062 μm scattering polystyrene beads (Bangs Laboratories, PS02N). This mixture was vortexed vigorously and sonicated for 2 min before heating. After heating, the gelled mixture was deposited on a #1.5 coverglass bottomed dish (Matek, P35G-1.5-14-C), allowed to cool, and then immersed in water for imaging.

F. Quantification of SNR and SBR

Signal (for Figs. 3 and Fig. S9 in Supplement 1) was estimated by computing the average intensity of an 8 × 8 pixel box centered over the bead of interest. Background was estimated by computing the average intensity from an equally sized area containing no visible beads at the same depth. SNR was calculated as the ratio of the average signal from a bead over the standard deviation of the background region. SBR was calculated as the ratio of the average signal from a bead over the average background intensity. For all bead measurements, an averaged "dark current" (camera shutter open, no excitation light) image was subtracted from the bead image stack prior to analysis.

G. Quantification of Bead Size/Apparent Resolution

All measurements of bead FWHM, except the measurement of the 2P excitation PSF, were calculated using the ImageJ plugin "Plot FWHM" that fits a Gaussian function to vertical and horizontal cuts centered on the brightest point in the image (http://www.umanitoba.ca/faculties/science/astronomy/jwest/plugins.html courtesy of Jennifer West, University of Manitoba). The emission PSF was measured by exciting the bead sample with filtered light (Semrock, FF02-482/18-25) from a halogen lamp (i.e., using the transillumination pillar of our microscope to provide wide-field illumination), and collecting emission through a 525 bandpass (Semrock, FF01-525/50-25) filter. The 2P excitation PSF lateral FWHM was manually estimated from a plot of the average intensity of a 6 × 6 pixel region centered on a bead, as the excitation light was sequentially stepped across the field of view (note that the emission galvo was held stationary for this measurement; only the excitation galvos were scanned). Images were cropped prior to analysis.

H. Immunolabeled Cells

Microtubules in cultured U2OS human osteosarcoma cells (ATCC,HTB-96) were immunolabeled as follows: Cells were washed 3× with cytoskeletal buffer (CB) (10 mM PIPES, 138 mM KCl, 3 mM $MgCl_2$, 2 mM EGTA, 0.01% NaN_3, 160 mM sucrose, pH 6.8), fixed and permeabilized for 30 min at 37°C in a mixture of 0.5% glutaraldehyde, 3.7% formaldehyde, and 0.3% Triton X-100 (vol/vol) in CB, washed 5× with CB, and quenched 3× in ice-cold CB containing 100 mM Glycine. Cells were washed 1× with CB between each round of quenching. After quenching, cells were washed 3× with CB and blocked in antibody dilution buffer (Abdil, 150 mM NaCl, 20 mM Tris, 0.1% Triton X-100 (vol/vol), 0.1% NaN_3, 4% BSA, pH 7.4) for 1 h, rocking them gently on an agitator (Lab Quake). After blocking, Abdil was aspirated and cells were incubated with 4 μg/mL monoclonal mouse anti-α-tubulin primary antibody (Sigma, T6199) in Abdil for 2 h at room temperature with rocking, washed 5× in Abdil, incubated in a 1:200 dilution of Alexa fluor 488 goat antimouse secondary antibody (Molecular probes, A11001) in Abdil for 3 h at room temp with rocking, washed 4× with Abdil, washed 4× in deionized water, and imaged.

I. Nematode Samples

Worm strains were raised at 20°C on NGM plates seeded with OP50 *E. coli*. Strain BV24 (*[ltIs44 [pie-1p-mCherry::PH(PLC1delta1) + unc-119(+)]; zuIs178 [(his-72p::HIS-72::GFP); unc-119(+)]V]*) was used to image nuclei, and strain IC692 (*quEx 162 sax-3p::GFP + pRF4 rol-6*) was used to image neuronal cell bodies and neurites. BV24 embryos were obtained by cutting adult hermaphrodites in half with a razor blade, then transferring embryos to a well chamber coated with Poly-L-lysine for imaging via mouth pipette (Sigma-Aldrich, A5177). L2 stage worms of strain IC692 were immobilized with 50 mM levamisole and imaged on an agarose pad sandwiched between two #1.5 coverslips. Strain IC692 was obtained from the Caenorhabditis Genetics Center, and strain BV24 was kindly supplied by Dr. Zhirong Bao.

J. Zebrafish Samples

$Tg(XlEef1a1:dclk2-GFP)^{io008}$ zebrafish embryos [14] were collected by natural spawning and maintained at 28°C. Embryos were anesthetized in Tricaine (Sigma, E10521) at a

concentration of 600 μM in embryo medium [60 mg RedSea Coral Pro Salt (Drs. Foster and Smith Pet Supplies) per liter ddH_2O]. Anesthetized embryos were mounted in 1% low-melt agarose (Cambrex, 50080) in Lab-Tek II chamber slides (Nunc, 155379), covered with embryo medium, and imaged at room temperature.

FUNDING INFORMATION

National Institute of Biomedical Imaging and Bioengineering (NIBIB) (EB000074); National Institute of Child Health and Human Development (NICHD).

ACKNOWLEDGMENTS

This work was supported by the Intramural Rsearch Programs of the U.S. NIBIB (to P.W.W., A.G.Y, M.I., R.C., G.H.P., and H.S.), and the Eunice Kennedy Shriver NICHD (to D.D.N. and A.C.). We thank Yicong Wu for help with LabVIEW programming and Christian Combs for help in rendering 3D datasets. We thank Victor Wang for help with stitching the 3D datasets. We thank students in the Marine Biology Laboratory Physiology course, especially Greg Alushin, Daria Bonazzi, and Alexis Lomakin, for help with construction of an early prototype of this device. We also thank Henry Eden for critical feedback on the manuscript. The NIH does not endorse or recommend any commercial products, processes, or services. The views and opinions of authors expressed here do not necessarily state or reflect those of the U.S. Government and they may not be used for advertising or product endorsement purposes. A. G. Y., G. H. P., and H. S. conceived the idea. P. W. W., A. G. Y., and H. S. designed the optical system. P. W. W. built the optical system and implemented data acquisition software with guidance from A. G. Y. and P. W. W., D. D. N., and M. I. acquired data. R. C., D. D. N., and A. C. provided guidance on biological experiments. P. W. W., R. C., and D. D. N. prepared the samples. D. D. N., M. I., G. H. P., and A. C. provided biological reagents or equipment. P. W. W., D. D. N., R. C., and H. S. analyzed the data. P. W. W. and H. S. wrote the paper with input from all authors. H. S. supervised the Research.

See Supplement 1 for supporting content.

REFERENCES

1. R. S. Fischer, Y. Wu, P. Kanchanawong, H. Shroff, and C. M. Waterman, "Microscopy in 3D: a biologist's toolbox," Trends Cell Biol. **21**, 682–691 (2011).
2. Y. Wu, R. Christensen, D. Colon-Ramos, and H. Shroff, "Advanced optical imaging techniques for neurodevelopment," Curr. Opin. Neurobiol. **23**, 1090–1097 (2013).
3. S. Cox and G. E. Jones, "Imaging cells at the nanoscale," Int. J. Biochem. Cell Biol. **45**, 1669–1678 (2013).
4. S. W. Hell, G. Reiner, C. Cremer, and E. H. K. Stelzer, "Aberrations in confocal fluorescence microscopy induced by mismatches in refractive index," J. Microsc. **169**, 391–405 (1993).
5. B. C. Wilson and S. L. Jacques, "Optical reflectance and transmittance of tissues: principles and applications," IEEE J. Quantum Electron. **26**, 2186–2199 (1990).
6. S. Berning, K. I. Willig, H. Steffens, P. Dibaj, and S. W. Hell, "Nanoscopy in a living mouse brain," Science **335**, 551 (2012).
7. T. J. Gould, D. Burke, J. Bewersdorf, and M. J. Booth, "Adaptive optics enables 3D STED microscopy in aberrating specimens," Opt. Express **20**, 20998–21009 (2012).
8. K. T. Takasaki, J. B. Ding, and B. L. Sabatini, "Live-cell superresolution imaging by pulsed STED two-photon excitation microscopy," Biophys. J. **104**, 770–777 (2013).
9. H. Shroff, C. G. Galbraith, J. A. Galbraith, and E. Betzig, "Live-cell photoactivated localization microscopy of nanoscale adhesion dynamics," Nat. Methods **5**, 417–423 (2008).
10. A. G. York, A. Ghitani, A. Vaziri, M. W. Davidson, and H. Shroff, "Confined activation and subdiffractive localization enables whole-cell PALM with genetically expressed probes," Nat. Methods **8**, 327–333 (2011).
11. F. C. Zanacchi, Z. Lavagnino, M. P. Donnorso, A. Del Bue, L. Furia, M. Faretta, and A. Diaspro, "Live-cell 3D super-resolution imaging in thick biological samples," Nat. Methods **8**, 1047–1049 (2011).
12. L. Shao, P. Kner, E. H. Rego, and M. G. L. Gustafsson, "Super-resolution 3D microscopy of live whole cells using structured illumination," Nat. Methods **8**, 1044–1046 (2011).
13. C. B. Muller and J. Enderlein, "Image scanning microscopy," Phys. Rev. Lett. **104**, 198101 (2010).
14. A. G. York, S. H. Parekh, D. D. Nogare, R. S. Fischer, K. Temprine, M. Mione, A. B. Chitnis, C. A. Combs, and H. Shroff, "Resolution doubling in live, multicellular organisms via multifocal structured illumination microscopy," Nat. Methods **9**, 749–754 (2012).
15. O. Schulz, C. Pieper, M. Clever, J. Pfaff, A. Ruhlandt, R. H. Kehlenbach, F. S. Wouters, J. Großhans, G. Bunt, and J. Enderlein, "Resolution doubling in fluorescence microscopy with confocal spinning-disk image scanning microscopy," Proc. Natl. Acad. Sci. USA **110**, 21000–21005 (2013).
16. M. G. L. Gustafsson, "Surpassing the lateral resolution limit by a factor of two using structured illumination microscopy," J. Microsc. **198**, 82–87 (2000).
17. R. Heintzmann and M. G. L. Gustafsson, "Subdiffraction resolution in continuous samples," Nat. Photonics **3**, 362–364 (2009).
18. M. Ingaramo, A. G. York, E. Hoogendoorn, M. Postma, H. Shroff, and G. H. Patterson, "Richardson–Lucy deconvolution as a general tool for combining images with complementary strengths," Chem. Phys. Chem. **15**, 794–800 (2014).
19. M. Ingaramo, A. G. York, P. Wawrzusin, O. Milberg, A. Hong, R. Weigert, H. Shroff, and G. H. Patterson, "Two-photon excitation improves multifocal structured illumination microscopy in thick scattering tissue," Proc. Natl. Acad. Sci. USA **111**, 5254–5259 (2014).
20. A. G. York, P. Chandris, D. Dalle Nogare, J. Head, P. Wawrzusin, R. S. Fischer, A. Chitnis, and H. Shroff, "Instant super-resolution imaging in live cells and embryos via analog image processing," Nat. Methods **10**, 1122–1126 (2013).
21. G. M. R. De Luca, R. M. P. Breedijk, R. A. J. Brandt, C. H. C. Zeelenberg, E. de Jong Babette, W. Timmermans, L. Nahidi Azir, R. A. Hoebe, S. Stallinga, and E. M. M. Manders, "Re-scan confocal microscopy: scanning twice for better resolution," Biomed. Opt. Express **4**, 2644–2656 (2013).
22. S. Roth, C. J. R. Sheppard, K. Wicker, and R. Heintzmann, "Optical photon reassigment microscopy (OPRA)," Opt. Nanosc. **2**, 1–6 (2013).
23. C. J. R. Sheppard, "Super-resolution in confocal Imaging," Optik **80**, 53–54 (1988).
24. P. W. Winter and H. Shroff, "Faster fluorescence microscopy: advances in high speed biological imaging," Curr. Opin. Chem. Biol. **20**, 46–53 (2014).
25. J. A. Zallen, B. A. Yi, and C. I. Bargmann, "The conserved immunoglobulin superfamily member SAX-3/Robo directs multiple aspects of axon guidance in C. elegans," Cell **92**, 217–227 (1998).
26. T. M. Greiling and J. I. Clark, "Early lens development in the zebrafish: a three-dimensional time-lapse analysis," Dev. Dyn. **238**, 2254–2265 (2009).
27. M. G. L. Gustafsson, L. Shao, P. M. Carlton, C. J. R. Wang, I. N. Golubovskaya, W. Z. Cande, D. A. Agard, and J. W. Sedat, "Three-

dimensional resolution doubling in wide-field fluorescence microscopy by structured illumination," Biophys. J. **94**, 4957–4970 (2008).
28. H. Hama, H. Kurokawa, H. Kawano, R. Ando, T. Shimogori, H. Noda, K. Fukami, A. Sakaue-Sawano, and A. Miyawaki, "Scale: a chemical approach for fluorescence imaging and reconstruction of transparent mouse brain," Nat. Neurosci. **14**, 1481–1488 (2011).
29. K. Chung, J. Wallace, S. Y. Kim, S. Kalyanasundaram, A. S. Andalman, T. J. Davidson, J. J. Mirzabekov, K. A. Zalocusky, J. Mattis, A. K. Denisin, S. Pak, H. Bernstein, C. Ramakrishnan, L. Grosenick, V. Gradinaru, and K. Deisseroth, "Structural and molecular interrogation of intact biological systems," Nature **497**, 332–337 (2013).
30. D. Debarre, E. J. Botcherby, T. Watanabe, S. Srinivas, M. J. Booth, and T. Wilson, "Image-based adaptive optics for two-photon microscopy," Opt. Lett. **34**, 2495–2497 (2009).
31. P. Kner, J. W. Sedat, D. A. Agard, and Z. Kam, "High-resolution wide-field microscopy with adaptive optics for spherical aberration correction and motionless focusing," J. Microsc. **237**, 136–147 (2010).